Measurement of the Double Differential Dijet Rate in Deep Inelastic Scattering at HERA and Comparison to NLO QCD Calculations

Vom Fachbereich Physik
der Universität Dortmund
zur Erlangung des akademischen Grades eines
Doktors der Naturwissenschaften
genehmigte

Dissertation

von
Diplom-Physiker Roman Pöschl
aus
Hagen

Dortmund
Oktober 2000

Contents

Preface

The understanding of the structure of matter is the subject of the research in the field of elementary particle physics. Scattering experiments play a dominant role in the quest for fundamental particles and forces. Presumably the most famous scattering experiment was performed by Ernest Rutherford and his collaborators in the year 1911 [RUT11]. They shot α particles on a gold foil and observed that some of these particles were deflected by an unexpected large angle from the initial direction of flight. Rutherford drew the conclusion that the atoms, up to that time regarded as fundamental particles, have a substructure consisting of an atomic shell and a nucleus.

In the following decades the picture about the structure of matter has been improved by a large variety of experimental and theoretical efforts.

The year 1992 marks the advent of the HERA accelerator at DESY (Deutsches Elektronen Synchrotron) in Hamburg. With this machine, high energy collisions between electrons and one constituent of the nucleus, the proton, are performed. With high resolution power the structure of the proton itself and the interactions between its constituents, the quarks, are studied. Some aspects of the strong force responsible for these interactions are investigated in this thesis. The effects of this strong force manifest themselves in collimated bundles of particles called jets. The analysis presented in this thesis is concentrated on a class of events in which jets are identified in the H1 detector.

This thesis is organized as follows. The first chapter will give an introduction to the basic theory of deep inelastic scattering and the special features of jet events. In the second chapter the experimental apparatus used for the measurement is described. In the third chapter the selection criteria of the events analyzed in this thesis are described. The quality of the selected data is discussed in the fourth chapter by means of numerous control distributions which are the basis of the correction of the measured data for comparison to theoretical predictions. The comparison of the data to these predictions will be performed in the fifth chapter.

Chapter 1

Theoretical Background

1.1 Introduction to Deep-Inelastic Scattering

Do the hadrons have a structure and, if yes, how does this structure look in detail ? Experiments where a highly energetic lepton is scattered off a proton target are an appropriate tool to answer these questions, because the exchanged boson has a virtuality which allows the structure of the proton, to be resolved. In deep inelastic scattering (DIS) the virtuality Q^2 of the exchanged boson is much larger than the mass of the proton. Figure 1.1 sketches the interaction between an incoming positron on a proton via the exchange of a photon with virtuality Q^2. In addition ep

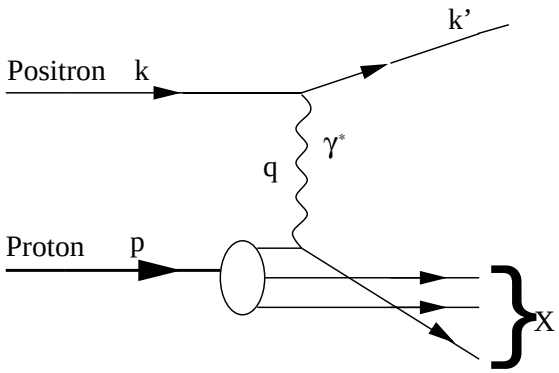

Figure 1.1: Schematic representation of deep inelastic electron proton scattering

interactions may also take place by the exchange of Z^0 or $W^{\pm}$ bosons. However, in the framework of this analysis these processes can be neglected since they are suppressed in the kinematic region studied and will not be considered further. In the case of neutral boson exchange the products of the process shown in Figure 1.1 are the scattered positron and a hadronic final state X. The kinematic quantities describing this process can be determined in terms of the four momenta of the incident and scattered lepton, $k, k^{'}$, and the momentum p of the incident proton:

- The square of the lepton-proton center-of-mass energy is given by:[1]

$$s = (k+p)^2 \approx 2kp. \tag{1.1}$$

- The virtuality of the exchanged boson is given by:

$$Q^2 = -q^2 = -(k-k^{'})^2 \ . \tag{1.2}$$

- The Bjorken scaling variable is given by

$$x_B = \frac{Q^2}{2pq}; (0 < x_B < 1), \tag{1.3}$$

[1] Throughout this thesis the rest masses of the particles are neglected.

and can be interpreted, in the naive parton model [BJO69], as the momentum fraction carried by the struck parton with respect to the total momentum of the incoming proton

- The inelasticity variable
$$y = \frac{pq}{pk}; (0 < y < 1) \tag{1.4}$$
defines the energy transfer from the lepton to the proton in the rest frame of the proton and is related to the earlier defined variables Q^2 and x_B via $y = \frac{Q^2}{s x_B}$.

- The square of the invariant mass of the hadronic final state X is given by:
$$W^2 = (p+q)^2 = \frac{1-x_B}{x_B} Q^2. \tag{1.5}$$

Only three of the four variables are independent from each other. Usually s, x_B and Q^2 are chosen. Since s is fixed by the energies of the incoming particles, two independent variables remain to fully describe the kinematics of inclusive deep inelastic scattering.

The cross section of the $ep \to eX$ process can be expressed as

$$\sigma \propto L_{\mu\nu} W^{\mu\nu}. \tag{1.6}$$

Here $L_{\mu\nu}$ denotes the leptonic tensor describing the interaction between the lepton and the exchanged virtual boson. The hadronic tensor $W^{\mu\nu}$ corresponds to the boson-proton vertex. In Quantum Electro Dynamics (QED) the lepton-photon vertex is well defined and therefore $L_{\mu\nu}$ is completely calculable. Using Lorentz invariance, current conservation and assuming parity conservation, the hadronic tensor can be reduced to only two functions which parameterize the structure of the proton. The DIS cross section has the well known form

$$\frac{d^2\sigma}{dx_B dQ^2} = \frac{4\pi\alpha^2}{x_B Q^4} (x_B y^2 F_1(x_B, Q^2) + (1-y) F_2(x_B, Q^2)). \tag{1.7}$$

Here α denotes the fine structure constant. The functions F_1 and F_2 parameterize the inner structure of the proton. Its determination is one of the main goals of the HERA experiments.

For the analysis of the hadronic final state X, it is useful to define another set of variables which have special properties under Lorentz boosts along the z-axis where the z-axis is defined by the incoming proton direction. The pseudo-rapidity

$$\eta = -\ln\left(\tan\left(\frac{\theta}{2}\right)\right) \tag{1.8}$$

defined via the polar angle θ changes its magnitude only by an additive constant under Lorentz boosts along the z axis. Thus differences in the pseudo-rapidity are invariant under Lorentz boosts along the z-axis. Further variables are the azimuthal angle ϕ and the transverse energy $E_t = E\sin\theta$ where E and θ are the energy and polar angle of either a single object of the hadronic final state or of well defined combinations of hadronic final state objects, see e.g. Section 1.1.1 or 1.6.

1.1.1 Reconstruction of Kinematic Variables

A precise reconstruction of the kinematic variables x_B,y, Q^2 is crucial for the analysis of deep inelastic scattering events.

Due to the redundancy of the H1 detector, see Chapter 2, a precise determination can be done either from the kinematics of the scattered electron alone, from hadronic final state or using information from both, e.g. the angle of scattered positron and the angle of the hadronic final state. Three different methods have been used in this analysis; the hadron method, the electron method and the double angle method. They are described in detail in [BAS95].

With the electron method the kinematics of the scattering process are fully determined by the energy, $E_e^{'}$, and the polar angle, θ_e, of the scattered positron:

$$Q^2 = 4E_e E_e^{'} cos^2 \frac{\theta_e}{2} \tag{1.9}$$

$$y_e = 1 - \frac{E_e^{'}}{E_e} sin^2 \frac{\theta_e}{2} \tag{1.10}$$

$$x_B = \frac{Q^2}{y_e s}. \tag{1.11}$$

The hadron or Jaquet-Blondel method uses only hadron variables and the kinematical variables of interest can be determined by summing over the energies (E_i), transverse ($p_{x,i}, p_{y,i}$) and longitudinal momenta ($p_{z,i}$) of the hadronic final state particles. The kinematics are thus given by the following expressions:

$$y_h = \frac{\sum_i (E_i - p_{z,i})}{2E_e} \tag{1.12}$$

$$Q_h^2 = \frac{(\sum p_{x,i})^2 + (\sum p_{y,i})^2}{1 - y_h} = \frac{E_{t,h}}{1 - y_h} \tag{1.13}$$

$$x_{Bh} = \frac{Q_h^2}{y_h}. \tag{1.14}$$

Finally, the kinematic variables can be reconstructed from the angle θ_e of the scattered positron and the angle γ_h of the hadronic final state using the double angle method. Here, the angle γ_h represents, in the naive quark parton model, the direction of the struck quark and is obtained from the hadronic flow measurement according to

$$\tan\frac{\gamma_h}{2} = \frac{\sum (E_i - p_{z,i})}{E_{t,h}}. \tag{1.15}$$

Using 1.15 and the scattering angle θ_e of the scattered positron one gets

$$y_{DA} = \frac{\tan\frac{\gamma_h}{2}}{\tan\frac{\theta_e}{2} + \tan\frac{\gamma_h}{2}} \tag{1.16}$$

$$\mathrm{Q}_{DA}^2 = 4E_e^2 \frac{\sin\gamma_h (1 + \cos\theta_e)}{\sin\gamma_h + \sin\theta_e - \sin(\theta_e + \gamma_h)} \tag{1.17}$$

$$x_{DA} = \frac{Q_{DA}^2}{y_{DA} s}. \tag{1.18}$$

The energy of the scattered positron can be expressed in terms y_{DA} and θ_e as follows:

$$E_{DA} = \frac{E_e (1 - y_{DA})}{\sin^2 \frac{\theta_e}{2}}. \tag{1.19}$$

The advantage of the double angle method is its independence (to first order) of the energy scale since the angular information the method is based upon is derived from ratios of energies leading to a partial cancellation of energy scale uncertainties. This feature is used in Sections 4.4 and 4.6 to estimate part of the systematic error of the results which will be obtained in this thesis.

The electron method will be used exclusively in this thesis for the final result. This method has been proven to provide good resolution in the kinematic region $y > 0.1$ [GLA98], where its resolution increases from 20% in the region $0.1 < y < 0.2$ to 4% at $y \approx 0.7$. Especially towards large y it is superior to the other methods [GLA98]. However, the redundancy offered by the other methods will be exploited to check the energy scale of the detectors used in the analysis, see Section 4.4.

1.2 The Naive Quark-Parton Model

The idea that the proton is built up by constituents was formulated by Gell-Mann [GEL64] as a result of the observation to account for the rich variety of different hadrons observed in high-energy-collision experiments. The introduction of proton constituents called quarks established an inner symmetry into the observed particle spectrum and allowed the explanation of the electric charge and the spin of the hadrons.

In the late 60's and early 70's it was confirmed in deep inelastic scattering experiments that the proton is made out of constituents which correspond to the postulated quarks [FRI91]. This led to the formulation of the so called (naive) quark-parton model [BJO69, FEY69] which is based on the following assumptions:

- The proton is made out of point-like constituents called quarks which share the total momentum of the proton.
- The quarks are moving free parallel to the proton.
- The quarks have a spin of 1/2.
- The quarks have a multiple of $\pm 1/3$ the elementary electric charge e. For example, the proton is built of two quarks with charge $+2/3e$ and one quark with charge -1/3e.
- Deep inelastic electron proton scattering can be regarded as elastic scattering of the electron off of a free quark of the proton. In this sense the term $\frac{4\pi\alpha^2}{x_B Q^4}$ on the right hand side of Equation 1.7 is equivalent to the well-known Rutherford scattering formula and describes the elastic scattering of two point-like electric charges.

Following these assumptions, the structure functions included in Equation 1.7 are only dependent on x_B and given by

$$F_1(x_B) = \frac{1}{2x_B} \sum e_i^2 x_B f_i(x_B) \tag{1.20}$$

$$F_2(x_B) = \sum e_i^2 x_B f_i(x_B) \tag{1.21}$$

where the parton density functions f_i are interpreted as the probability to find a quark with momentum fraction x_B inside the proton. The sum runs over all different quark flavors. The postulation that the structure functions depend only on the fractional proton momentum is called scaling and was established in deep inelastic scattering experiments at SLAC for values

of $x_B \approx 0.25$ [BLO69]. The scaling behavior implies that the two structure functions F_1 and F_2 are related by the Callan-Gross relation [CAL69]

$$F_2(x_B) = 2x_B F_1(x_B). \tag{1.22}$$

The Equation 1.22 only holds, if the quarks have spin 1/2 which was experimentally verified in 1969 [ALB69].

However, experiments in the early 70's showed a deviation from the scaling behavior predicted by the naive quark-parton model. The measured structure functions showed a logarithmically dependence on the four momentum transfer Q^2 [FOX74, AND77, DRE83]. Moreover, it was observed that the quarks carry only 50% of the total momentum of the proton. These two contradictions to the assumptions of the naive quark-parton model can be explained in the framework of Quantum-Chromodynamics (QCD), a field theory of strong interactions which describes the interactions between quarks as mediated by gluons. Gluons do not couple to the photon and carry the missing momentum of the proton [GRO79].

1.3 Basics of QCD

In the framework of QCD, the interaction between the quarks are driven by an additional degree of freedom called color. Quarks may appear in three different color states usually labeled 'red', 'green' and 'blue'. The strong or color force is mediated via electrically neutral spin 1 particles called gluons. To a certain extend, these gluons are similar to the carriers of the electromagnetic force, the photons. However, there is one striking difference. In contrast to the photons, which do not carry an electromagnetic charge, the gluons carry color charge which leads to strong interactions between gluons.

Analogous to QED, QCD driven amplitudes can be expanded in a perturbation series of a coupling constant, denoted α_s, which quantifies the strength of the strong force. To calculate cross sections in QCD, contributions from real and virtual quarks and gluons have to be considered in the perturbation series. Virtual contributions are, for example, the loop diagrams shown in Figure 1.2. The Feynman rules demand the integration of each loop over the inner

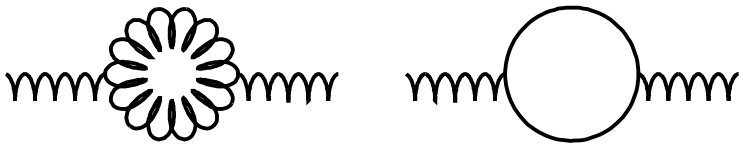

Figure 1.2: One loop diagrams which lead to the running of the coupling constant α_s.

four momentum k, which is not fixed by energy momentum conservation. These integrals are logarithmically divergent for $|k| \to \infty$. To account for this, the ultraviolet divergences are renormalized and absorbed into the coupling constant α_s. The renormalization procedure introduces an artificial mass parameter μ_r^2 on which the coupling constant depends. Any physical quantity R must not depend on this artificial parameter. This can be expressed mathematically by the following equation:

$$\mu_r^2 \frac{\partial R}{\partial \mu_r^2} + \mu_r^2 \frac{\partial \alpha_S}{\partial \mu_r^2} \frac{\partial R}{\partial \alpha_s} = 0. \tag{1.23}$$

The partial derivative $\partial\alpha_s/\partial\mu_r^2$ defines the μ_r dependence of the of $\alpha_s(\mu_r)$ in terms of the β function of QCD which can be expanded in a power series of α_s

$$\mu_r^2\frac{\partial\alpha_s}{\partial\mu_r^2} = \alpha_s\beta(\alpha_S) = -\beta_0\left(\frac{\alpha_s}{4\pi}\right)^2 - \beta_1\left(\frac{\alpha_s}{4\pi}\right)^3 + \ldots .$$

where β_0, β_1 are the first coefficients occurring in the expansion. In the one loop approximation, i.e. regarding only the term with β_0, the coupling constant α_s can be written in terms of the renormalization scale as

$$\alpha_s(\mu_r^2) = \frac{4\pi}{\beta_0 \ln(\mu_r^2/\Lambda^2)}, \beta_0 = 11 - \frac{2}{3}N_f. \tag{1.24}$$

Here N_f is the number of (active) quark flavors which have masses smaller than μ_r and Λ denotes the free parameter of QCD which is of the order of $200 - 300$ MeV dependent on the number of active flavors and the renormalization scheme used to control the ultraviolet divergences as for example the frequently used $\overline{MS}$ scheme [BAR78].

From the formula 1.24 it can be seen that in QCD partons are asymptotically free, that is $\alpha_s \to 0$ as $\mu_r^2 \to \infty$, see Figure 1.3. This property is unique to non-Abelian gauge theories.

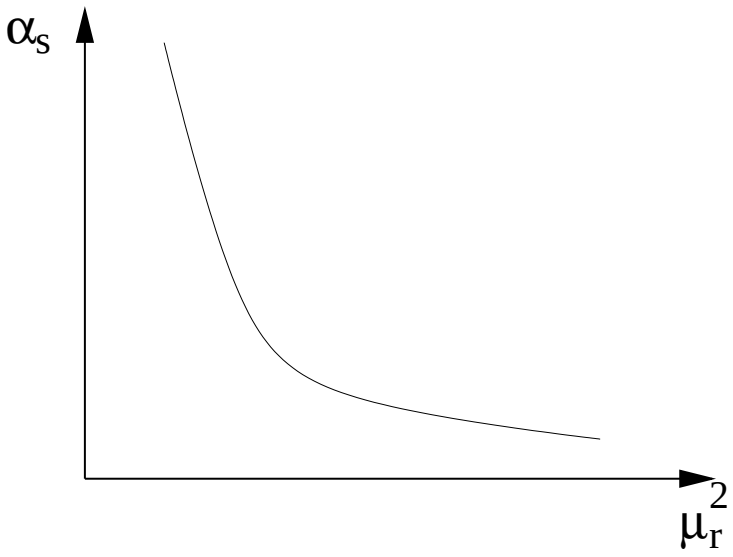

Figure 1.3: Schematic representation of the dependence of the strong coupling constant α_s on the renormalization scale μ_r^2.

Another important consequence of the non-abelian nature of QCD is that α_S increases with decreasing μ_r^2. It is believed that this increase of the strong force is one source for the (color) confinement of quarks and gluons inside hadrons, so called infrared slavery, which means that one cannot see the struck quark in an experiment but only an energetic jet of colorless hadrons emerging from it [GRO73].

The variation of α_s with μ_r^2, but not its absolute value, can be derived from QCD; the latter has to be fixed experimentally. The current world average of α_s was determined by the combination of various experimental results and is expressed at the energy scale of the rest mass of the Z^0-boson $\mu_r = M_Z$ [BET00]:

$$\alpha_s(M_z) = 0.118 \pm 0.003. \tag{1.25}$$

1.4 QCD Improved Parton Model

The observed deviations from the predictions of the naive quark parton model can be explained by the inclusion of QCD into the description of the deep inelastic scattering processes. The diagrams shown in Figure 1.4 are examples for corrections to first order in α_s to the total ep cross section. The radiation of gluons by quarks in the proton give rise to a gluon density $g(x)$ in the proton. However, the calculation of the matrix elements which correspond to the

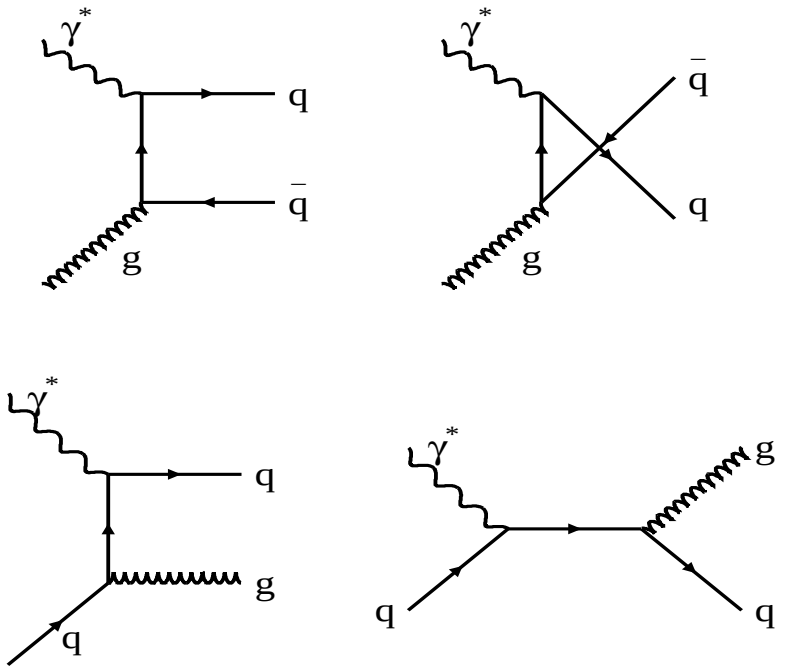

Figure 1.4: Feynman graphs of corrections to the order α_s in deep inelastic scattering. The upper graphs represent the boson-gluon fusion and the lower graphs represent the QCD Compton scattering

Feynman graphs in Figure 1.4 lead to divergences if partons are radiated either collinear to the incoming quark or gluon or with infinitely low energies. Following the factorization theorem of QCD [COL89], all collinear and infrared divergences can be absorbed into the (redefined) parton densities of the proton. The scale at which the hard scattering is separated from the soft and collinear processes happens is called the factorization scale μ_f. Therefore the parton densities become explicitly dependent on the scale μ_f, which is usually set to Q^2. This additional dependence of the parton densities is the reason for the observed scaling violations. The parton densities can not be calculated from first principles by QCD. They have to be obtained from some experimental input. Frequently used parameterizations of parton densities are those of the CTEQ collaboration [CTE97, CTE00] and the ones of Glück, Reya and Vogt (GRV) [GLU95, GLU98]. Once the parton densities are known at a given point in phase space, say Q_0^2, they can be evolved dynamically to another point Q^2 using perturbative QCD by means of so called evolution

equations. To derive the evolutions equations, one has to consider all contributions from all orders of perturbation theory. Since this is impossible, approximations have to be used which effectively sum up large logarithms like $\alpha_s \log(Q^2/Q_0^2)$ or $\alpha_s \log(1/x_B)$ (leading log approach) occurring in the perturbative expansions.

The most familiar attempt to evolve the parton densities, the so-called DGLAP evolution [GRI72, ALT77, DOK77], will be described briefly here. The DGLAP evolution equations are used to evolve the parton densities from a starting scale Q_0^2 to any other value of Q^2:

$$\frac{\partial f_i(x_B, Q^2)}{\partial \log Q^2} = \frac{\alpha_s}{2\pi} \int_{x_B}^{1} \frac{dx'}{x'} \left(f_i(x', Q^2) P_{qq}(\frac{x_B}{x'}) + g(x', Q^2) P_{qg}(\frac{x_B}{x'}) \right) \tag{1.26}$$

$$\frac{\partial g(x_B, Q^2)}{\partial \log Q^2} = \frac{\alpha_s}{2\pi} \int_{x_B}^{1} \frac{dx'}{x'} \left(\Sigma_i f_i(x', Q^2) P_{gq}(\frac{x_B}{x'}) + g(x', Q^2) P_{gg}(\frac{x_B}{x'}) \right). \tag{1.27}$$

The equations mathematically express the fact that a parton with momentum fraction x_B could have come from a parent parton with larger momentum fraction x'. The probability for parton i to radiate a parton j is given by the splitting functions, P_{qq}, P_{qg}, P_{gq} and P_{gg}. The splitting function P_{gg} gives the probability for a gluon to radiate another gluon and thus contains the self interaction of the gluons which is a consequence of the non-abelian nature of QCD.

Using a physical gauge, the evolution from the proton to the place of the hard scattering can be depicted by a ladder diagram as shown in Figure 1.5. The emitted partons in the ladder are ordered with respect to their transverse momenta, $Q^2 \gg ... \gg k_{t,i+1}^2 \gg k_{t,i}^2$, such that the hardest emission is given by the quark box at the top of the ladder. The longitudinal momenta on the other hand obey $x_{i+1} < x_i$. The DGLAP evolution equations effectively sum up terms proportional to $\alpha_s \log(Q^2/Q_0^2)$ which dominate the parton evolution if x_B is not too small.

An important test of the validity of the DGLAP evolution equations is the measurement of the proton structure function F_2 as a function of x_B and Q^2. It has been measured with high precision at HERA in a wide region of phase space. It is well described by a QCD fit based on the DGLAP evolution equations as can be seen in Figure 1.6 which shows a recent H1 measurement [KLE99] together with results from fixed target experiments (SLAC, NMC and BCDMS). The figure impressively demonstrates the important contribution of HERA experiments to the knowledge on the proton structure and therefore the understanding of the structure of matter in general. Especially, the described scaling violations, i.e. the dependence of F_2 on Q^2, can be seen very nicely from this data.

Note that, to obtain these results, no knowledge about the structure of the hadronic final state X is necessary. The investigation of the hadronic final state is a very important test of QCD by itself. The description of its detailed structure by QCD must be successful to claim QCD as the correct theory of the strong interaction.

1.5 Hadronization

The partons which emerge from the deep inelastic scattering process are not directly observable. Due to confinement the partons have to become color neutral hadrons if they are separated by more than approximately 1 fm. The transition from partons to hadrons is called hadronization. For distances larger than 1 fm the concepts of perturbative QCD are no longer valid and the transition from parton level to the hadron level presently has to be treated by phenomenological models. The final product of the hadronization process is a spray of particles collimated around the direction of the incident parton. Such a spray of particles is called a jet.

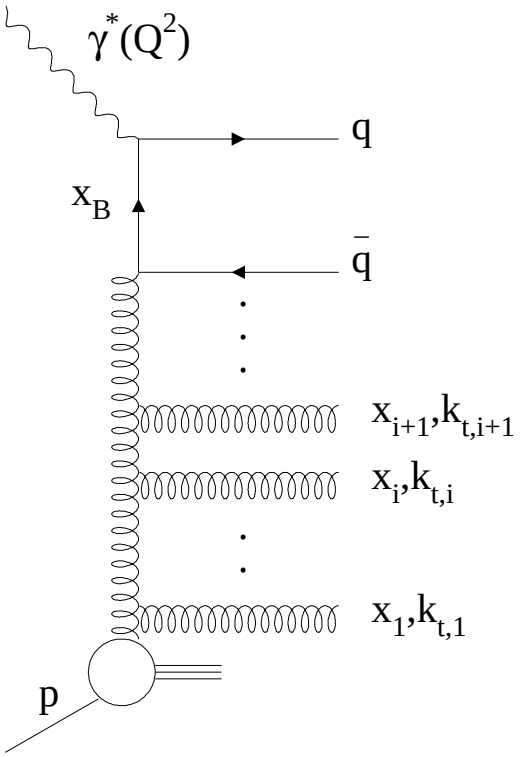

Figure 1.5: Ladder representation of a DIS process. The variables; k_t and x_i denote the transverse momentum and longitudinal momenta of the radiated partons, respectively.

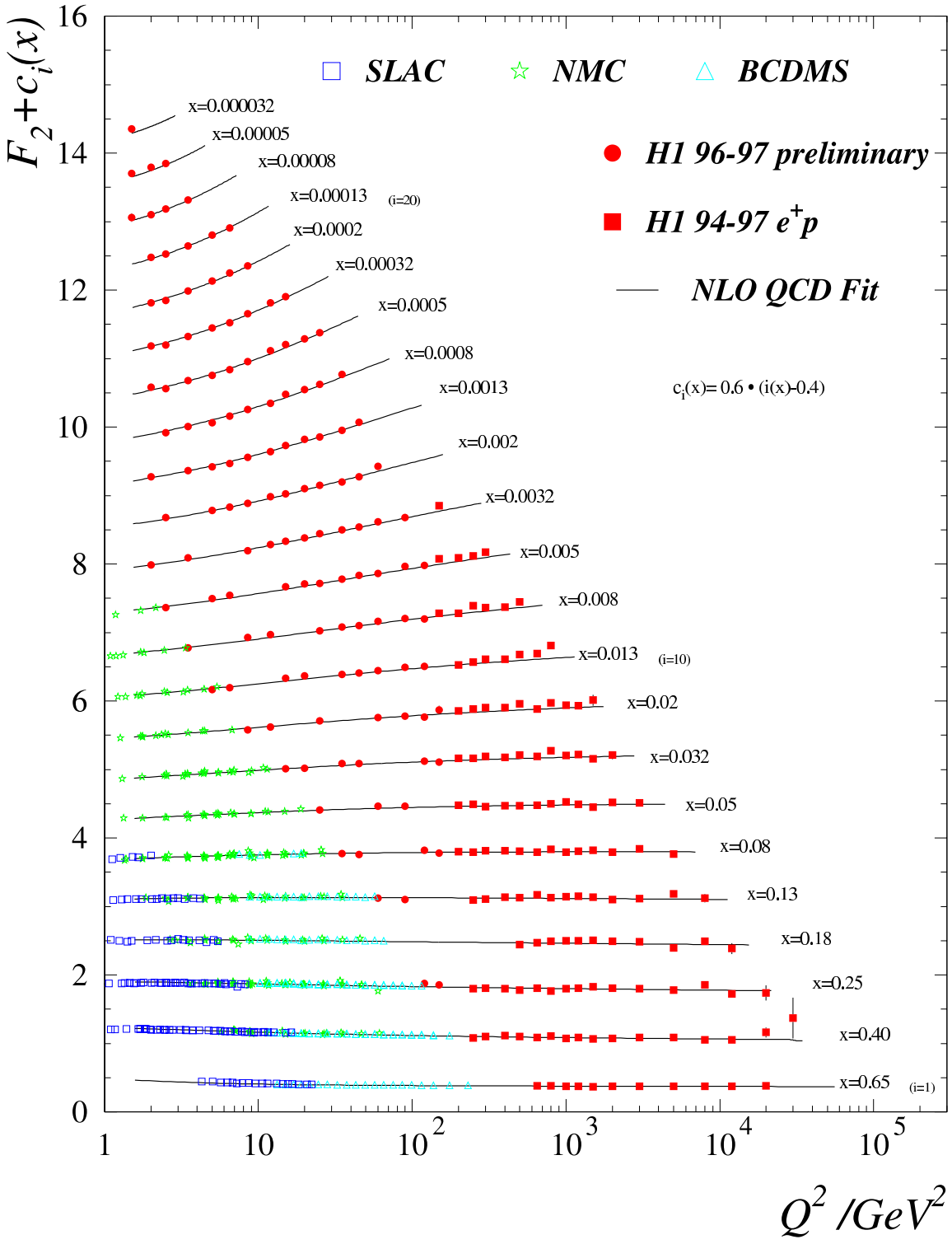

Figure 1.6: Proton structure function F_2 as a function of Q^2 for different ranges of x_B (denoted simply as x in the figure).

1.6 Jet Algorithms

The jet structure of an event is a footprint of the underlying hard scattering or short distance process between the virtual photon and a parton from the proton. Hadronization between the initial scattering and the measurement smears out the topology of the reaction. Jet algorithms attempt to establish a connection between the resulting event topology and the elementary hard subprocess. They group objects together according to a defined metric such that the constructed jets are related to the final state partons of the basic scattering process as closely as possible. Important requirements are:

- Infrared and collinear safety of the algorithm; i.e. the result of the algorithm must not change if a parton with infinitely low energy is added to an n-parton configuration and/or one parton of this configuration is split into two collinear partons.
- The algorithm must be able to separate the hard subprocess from soft interactions occurring in the event.
- It must provide small hadronization correction.

There is no unique procedure to define jets and a large variety of jet definitions have been proposed in the last decades, for a review see e.g. [MOR98]. Jet definitions can be grouped into clustering type algorithms which define jets by a successive recombination of pairs of particles in an iterative way and cone algorithms which define jets by maximizing the energy flow through a cone of fixed size. The algorithm used in this thesis, the longitudinally invariant k_t algorithm, has been shown to be a compromise between the two types of jet definitions [ELL93] and is described below.

1.6.1 The Longitudinally Invariant Inclusive k_t Algorithm

Originally the k_t algorithm was invented for e^+e^-collisions [CAT92]. It was then modified to be applicable also in hadron-hadron collisions [CAT93]. The variant used in this thesis was first proposed by Ellis and Soper [ELL93].

The idea behind the k_t-algorithm is to combine particles with nearly parallel momenta. These particles are regarded as part of a cascade of particle emissions with one of the final state partons at its origin. The experimental footprint of this cascade are local enhancements in the energy flow produced by energy depositions of particles which have only small distances in η and ϕ relative to each other.

The algorithm starts with a list of objects belonging to the hadronic final state. These objects might be the partons emerging from the hard subprocess, final state hadrons simulated by an event generator or experimentally measured quantities like clusters of energy depositions in a detector. The objects are called protojets and in the end will be merged into one or more final jets. Each protojet is characterized by its transverse energy $E_{t,i}$, its azimuthal angle ϕ_i and its pseudo rapidity η_i. The jet algorithm depends on a distance parameter R which controls the relative distance within which protojets merged into a new object. The value of R is set to 1 according to the recommendation in [ELL93]. In detail, the algorithm proceeds as follows (see also [ELL93]):

1. For each protojet define

$$d_i = E_{t,i}^2. \tag{1.28}$$

2. For each pair of protojets define the distance

$$d_{ij} = \min(E_{t,i}^2, E_{t,j}^2)[(\eta_i - \eta_j)^2 + (\phi_i - \phi_j)^2]/R^2. \tag{1.29}$$

3. Find the smallest of all the d_i and d_{ij} and label it d_{min}.

4. If d_{min} is given by a d_{ij} then merge i and j into a new protojet k which is then added to the list while i and j are removed from the list. The merging of the particles is performed according to a specific recombination scheme. Here the so called 'E_t – scheme' (Snowmass convention [HUT90]) is used with

$$E_{t,k} = E_{t,i} + E_{t,j} \ , \tag{1.30}$$

$$\eta_k = \frac{[E_{t,i}\eta_i + E_{t,j}\eta_j]}{E_{t,k}}, \tag{1.31}$$

$$\phi_k = \frac{[E_{t,i}\phi_i + E_{t,j}\phi_j]}{E_{t,k}}. \tag{1.32}$$

5. If d_{min} is given by a d_i the corresponding protojet is removed from the list and added to the list of jets.

This procedure continues until there are no protojets remaining. At the end one receives a list of jets with successively increasing $E_{t,i}^2$.

1.6.2 Choice of the Reference Frame

In the laboratory frame partons emerging from a deep-inelastic scattering process may gain transverse momentum in two ways: (a) by balancing the transverse momentum of the scattered positron, (b) by radiating partons induced by an underlying QCD process. In a reference frame where the parton from the proton collides head on with the virtual photon the only source for jet production is the underlying QCD process[2], as depicted in Figure 1.7. In the naive quark-

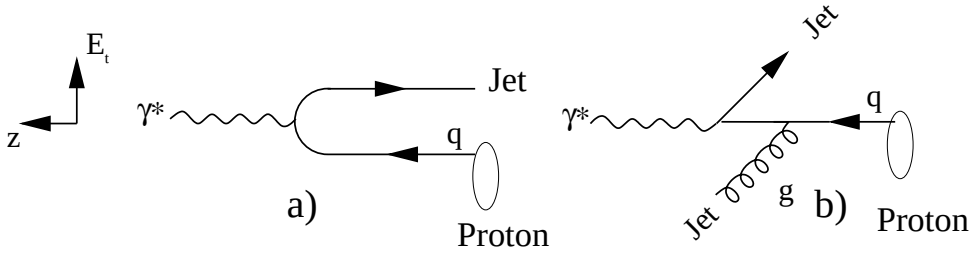

Figure 1.7: The figure shows in (a) a parton model diagram for $\gamma^* q \to q$, producing a jet with $E_t = 0$ and in (b) a gluon emission diagram which produces jets with $E_t \neq 0$.

parton model, final state hadrons are produced in the direction of the virtual photon. But, if the quark emits a gluon, as for example in the QCD Compton process, the quark recoils against the radiated gluon and two jets are produced each of which can have a large transverse energy relative to the direction of the incoming quark or proton.

[2]This statement is strictly speaking only true if the primordial transverse energy of the partons in the proton which is of the order of 300 – 600 MeV [GEI90] is small compared to the minimal transverse energy required for the final state jets.

Figure 1.7 suggests that an appropriate frame in which to study QCD by means of the transverse energies of the final state particles is the center-of-mass frame, which is defined by the virtual boson and the parton, also called partonic cms. In this frame the only source for transverse energy is the photon parton subprocess. Unfortunately, a boost from the laboratory frame to the partonic cms is not practicable since the momentum fraction ξ of the initial parton participating in the process is not known a priori. However concerning measurements of the transverse momentum every frame whose z axis coincides with that of the partonic cms seems to be suited. Since the initial state partons move (to a first approximation) collinear with the incoming proton direction an equally suited frame is given by the center-of-mass frame defined by the proton and the virtual boson, called hadronic center-of-mass frame or $\gamma^* p$-frame, which will be used in this analysis.

1.7 Dijet Cross Section

An event with two jets in the final state is characterized by additional kinematic variables beside the DIS variables defined in Section 1.1. These additional variables are introduced in the following:

- The variable ξ defines the momentum fraction of the incoming parton on the proton and is in general not equal to x_B
- The partonic scaling variable x_p is defined as:

$$x_p = \frac{Q^2}{2\xi pq} = \frac{x_B}{\xi} \tag{1.33}$$

  and interpreted as the momentum fraction of the parton which interacts with the virtual photon relative to the momentum fraction ξ of the incident parton.

- The center-of-mass energy in the photon-parton center-of-mass frame is defined as

$$\hat{s} = (\xi p + q)^2 = Q^2(\frac{\xi}{x_B} + 1) = Q^2(\frac{1}{x_p} - 1) \ . \tag{1.34}$$

- The polar angle θ of the outgoing parton is expressed by the Lorentz-invariant quantity z_q according to

$$z_q = \frac{pp_q}{pq} = \frac{1}{2}(1 - \cos\theta) \tag{1.35}$$

  where p_q defines the momentum of the outgoing parton.

- The transverse energy E_t of the outgoing partons can be expressed by $\hat{s}$ and z_q:

$$E_t^2 = \hat{s} z_q (1 - z_q). \tag{1.36}$$

To first order in α_s, the final state of the partons can be expressed by three independent variables, e.g. by x_p, z_q and the azimuth angle of the outgoing partons and the differential cross section for two partons in the final state integrated over the azimuthal angle, can be written as [MEN78]:

$$\frac{d^2\sigma_{2jet}}{dx_B dQ^2} \propto \alpha_S(\mu_r^2) \int_0^1 \frac{d\xi}{\xi} \left\{ C_{qg}(x_B/\xi, z_q, x_B, Q^2) f(\xi, \mu_f^2) + C_{q\bar{q}}(...) g(\xi, \mu_f^2) \right\}. \tag{1.37}$$

Here, f and g represents the quark or gluon density at a given phase space point ξ and μ_f^2, respectively. The coefficient functions C_{qg} and $C_{q\bar{q}}$ represents the hard part of the scattering which can be calculated by perturbative QCD and contain the cross sections for the boson gluon fusion and the QCD Compton process. The differential cross sections, integrated over the azimuthal angle for the boson gluon fusion and the QCD Compton process normalized to the total cross section σ_{DIS} can be written as [PEC80], [RUM81], [LON95]:

$$\frac{d\sigma_{q\bar{q}}}{\sigma_{DIS}} = \frac{2\alpha_s}{3\pi}\frac{f_q(\xi,Q^2)}{f_q(x_B,Q^2)}\left(\frac{z_q^2+x_p^2}{(1-z_q)(1-x_p)} + 2(x_p z_q+1) + \frac{8x_p z_q(1-y)}{1+(1-y)^2}\frac{dx_p}{x_p}dz_q\right) \tag{1.38}$$

$$\frac{d\sigma_{qg}}{\sigma_{DIS}} = \frac{\alpha_s}{4\pi}\frac{g(\xi,Q^2)}{f_q(x_B,Q^2)}\times \left(\frac{(x_p^2+(1-x_p)^2)(z_q^2+(1-z_q)^2)}{z_q(1-z_q)} + \frac{(x_p^2+(1-x_p)^2)(z_q^2+(1-z_q)}{1+(1-y)^2}\frac{dx_P}{x_p}dz_q\right). \tag{1.39}$$

Both expressions are divergent for $z_q \to 0$ and $z_q \to 1$, respectively. In this case the partons are emitted collinear to the incoming or outgoing parton. Another divergence occurs for the QCD Compton process if $x_B \approx \xi$ or $x_p \approx 1$. This reflects the increasing probability for the radiation of soft gluons. These divergences can be avoided by requiring a minimum E_t for the outgoing partons.

The previous considerations and formulae show that the dijet cross section σ_{2jet} is directly proportional to the strong coupling constant α_s. The experimental determination of the dijet cross section therefore provides a more direct test of QCD than the determination of F_2 via inclusive measurements. A widely used observable to study dijet production is the dijet rate R_2 which is defined as:

$$R_2 = \frac{\sigma_{2jet}}{\sigma_{DIS}}. \tag{1.40}$$

Note, that in leading order, the dijet cross section depends implicitly, i.e. by α_s, on the parameter μ_r^2 and Equation 1.23 therefore cannot be fulfilled. Any leading order prediction can only be expected to describe the order of magnitude and the rough features of the dijet cross section. Any reliable prediction has therefore to be based on NLO calculations, i.e. by including the diagram shown in Figure 1.8 in addition to those shown in Figure 1.4. This means that the coefficient functions given in Equation 1.37 become explicitly dependent on the artificial scale μ_r^2. By this the dependence of the theoretical predictions on μ_r^2 due to the running coupling is partially balanced such that the renormalization scale uncertainties become small with respect to leading order predictions. Nevertheless a residual scale dependency remains which is the reason why the correct choice of μ_r^2 is still a matter of discussion. It is clear that μ_r^2 has to be large such that α_s remains small to justify the perturbative treatment of the theory. For the study of dijet events in DIS, at least two scales are suggested by the nature of the process. The first is the four-momentum transfer Q^2 while the other possible scale for jet production is the transverse energy of the outgoing jets. It is not clear a priori which choice of scale is better suited to describe dijet production in DIS and the answer can only be given by comparing measured dijet quantities to theory.

In addition to the 'scale problem' mentioned above, further considerations have to be taken into account when dealing with NLO QCD calculations. To generally avoid regions of phase space where the cross sections diverge, i.e. where partons are emitted collinear to the incoming or outgoing partons or with very small energies, a minimum requirement on the transverse energy $E_{t,cut}$ for the final state partons or jets is demanded. In earlier dijet analyses it has been common

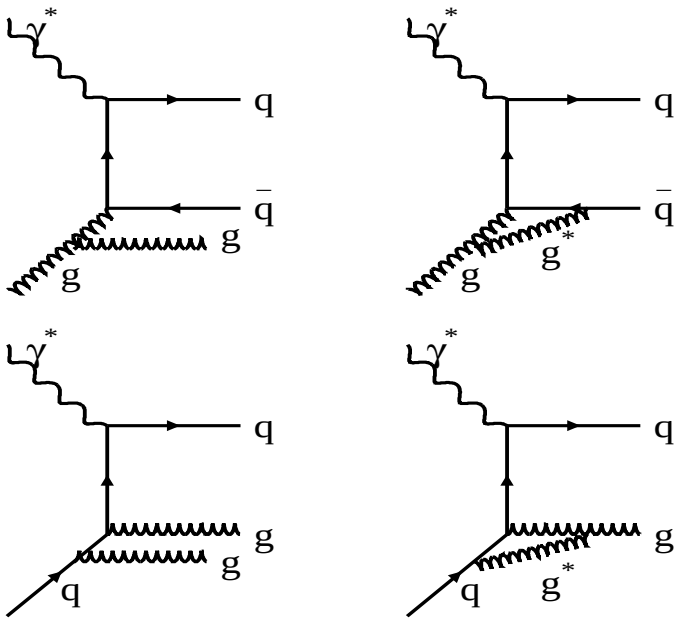

Figure 1.8: Real and virtual corrections to the leading order processes shown in Figure 1.4. They lead to order α_s^2 contributions to the dijet cross section.

practice to require the same $E_{t,cut}$ value for both of the outgoing jets. However, virtual corrections result in negative contributions to the calculated cross sections. These negative contributions have to be balanced by real emissions from the outgoing parton leg. If the required minimum transverse energy is equal for both final state partons/jets, there might not be enough phase space left for the additional emission of gluons without letting one of the two jets fall below the required threshold. In this case the real corrections do not balance the virtual corrections which lead to an infrared sensitivity of the predictions. To avoid this infrared sensitive region, it has been proposed [KLA96, FRI97] to apply asymmetric cuts on the outgoing partons or jets. Thus,

$$E_{t,jet1} > (E_{t,cut} + \Delta) \text{ with } \Delta > 0$$
$$E_{t,jet2...n} > E_{t,cut} \ .$$

As an example, the dependence of the dijet cross section calculated in NLO QCD is depicted in Figure 1.9 as a function of the introduced threshold parameter Δ. Contrary to naive expectations

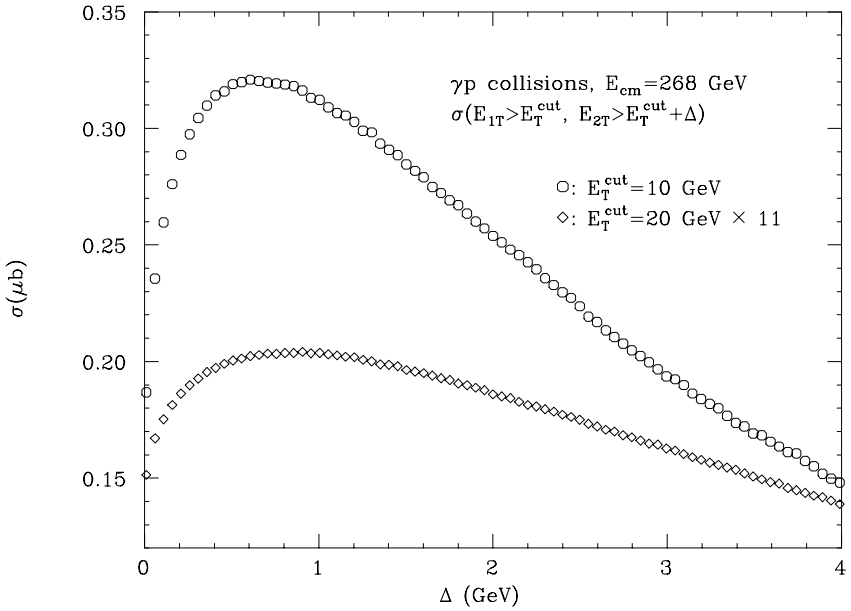

Figure 1.9: Example for the behavior of the dijet cross section calculated in NLO QCD as a function of the threshold parameter Δ. The figure is taken from [FRI97].

the cross section decreases as Δ approaches zero. This illustrates the unphysical behavior of the predictions if the perturbative series is only evaluated to a finite order. This is a problem of any fixed order calculation and can only be solved by resumming the perturbation series to all orders and/or taking non-perturbative effects into account. A detailed discussion of problems at exclusive boundaries in the phase space can be found in [FRI97] and [CAT97-1].

If dijet production is investigated from a symmetric to a largely asymmetric cut scenario, the QCD prediction can be tested from a region where it needs improvement to a region where it can be expected to be highly predictive. Such a measurement, therefore, is an important test of the actual status of the theory and might help to improve upcoming QCD predictions.

1.8 Alternative Concepts for Parton Evolutions

So far only the concept of a DGLAP evolution which assume a strong ordering in the transverse momenta of the emitted partons inside a parton ladder (see Figure 1.5) has been considered.

However, there are several other methods to describe initial state parton emission before the hard scattering process, potentially improving cross section predictions in regions where the basic assumption of strong k_t-ordering is no longer valid, e.g. at low x_B. As mentioned in the previous section, dijet production in deep inelastic scattering provides two important scales which characterize the scattering process, namely the virtuality of the photon Q^2 and the transverse energy E_t of the outgoing parton/jet. The presence of a second hard scale violates the requirement $Q^2 \gg k_{t,i}^2$ which is crucial for the validity of the DGLAP expansion. In the following, two approaches are introduced which are commonly used to describe the parton emissions in the presence of two hard scales.

1.8.1 Virtual Photon Structure

The photon is the elementary gauge boson of QED. From γp interactions where the γ is nearly on-shell, it is well established that a photon has a hadronic structure. In an intermediate state the photon can fluctuate into a $q\bar{q}$ pair. If the interaction time, say characterized by the E_t of the outgoing parton/jet, between the proton and the photon is much smaller than the fluctuation time t_f of the $q\bar{q}$ pair it will interact with the proton and give rise to a hadronic structure of the photon. The fluctuation time for high energy photons with virtuality Q^2 into a $q\bar{q}$ pair can be estimated from the uncertainty principle [IOF69] by

$$t_f \propto \frac{1}{Q^2 + (m_{q\bar{q}})^2}. \tag{1.41}$$

As Q^2 increases, t_f becomes smaller and the photon retains its structure-less character. In its resolved state, i.e. probing its structure at a scale $E_t^2 \gg Q^2$, the photon can fluctuate either into an on-shell $q\bar{q}$ pair forming a vector meson, so called Vector Dominance Part, or an off-shell $q\bar{q}$ pair, so called anomalous part, which can undergo strong interactions with other particles around.

Once the hadronic structure of the photon has been recognized, it is a natural step forward to parameterize this structure in terms of parton densities of the photon, analogous to the parton densities of the proton (for a review see e.g. [ERD97]). For quasi-real photons ($Q^2 \approx 0$) the parton densities are of the form $f_i^\gamma(x_\gamma, E_t^2)$ where x_γ is the fraction of the photon momentum carried by the interacting parton. The parameterization of the photon structure must be formulated such that the photon becomes less resolvable if the virtuality of the photon becomes comparable to the hard scale which is used to test its structure. Several proposals exist to realize this suppression of the photon structure, see e.g. [DRE94, SAS95, GLU99]. Figure 1.10 shows a measurement by the H1 collaboration of parton densities in the photon as a function of Q^2, compared to the predictions of Schuler and Sjöstrand [SCH96]. Here, the suppression of the partonic structure of the photon with increasing Q^2 is clearly visible.

Taking the internal structure of the photon into account, the ladder diagram given in Figure 1.5 is modified such that the hardest emission may occur anywhere in the ladder with increasingly soft emissions along the ladder towards the proton and the photon, as shown in Figure 1.11. The inclusion of the photon structure leads therefore to an artificial breaking of the strong k_t ordering which is demanded by the DGLAP evolution scheme and mimics an alternative type of parton evolution. Taking this alternative type of parton evolution into account the resolved contributions may enlarge the production of dijet events.

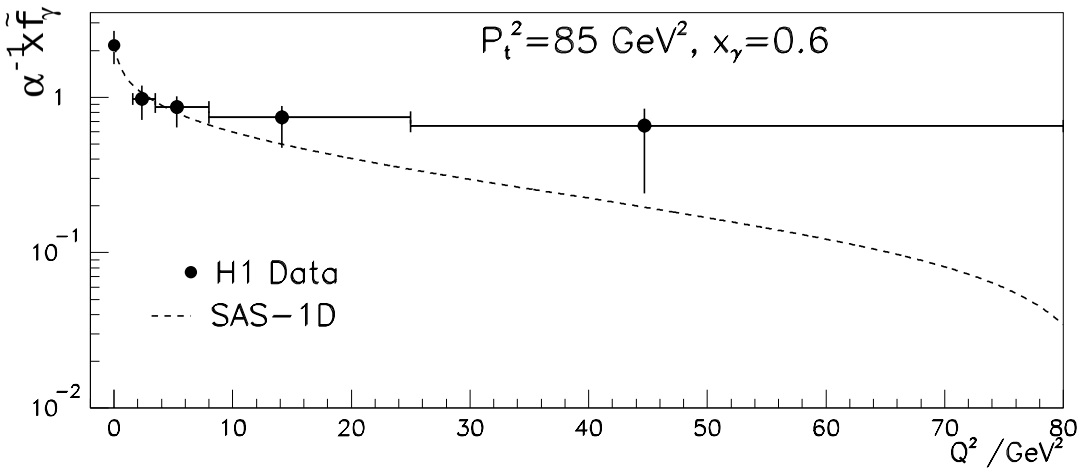

Figure 1.10: Example for the behavior of parton densities of the virtual photon (denoted as $q+\frac{9}{4}g$) as a function of Q^2 for fixed fractional momentum x_γ of a parton on the photon momentum and a jet E_t^2 of 85 GeV^2 (denoted as P_t^2 in the figure). The results are taken from [H1C00].

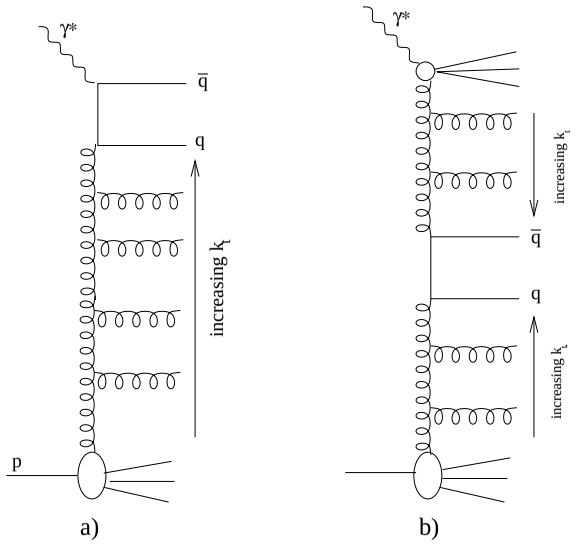

Figure 1.11: Different k_t ordering in the parton ladder between direct (a) and resolved γ^* (b) processes.

1.8.2 BFKL Evolution

An interesting situation occurs if the E_t^2 of the outgoing partons and the virtuality of the photon Q^2 are of the same size because then the conditions for DGLAP parton evolution are not fulfilled and the radiation of partons in the ladder diagram would be suppressed.

However, there are contributions proportional to $\alpha_S \log(1/x_B)$ which, while neglected in the DGLAP evolution, might become important if $Q^2 \approx E_t^2$. Their contribution is considered in another type of evolution equations, called BFKL (Balitsky, Fadin, Kuraev, Lipatov) evolution equations [KUR72]. In these evolution equations mainly $\alpha_s \log(1/x_B)$ terms are summed up. The onset of BFKL effects is expected in the low x_B regime where the $\alpha_s \log(1/x_B)$ contributions are expected to be large. In contrast to the DGLAP type of evolution equations, they require a strong ordering in the longitudinal momenta, $x_{i+1} \ll x_i$ and no ordering in k_t in the ladder depicted in Figure 1.5. It is argued in [KWI99] that the inclusion of BFKL type parton evolutions may enhance the dijet cross section at small x_B.

1.9 Monte Carlo Models

In order to compare theoretical assumptions with data one needs Monte-Carlo programs. Monte Carlo generators are able to predict details of the structure of multi particle final states observed in an experiment. Presently available programs include the matrix elements up to $O(\alpha_s)$ (Figures 1.1, 1.4); they generate the partonic final state using a technical implementation of one of the evolution equations mentioned above which leads to a good approximation of higher order effects without having to calculate the whole perturbation series. Since there is presently no generator embedding the BFKL equation, the parton shower development is mainly based on the DGLAP evolution equations. However, more phenomenological approaches to generate a parton shower exist. For the generation of the final state hadrons two types of phenomenological models exist: the string fragmentation and the independent cluster fragmentation [WEB84]. In the following a brief introduction to those Monte Carlo generators used in this thesis will be given.

1.9.1 RAPGAP

The program RAPGAP [JUN95] generate the ep process including the order α_s matrix elements represented by the Feynman graphs in Figure 1.4. In order to simulate higher order contributions the matrix elements are complemented with leading logarithm parton showers based on the DGLAP equations. In addition, the program allows the inclusion of resolved virtual photon configurations. The hadronization step is realized via an interface to the program JETSET [SJO86]. This program provides the transition from partons to hadrons using the LUND string model [AND83] and the decay of short-living hadrons. The incorporation of QED corrections is realized via an interface to the HERACLES [KWI92] program.

1.9.2 ARIADNE Color Dipole Model

The color dipole model (CDM), [AND89], [LON95], was originally developed for e^+e^- reactions. The basic idea is that the quarks produced in an annihilation process represent a color dipole which subsequently radiates gluons. The radiation leads to additional dipoles which again radiate partons resulting in a parton cascade.

In the case of ep scattering the color dipole is built by the struck quark and the proton remnant. The amount of the emissions is controlled by the extension of the proton and the

photon. Since both are considered to be extended objects the radiation is suppressed according to steering parameters which quantify this extension. By construction only the QCD Compton diagram can be embedded naturally into the algorithm. The boson gluon fusion process therefore has to be realized by allowing the radiation of an anti-quark from the primary dipole. The generation of parton showers in the framework of the dipole model produces no k_t ordering of the emitted partons. Thus, it follows closely the philosophy of the BFKL parton evolution. The hadronization step is realized by JETSET.

1.9.3 LEPTO

The event generator LEPTO [ING92] contains both, the QCD Compton and the boson gluon fusion matrix elements. Leading logarithm parton showers based on DGLAP evolution equations are implemented in the program to simulate higher order contributions. The hadronization is, like in RAPGAP, realized by the Lund fragmentation scheme using JETSET.

1.9.4 DJANGO

The generator DJANGO [SCH92] allows the incorporation of QED corrections to the order α^3 in the evaluation of the ep cross sections. DJANGO is used in combination with the programs HERACLES [KWI92], LEPTO, ARIADNE and JETSET. HERACLES generates the deep inelastic events which include electromagnetic corrections to the order α. Then, a matrix element of the order $\alpha\alpha_s$ is generated which is then transferred to e.g ARIADNE to generate the QCD parton cascade. Simulated and reconstructed Monte Carlo events from DJANGO are used in this analysis for the correction of the data for QED radiation effects and will be denoted as DJANGO/CDM in this thesis.

1.10 Analytical Calculations

In general the implementation of a NLO calculation for jet cross sections in a computer program faces several difficulties. The phase space integrals which have to be performed are too complicated to be treated analytically and therefore must be subject to numerical integrations. Before they can be performed the singular parts which come along with infrared and collinear divergences in the real and virtual contributions have to be integrated out numerically.

1.10.1 DISENT

The program DISENT [CAT97-2] calculates dijet cross sections to the order α_s^2. It assumes a point-like structure of the virtual photon. The matrix elements which are listed in the Tables 1.1 and 1.2 under the column 'direct' are implemented in the program.

direct	resolved		
$\gamma^* q \to qg$	$qq' \to qq'$	$qq \to qq$	$qg \to qg$
$\gamma^* g \to q\bar{q}$	$q\bar{q}' \to q\bar{q}'$	$q\bar{q} \to q\bar{q}$	$gg \to gg$
	$qq' \to q'\bar{q}'$	$q\bar{q} \to gg$	$gg \to q\bar{q}$

Table 1.1: Two parton final state subprocesses.

direct	resolved		
$\gamma^* q \to qgg$	$qq' \to qq'g$	$qq \to qqg$	$q\bar{q} \to ggg$
$\gamma^* g \to q\bar{q}g$	$q\bar{q}' \to q\bar{q}'g$	$q\bar{q} \to q\bar{q}g$	$gg \to q\bar{q}g$
$\gamma^* q \to qq'\bar{q}'$	$q\bar{q} \to q'\bar{q}'g$	$qg \to qq\bar{q}$	$gg \to ggg$
$\gamma^* q \to qq'\bar{q}'$	$qg \to qq'\bar{q}'$	$qg \to qgg$	

Table 1.2: Three parton final state subprocesses.

In DISENT the control of the infrared divergences is realized by the subtraction method. A so called counter term is calculated and properly subtracted from the real and virtual contributions to the NLO cross sections.

1.10.2 JETVIP

The program JETVIP [POE97] calculates dijet cross sections in next-to-leading order QCD as well . In contrast to the above described program DISENT, it allows contributions from a resolved virtual photon to be incorporated in the NLO calculations. Therefore, all the subprocesses listed in Tables 1.1 and 1.2 are implemented in the program. It is so far the only existing program which provides calculations in NLO for direct and resolved interacting photon processes using parameterizations of the virtual photon structure function. It is therefore extremely useful in a kinematic regime where the E_t^2 of the partons in the final state is similar or larger than the Q^2 of the virtual photon.

The calculations are based on a phase space slicing method. In this method the singular phase space regions of soft and collinear final state particles are separated by introducing an invariant mass cut-off y_{cut}. The finite phase space regions outside the cut-off are treated numerically and can be subject to a variety of experimental cuts and jet definitions.

A further discussion about the applicability of the concept of a virtual photon structure if Q^2 is well above the photoproduction limit $Q^2 \gg m_\rho$, where m_ρ is the mass of the ρ meson, will be given in Chapter 5 where the predictions of JETVIP are confronted with the results of the analysis performed in this thesis which cover the range $5 < Q^2 < 100\,\mathrm{GeV}^2$.

1.11 Concluding remarks

In order to test the reliability of QCD predictions concerning dijet production in deep inelastic scattering the dijet rate R_2 is measured in the phase space region $5 < Q^2 < 100\,\mathrm{GeV}^2$ and $10^{-4} < x_B < 10^{-2}$. The measurement presented in this thesis follows a study published by the H1 collaboration of a single differential measurement of R_2 [H1C98]. It benefits from the increased statistics and the improved experimental apparatus which allows the extension of the measurement to phase space regions which were only partly covered by the previous analysis. By this it is possible to study the following two issues:

- For the first time a double differential measurement of R_2 as a function of x_B in bins of Q^2 is shown. If Q^2 is kept fixed one might get sensitive to the small x_B dynamics responsible for dijet production. This would allow the possibility to distinguish between DGLAP from alternative types of parton evolutions which can for example be realized by adding contributions from a resolved virtual photon to the dijet cross section. The measurement will be compared to predictions of NLO calculations. Therefore an asymmetric cut on the jet

E_t becomes necessary and $\Delta = 2\,\mathrm{GeV}$ is chosen as the central cut scenario. It was shown that for this cut scenario the NLO predictions are safe [POE99].

- In addition the double differential R_2 is studied as function of Δ. This allows the dependence of dijet production as a function of the transverse energy of the jets to be studied. If Δ is used to parameterize the E_t dependence, the measurement will cover a range in phase space from where NLO QCD calculations need improvements to where it is believed to be make accurate predictions.

In summary the measurement will be a extremely detailed and precise test of the predictions of perturbative QCD. It will reveal the huge predictive power of the theory as well as bring up points where the theory definitely needs improvement. The correct description of the measurement presented here will be a great challenge for the theory.

Chapter 2

HERA and the H1 Detector

In this chapter, the accelerator HERA and the H1 experiment are introduced. After a brief description of the HERA machine, an overview of the H1 detector in its 1996/97 setup is given with focus on those components which are essential for the analysis presented in this thesis.

2.1 The HERA Accelerator

The Hadron-Elektron-Ring-Anlage HERA is the first storage facility ever built to provide colliding beams of electrons or positrons[1] and protons. It consists of two independent storage rings with 6.3 km circumference each. The beam energies[2] are 27.5 GeV for positrons and 820 GeV for protons, leading to a center of mass energy of $\sqrt{s} \approx 300\,\text{GeV}$ available for the positron-proton collision. Two experiments, named H1 and ZEUS, make use of the colliding mode of the accelerator. They are located in the north hall (H1) and in the south hall (ZEUS). A third experiment, HERA-B, is located in the west hall and uses the proton beam to study CP violation. Finally, the HERMES experiment (east hall) is studying the spin structure of the proton with the positron beam. The layout of the HERA machine, together with the injection system is illustrated in Figure 2.1.

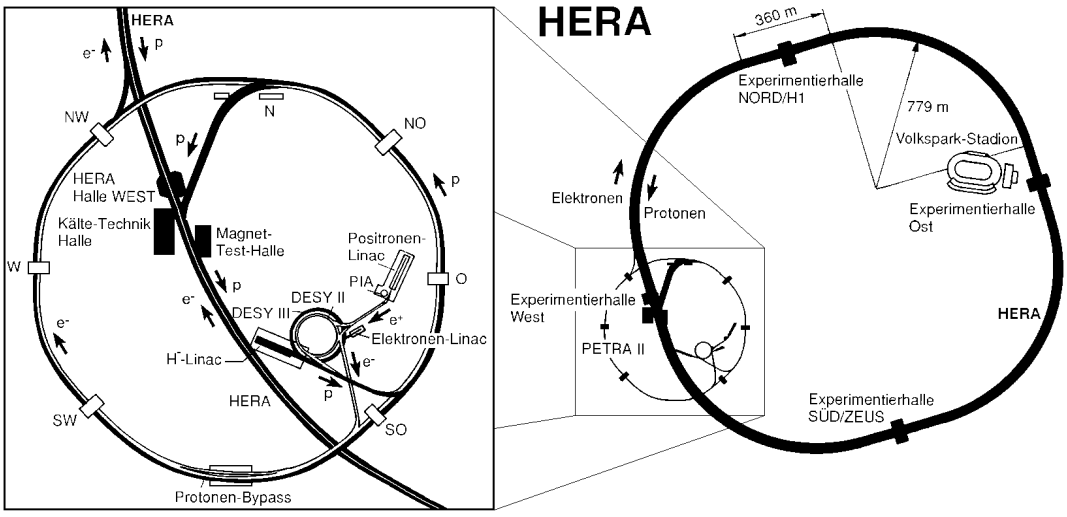

Figure 2.1: Schematic overview of the HERA accelerator complex.

[1] In the data taking periods relevant for this analysis HERA was operated with positron beams.
[2] From 1998 on the proton beam energy is 920 GeV

2.2 The H1 Experiment

The H1 collaboration has constructed a general purpose detector, consisting of a number of complex subdetectors. These are designed to provide both complementary and redundant measurements of various aspects of final states in high-energetic positron-proton collisions. A schematic view of the detector is given in Figure 2.2. After a brief overview, the components relevant for this analysis are described in more detail. A detailed description of the H1 detector can be found in [H1C96]. The components of the detector are arranged cylindrically symmetric around

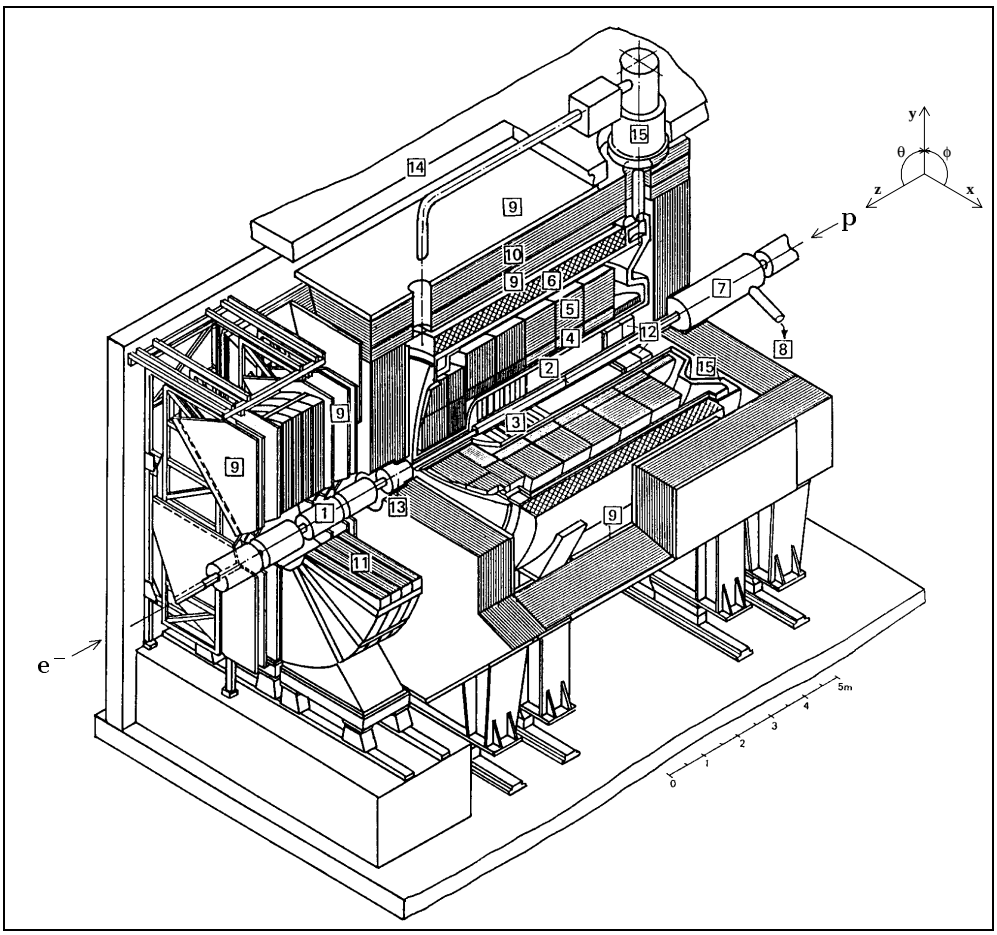

1 Beam pipe and beam magnets	9 Muon chambers
2 Central tracking device	10 Instrumented iron yoke
3 Forward tracking device	11 Forward muon toroid
4 Electromagnetic LAr calorimeter	12 Backw. calorimeter (SpaCal)
5 Hadronic LAr calorimeter	13 PLUG calorimeter
6 Superconducting coil (1.15 T)	14 Concrete shielding
7 Compensating magnet	15 Liquid argon cryostat
8 Helium supply for 7	

Figure 2.2: Three dimensional view of the H1 detector

the beam axis. The center-of-mass frame of the positron proton collisions is strongly boosted in the outgoing proton direction leading to a better instrumentation of the detector in that direction. The direction of the outgoing proton defines the positive z-axis of the right handed H1 coordinate frame.

The proton and electron beams collide within the beam pipe(1) at a well defined interaction point which is marked with a cross in Figure 2.2. The beam pipe is surrounded by a system of central (2) and forward (3) drift chambers to measure the tracks of charged particles in the polar angle region between $5^o < \theta < 155^o$. The energy of charged and neutral particles is measured in a highly segmented liquid argon calorimeter (4,5) which surrounds the central and forward tracking system. It is divided into a inner so called electromagnetic calorimeter (4) and outer so called hadronic calorimeter (5). Both calorimeters are embedded in a cryostat which keeps the liquid argon at a temperature of 88^oK. In the very forward direction a further calorimeter, the PLUG (13), is installed.

The cryostat is surrounded by a superconducting coil (6) which provides a magnetic field of 1.15 T parallel to the beam pipe. The iron return yoke (10) provides the return path for the magnetic field. It is instrumented with streamer tubes which complete the energy measurement of the liquid argon calorimeter and which are used for muon identification. The influence of the magnetic field on the beam orbits is balanced by a compensating magnet (7). A toroidal magnet installed in the proton direction provides additional capabilities for the detection of muons which leave the interaction point under small polar angles.

In the direction of the incoming positron beam, at polar angles $153^o < \theta < 178^o$, the H1 detector is equipped with a backward drift chamber (BDC) which is mounted in front of a lead scintillating/fiber calorimeter SpaCal (12). These detector components enable precise measurements of the scattered positron.

All detector components provide complementary information on the reaction products. The components relevant for the studies presented in this thesis will be described briefly in the following.

2.3 Central and Forward Tracking System

The forward and central tracking system shown, schematically in Figure 2.3, is designed for the reconstruction and momentum measurement of tracks produced by charged particles. Momentum reconstruction is possible since trajectories of charged particles are bent in the magnetic field of 1.2 T provided by the super conducting coil.

The basis of the central tracking system, which covers the polar angle region $25^o < \theta < 155^o$, are two large concentric drift chambers named CJC1 and CJC2. Their active length along the z-direction is 220 cm. Their radial coverage is between 203 mm and 451 mm. The CJC1 contains 30 drift cells with 24 sense wires each and the CJC2 contains 60 cells with 32 wires each. The signals recorded in the chambers are used to determine the transverse track momentum and provide information about the specific energy loss dE/dx for particle identification. The spatial resolution in the $r-\phi$ plane is about 170 μm. A resolution of 2.2 cm is achieved in the z-coordinate measurement by comparing the signal amplitudes read out at both wire ends ('charge division' technique).

Two additional drift chambers (4 layers each) with wires perpendicular to the beam axis measure the z coordinate with better precision than achieved by the charge division technique. These chambers, the so-called central inner (CIZ) and central outer (COZ) z-chamber, are located inside and outside the CJC1 and complete the measurement of the track momenta.

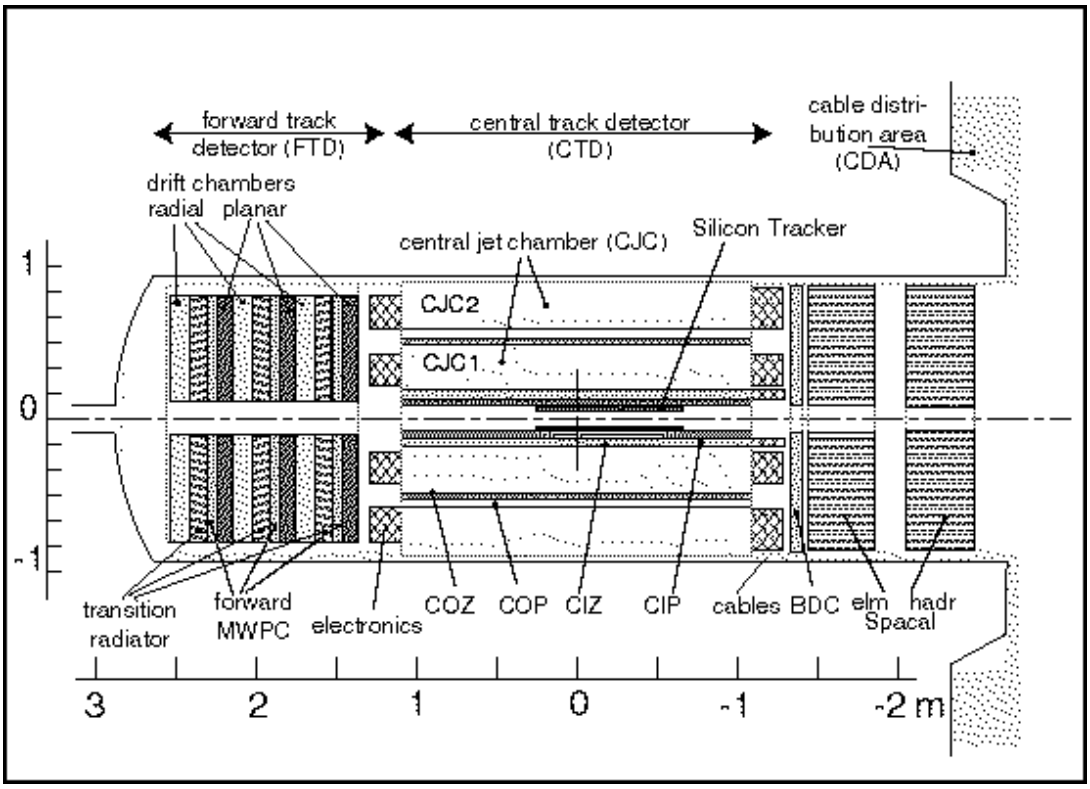

Figure 2.3: Side view of the H1 tracking system.

They provide a resolution of typically 300 μm in z and about five degrees in ϕ. The momentum resolution achieved by combining the measurements of all four chambers is $\sigma_p/p^2 < 0.01\,\mathrm{GeV}^{-1}$.

The central tracking system is completed by two multi-wire proportional chambers (MWPC) named CIP and COP. They deliver a fast timing signal which allows an exact determination of the interaction time. A combination of signals in the CIP with signals in the COP and in the forward proportional chambers (forward MWPC) is used to trigger on charged particle trajectories originating from the interaction region. For this purpose the signals in the proportional chambers are combined and filled into the so called z-vertex histogram as indicated in Figure 2.4 from which the trigger decisions are derived. Further details of this procedure are given in [BEC96] and [H1C96].

The forward tracking system covers the polar angle region $5^o < \theta < 25^o$and therefore provides tracking information in the direction of small polar angles. It consists of three identical submodules each containing two drift chambers. The wires in one of the drift chamber are strung parallel to each other (labeled as 'planar' in Figure 2.3), while the wires of the other are strung radial (labeled as 'radial' in Figure 2.3). In both the wires are strung perpendicular to the beam axis. Each module is completed by multi-wire proportional chambers (FPC) which are used for fast trigger decisions and transition radiation detectors which may be used for electron hadron separation.

The spatial resolution of the forward tracking system is $\sigma_{x,y} \leq 200\,\mu$m and the momentum resolution is $\sigma_p/p^2 = 0.03\,\mathrm{GeV}^{-1}$.

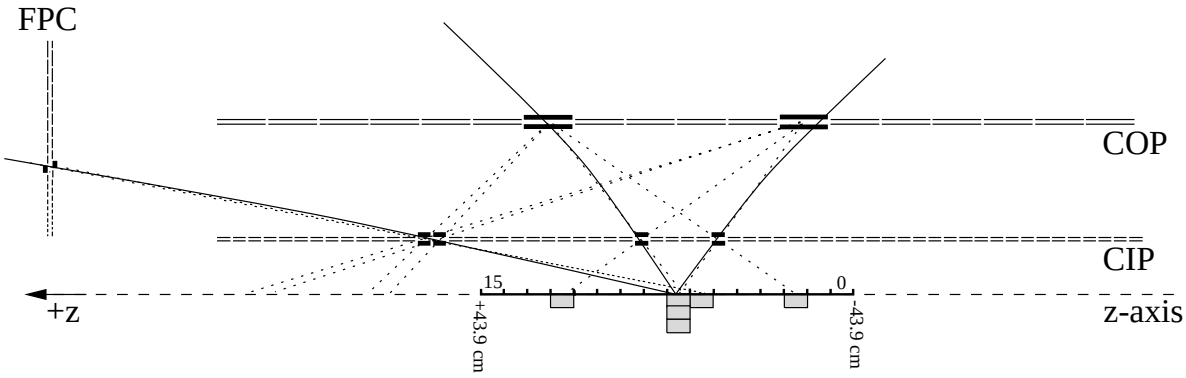

Figure 2.4: Side view of the principle operation of the z-Vertex trigger. Four signals in the CIP, COP or forward MWPC (here denoted as FPC) pointing along a straight line contribute one count to the z-Vertex histogram, which is depicted in the lower part of the figure.

2.4 Backward Drift Chamber

The region of large polar angle $153^o < \theta < 178^o$ is covered by the backward drift chamber (BDC). It is used in this thesis to measure the polar angle of the scattered positron.

The BDC consists of four octagonal double layers with drift chamber cells. The arrangement of the sense wires is shown in Figure 2.5. Each double layer is rotated with respect to the

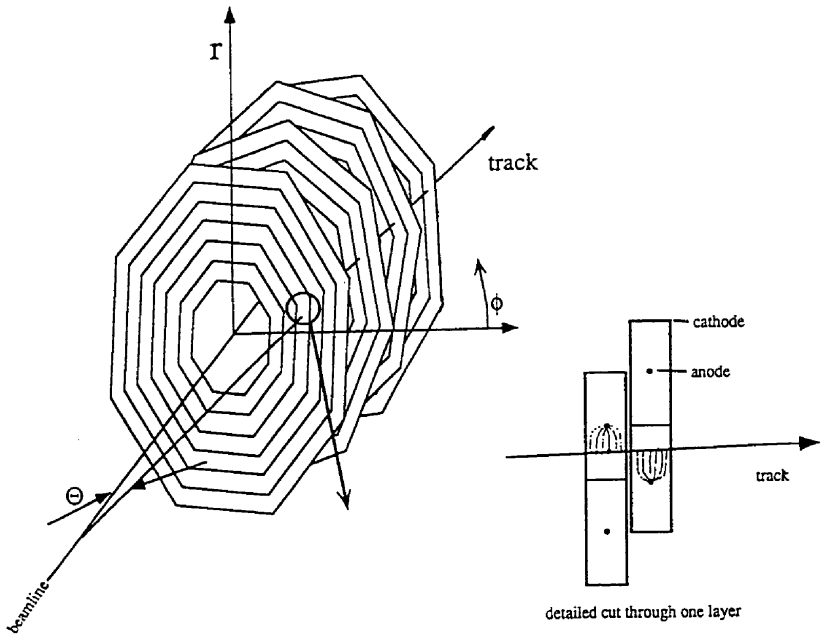

Figure 2.5: Schematic view of the BDC. Shown are the rotated double layers. In lower right part a cut through a double layer is depicted.

previous one in the ϕ direction by an angle of 11.25^o to increase the sensitivity in that direction. The spider's web like structure of the sense wires allows a precise measurement of the scattered

positron in radial direction since the sense wires are perpendicular to the radial vector. The first cells in every second layer are shifted by half a cell width in radial direction to avoid left-right ambiguities. The distance between the sense wires decreases with decreasing distance to the beam axis. This accounts for the increasing rate of background events towards the beam pipe for example from beam-gas interactions.

The resolution on the polar angle of the scattered positron measured in the BDC has been shown to be better than 0.7 mrad [GLA98].

2.5 The H1 Liquid Argon Calorimeter

The H1 liquid argon calorimeter (LAr) covers the polar angle between $4^o < \theta < 153^o$; a side view is shown in Figure 2.6. It consists of eight wheels with inner and outer modules referred to

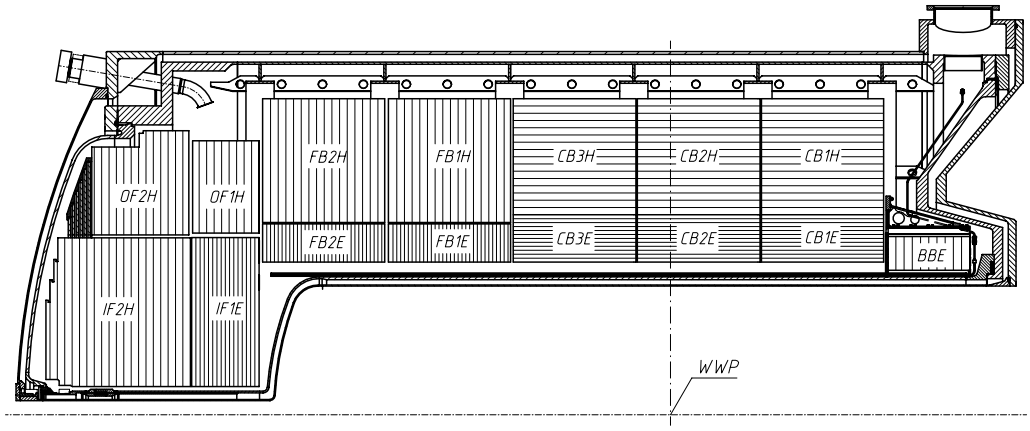

Figure 2.6: Side view on the H1 liquid argon calorimeter.

as the electromagnetic and the hadronic part, respectively. The electromagnetic part is mainly designed to absorb electromagnetic showers. Together with the hadronic part the LAr Calorimeter provides a nearly complete absorption of hadronic showers which is of great importance for the analysis presented here.

The LAr is a sampling calorimeter. As active material liquid argon is used because of its good stability, the homogeneity of the response and the fine granularity which can be achieved with this material. The passive material in the electromagnetic part of the calorimeter is lead while for the hadronic part iron is used. The depth of the electromagnetic part varies between 20 and 30 radiation lengths. The hadronic interaction length varies between 8 λ_I in the forward region and 4.5 λ_I in the central region.

The total calorimeter consists of 45000 cubic cells with typical dimensions of $4 \times 4 \times 4\,\mathrm{cm}^3$ in the electromagnetic part and $10 \times 10 \times 10\,\mathrm{cm}^3$ in the hadronic part. They measure the energy deposited by any high energetic particle initiating a shower when entering the calorimeter. Topological connected cells are grouped to macro objects called cluster. The algorithm used for the clustering is described in detail in [GOR96].

The H1 liquid argon calorimeter is a non-compensating calorimeter. This means that the signal produced by an electron is 25% higher than the signal generated by a hadron of the same energy. However, the fine segmentation of the calorimeter allows the various components of a hadronic shower to be detected such that the difference can be balanced by proper weighting

techniques [WEL90, WEL94, ISS96]. The reweighted hadronic clusters are the main experimental information used to identify jets of particles.

The calibration of the liquid argon calorimeter was done in test beam experiments and is controlled by α and β sources [BAB94] as well as by the analysis of halo muons [NAU98]. Further control of the calibration is obtained by comparing the transverse energy of the scattered positron and of the hadronic final state, which have to be identical according to energy-momentum conservation. From these studies, the absolute calibration of the calorimeter is known to be 4% for hadronic showers and 3% for electromagnetic showers as referred to in this thesis [GAY96]. Most recent developments show that this can be improved to a 1% and 2% precision for electromagnetic and hadronic showers, respectively (see e.g. [HEI99] and Section 4.6).

The energy resolution of the calorimeter has been determined in test beam measurements to

$$\frac{\sigma_E}{E} = \frac{0.11}{\sqrt{E}} \tag{2.1}$$

for electromagnetic showers [H1C94] and

$$\frac{\sigma_E}{E} = \frac{0.5}{\sqrt{E}} \oplus 0.02 \tag{2.2}$$

for hadronic showers where $a \oplus b$ stands for $\sqrt{a^2 + b^2}$.

2.6 The Backward Calorimeter

The backward part of the H1 detector is equipped with a high resolution lead/scintillating fiber spaghetti calorimeter (SpaCal). Technical parameters of the calorimeter are given in Table 2.1. A detailed description of the design of the calorimeter is given in [H1S96-1]. Incident particles develop into a shower of secondary particles in the absorber material which in turn cause the fibers to scintillate. The light is collected by fine mesh photo-tubes [JAN94].

The SpaCal covers the polar angle between $153^o < \theta < 178^o$. In 1995 it replaced the former backward electromagnetic calorimeter BEMC [H1B96, H1C96] providing a larger angular acceptance and an improved energy resolution. The SpaCal is used in this analysis for the measurement of the energy and the scattering angle of the scattered positron as well as for triggering DIS events. Figure 2.7 shows the geometric position of the SpaCal calorimeter in the backward region of the H1 detector.

The SpaCal is split into two sections an electromagnetic part and a hadronic part. The electromagnetic part consists of 1192 cells with a dimension of $4.05 \times 4.05 \times 25\,\mathrm{cm}^3$. The smallest construction units are two cell modules. Sets of eight 2-cell modules are combined to form square 16-cell super-modules which represent the main building blocks of the electromagnetic section. It provides an excellent measurement of the energy and, due to its fine granularity, of the polar angle of the scattered positron. The large angular coverage of the calorimeter is provided by a special insert module which surrounds the beam pipe by adjusting the cell geometry of the 16 cells belonging to the insert module to the cylindrical shape of the beam pipe [DIR95, PFE97]. The hadronic part consists of 136 cells with a dimension of $12 \times 12 \times 25\,\mathrm{cm}^3$. The distinct separation of the complete SpaCal into two different parts allows for a good electron/hadron separation [DIR95, H1S96-2]. A schematic front view of the electromagnetic SpaCal is given in Figure 2.8.

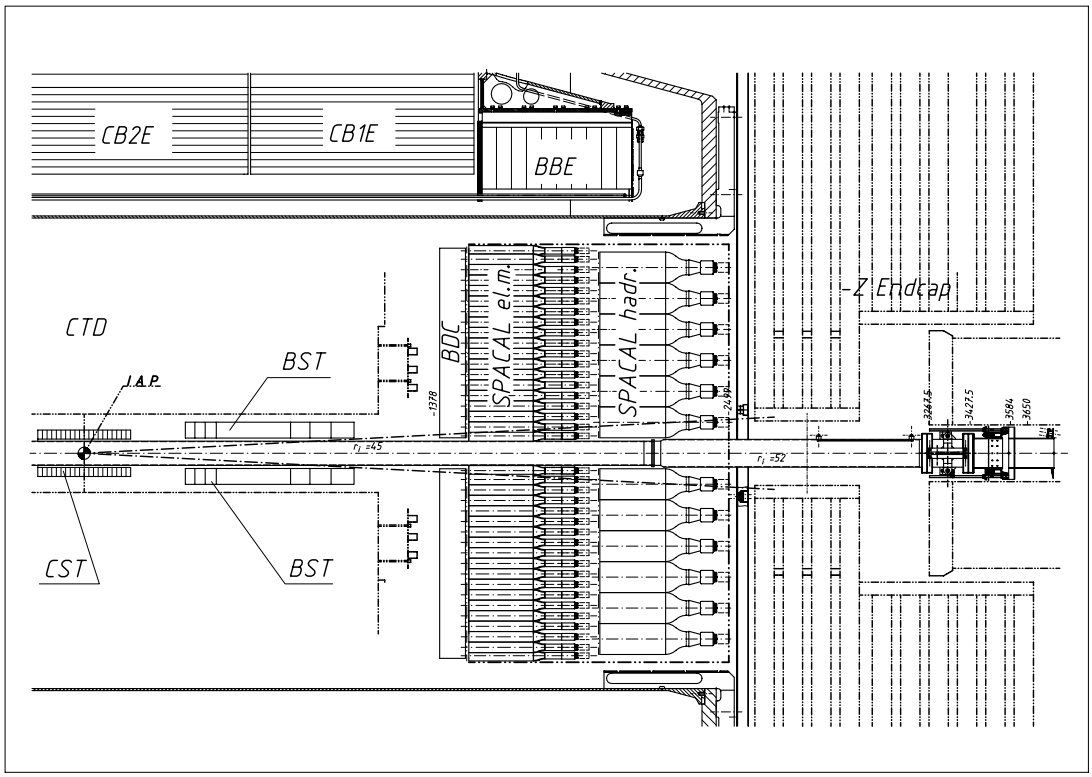

Figure 2.7: Side view of the backward part of the H1 detector which shows the position of the BDC and SpaCal

	electromagnetic	hadronic
Lead/fiber ratio	2.27:1	3.4:1
Fiber Type	BICRON BCF-12	BICRON BCF-12
Fiber diameter	0.5 mm	1.0 mm
Active Length	25 cm	25 cm
Cell Size	$4.05 \times 4.05\,\mathrm{cm}^2$	$12.0 \times 12.0\,\mathrm{cm}^2$
Number of cells	1192	136
Radiation Length	0.90 cm	0.85 cm
Molière Radius	2.55 cm	2.45 cm
Interaction Length	25 cm	25 cm
fine mesh photo-tubes	Hamamatsu R5505	R2490-06
Photo-tube gain at 1 T	$\approx 10^4$	$\approx 2 \times 10^4$

Table 2.1: Technical parameters of the two SpaCal components [TZA97].

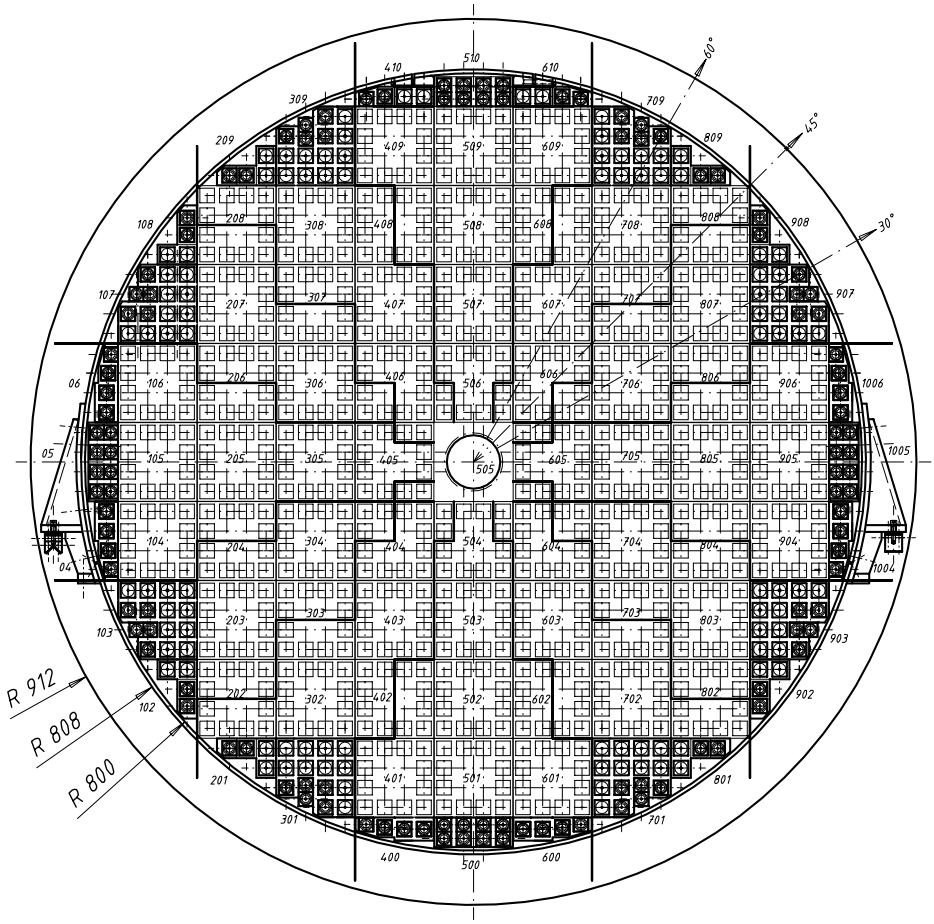

Figure 2.8: Front view of the electromagnetic SpaCal. The wide shaded areas are the super-modules which consists of 4×4 cells. In the very central part the special insert module is visible. The black shaded areas are special cells which fill up the boundary of the calorimeter.

2.6.1 SpaCal Electronics

The calorimeter electronics consists of three different branches. They will be discussed briefly in the following. A detailed description of the SpaCal electronics can be found in [H1S99].

2.6.1.1 The Timing Branch

The Time-of-Flight information, providing timing information at a precision of $\leq$ 1 ns [H1S99, TZA97], allows the separation of good ep from proton induced background at the first trigger level. The time difference between the positron-proton collision and the proton induced background is 10 ns. At the first trigger level a positive coincidence is required between the time signal and an adjustable gate (interaction TOF window). This gate defines the time interval in which good ep events are expected to arrive.

2.6.1.2 The Inclusive Electron Trigger

The inclusive electron trigger (IET) of the SpaCal is specially designed for the measurement of positrons which have been scattered into the backward hemisphere of the H1 detector. For triggering purposes the SpaCal is segmented into groups of 2x2 cells, so called trigger windows, in which the deposited energy is summed (Presums) leading to a slightly worse but sufficient granularity. By this the granularity of the trigger is just four times worse than the granularity of the SpaCal itself. Four adjacent trigger windows are combined to so called trigger towers. The principle of the trigger is illustrated in Figure 2.9. It shows that an energy deposition at point B is registered by trigger tower 3.

The trigger towers overlap in order to avoid inefficiencies at their borders giving rise to the name 'sliding windows'. A positive trigger signal is transmitted to the H1 central trigger logic if an energy deposition registered in one of the trigger towers has passed an adjustable threshold and lies in the interaction TOF window. The energy thresholds relevant for the data taking period considered in this analysis are

- IET$>$0: This corresponds to a threshold of 0.5 GeV.
- IET$>$1: This corresponds to threshold of 2 GeV.
- IET$>$2: This corresponds to threshold of 5.7 GeV.

2.6.1.3 The Energy Branch

In the energy branch the signals are fed into two 12-bit Analog Digital Converter (ADC). In order to cover larger signal range both ADCs work with different effective resolutions such that 2^{14} energy channels are provided. The digitized signals are processed further by digital-signal processors DSPs. The DSP signals are then transferred to the so-called event builder where they are brought into a data format which can be used by the off-line event reconstruction.

2.6.2 Calibration

To provide a homogeneous response of the SpaCal, the relative response of the calorimeter cells is very important. Three methods are used for the calibration [MEY97], [TZA97], [DIR96]:

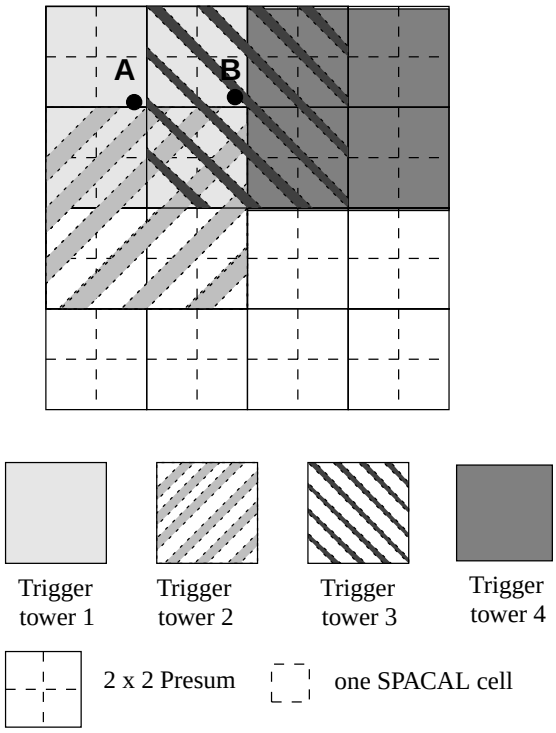

Figure 2.9: Illustration of the principle of the IET trigger. The energy deposition in B may lead to signals four overlapping trigger towers which consist of 16 cells each.

- Calibration using the elastic scattering peak of the ep interaction.
- Calibration using cosmic muons.
- Calibration using muons from the beam halo.

In order to achieve a precise energy measurement it is important to monitor any short term fluctuations and long-term drifts of the SpaCal photo-tubes. This task is performed for the SpaCal by a light-emitting diode (LED) system [JAN96].

The absolute energy calibration can be determined by using the Double Angle Method (see Section 1.1.1). The uncertainty on the electromagnetic energy scale is of the order of 1% [TZA97], [GLA98] and the linearity of the energy response was determined to be 0.5% for energies between 11 and 23 GeV and 2% for energies between 4 and 11 GeV [LEN99]. The electromagnetic SpaCal energy resolution was measured to be [TZA97]:

$$\frac{\sigma_E}{E} = \frac{7.5\%}{\sqrt{E[\mathrm{GeV}]}} \oplus 1\%.$$

2.6.3 Event Reconstruction

The SpaCal event reconstruction consists mainly of two modules:

- SSCALE: At the begin of the reconstruction the energy deposited in the cells of the SpaCal are available in so called DSP units. In the module SSCALE this information is converted to GeV units and calibration factors are applied to the cells. These factors comprise results from the energy calibration as described in Section 2.6.2. At the end of the SSCALE module, well calibrated cell information is ready for further analysis.
- SCLUST: This module uses calibrated cell information as input to create the main output of the SpaCal reconstruction, the clusters. Topologically, connected cells are merged to clusters and their energy and position is calculated. A nice overview over the details of the SpaCal clustering algorithm can be found in [SCH98]. The different methods which can be used for the position reconstruction are discussed in [GAR00] and [POE96]. The clustering algorithms, together with the application of the logarithmic weighting method [AWE92], have been proven to provide a position resolution of 4 mrad [POE96].

2.7 The Time of Flight (TOF) System

The time-of-flight system is used to reject beam induced background. Three scintillators are installed at different positions along the beam pipe. These are the backward TOF (BTOF) at z=-275 cm the forward TOF (FTOF) at z=790 cm and the Plug TOF (PTOF) at z=540 cm. Two scintillator walls at z=-810 cm and z=-650 cm complete the H1 TOF system. All TOF counters together provide a timing resolution of about 1 ns. The TOF system is used in this thesis for triggering purposes. A detailed description of the TOF system and its performance in the data taking period 1997 can be found in [WIS98].

2.8 The Luminosity System

It is vital, for cross section measurements to know, the amount of luminosity available for the analysis. While it can be calculated from the emittance and the currents of the beams, a much

more precise determination is achieved by measuring the rate of events of a well known scattering process. The H1 and ZEUS experiments use the Bethe-Heitler process $ep \rightarrow ep\gamma$ [BET34] by measuring the radiated photon and the electron, simultaneously far away from the interaction point. Theoretically the cross section is known to a precision of 0.5% and the event rate is huge. Therefore, it is well suited to determine the luminosity in an ep collision experiment.

The layout of the H1 luminosity system is shown in Figure 2.10. There are two principal

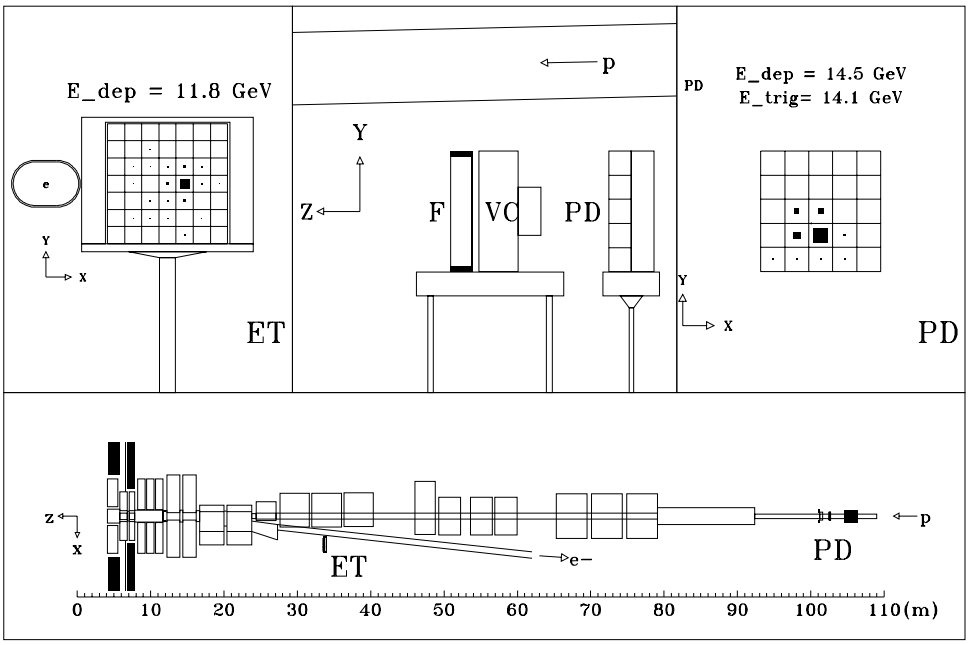

Figure 2.10: Side view of the H1 luminosity system The lower part shows the view on the HERA ring from the interaction point to the photon detector (PD) at -102.9 m. The picture is stretched in x-direction. The upper left part shows the position of the electron tagger (ET) relative to the electron beam pipe. The photon detector is located along the extension of the H1 beam axis under the proton beam pipe. In front of the photon detector a lead filter is installed (F) together with a veto counter (VC).

components available for the measurement of the positron and the photon, respectively. The electron tagger is located close to the beam pipe at $z = -33.4$ m. It detects the positron which, due to its energy loss, is deflected by magnets from the nominal orbit and leaves the beam pipe through an exit window at -27.9 m. It consists of 49 crystals with 22×22 mm^2 each. The crystals themselves consist of 78% TlCl and 22% TlBr. The produced Cherenkov light is detected by photo-tubes.

The photon tagger is located at $z = -102.9$ m. It detects the photons produced in the Bethe-Heitler process and consists of 25 crystals of the same chemical composition as those used in the electron tagger. The dimension of the crystals of the photon detector is 20×20 mm. The photon tagger is protected against synchrotron radiation by a lead shield of 1.5 radiation lengths. Between the lead shield and the photon tagger a water Cherenkov counter is installed. Its purpose is to detect whether the photon has already showered in the lead shield which degrades the energy measurement.

The measurement of the luminosity is of minor importance for this thesis since in the final result only ratios of cross sections are determined. However, for background subtraction, the knowledge of the luminosity is necessary.

2.9 The H1 Trigger System

The trigger system of the H1 experiment is intended to filter interesting events out of the huge amount of background signals. The background rate is typically 10^4 times higher than the rate of 'good' ep interactions. The H1 trigger system consists of five levels, of which only level 1,2,4 and 5 were in operation during 1996/97. At each level, a larger amount of information is available to select and classify interesting events.

2.9.1 Level 1

The components of the H1 detector deliver information which are used to decide, within 2 μs, whether an event is a promising ep event. The central trigger logic combines 192 trigger elements into 128 sub-triggers. If one of these sub-triggers suggests a signature, indicating an interesting ep reaction, the event is accepted, initiating the complete readout of the detector. High rate sub-triggers may be prescaled in order to control the output rate of the L1 trigger.

The most important trigger elements for this analysis are the IET$>$2 threshold of the SpaCal to provide sizable energy deposition in the SpaCal, and the Ray-T0 trigger element which uses signals from the CIP, COP and FPC to trigger on charged particles coming from the interaction region.

2.9.2 Level 2

The second level trigger is based on neural networks and topological requirements. Due to the decision time of 20 μs it allows a more sophisticated selection of events and can optionally be used to refine the L1 trigger decision. It is not explicitly used in the present analysis.

2.9.3 Level 4

If the event has been accepted by the first and second trigger levels it is further analyzed by level four (L4), a software filter based on 32 RISC processors. The event rate which is input to the fourth trigger level varies typically between 30 and 50 Hz. Since the L4 process takes place after the complete detector readout, decisions can be based on the full event information.

The huge event rate which came along with the large amount of luminosity collected in the years 1996/97 made it necessary to down scale physics processes with a high rate. Therefore, since 1997 the software of the fourth level trigger features a Q^2 dependent weighting scheme [LEM97]. The events which are accepted by L4 are written to tape with a rate of approximately $10 - 20$ Hz.

2.9.4 Level 5

The so-called fifth trigger level is identical with the final reconstruction program. Events are completely reconstructed, using the best knowledge of detector calibration and assigned to several event classes. Events not assigned to any of the available event classes are rejected. The remaining data are further compressed and written to data summary tapes (DST) which are the starting point of physics analyzes.

2.10 Simulation

The measured cross sections are influenced by the detector resolution. The measurement has to be corrected for effects of the detector. The complicated structure of the hadronic final state together with the complex experimental apparatus makes such a correction very difficult. For the correction of the data, the following procedure is followed:

- Event generators produce complete deep-inelastic scattering events and provide four vectors of the final state objects. This level of the simulation chain is called the hadron level.
- The four vectors and the particle ID of these objects are fed into the full H1 detector simulation. H1SIM is based on the detector simulation package GEANT and provides the modeling of the full detector response for the various types of particles.
- The simulated events are subject to the same reconstruction chain as the measured data. This part of the simulation chain is called the detector level.
- The simulated spectra are then compared to the measured spectra and, in case of agreement, can be used to correct for detector effects.

Chapter 3

Event Selection

In order to measure the dijet rate R_2, a sample of DIS events has to be selected which serves as the basis of the jet analysis performed. The dijet data will form a subsample of these events.

3.1 Selection of Runs

A run is defined as a period of measurement with equal experimental conditions. In general the analysis comprises data collected in the runs 158007-171156 in the year 1996 and 180076 -201519 in the year 1997. Not all of these runs fulfill the quality criteria to be included the final analysis. For this it is required that the following components of the H1 detector have been fully operational for at least 95% of the time during a run.

- The H1 liquid argon calorimeter to measure the particles of the hadronic final state.
- The backward calorimeter SpaCal to measure the scattered positron and to detect particles of the hadronic final state not contained in the Liquid Argon Calorimeter.
- The backward drift chamber BDC to measure the scattering angle of the scattered positron.
- The central tracking system (CJC1/2, CIP, COP, CIZ, COZ), which is needed to trigger on interesting DIS events, to reconstruct an event vertex and to support the measurement of the hadronic final state.
- The luminosity system to assure the luminosity measurement.

The selected runs have been checked further and some were rejected if they had additional problems [CAR99]. Those runs which have been rejected in this final step of the run selection procedure are listed in Table 3.1 together with the problem enforcing the rejection. The remaining integrated luminosity used for this analysis is 21.9 pb^{-1} in contrast to 2 pb^{-1} used for a preceding analysis of R_2 based on H1 data collected in 1994 [H1C98].

3.2 Fiducial cuts

Experimental constraints made it necessary to split the sensitive region of the SpaCal into two parts. A cell close to the beam pipe with unnaturally high rate presumably caused by synchrotron radiation forced a division into a central and an outer SpaCal IET (see Section 2.6.1.2) region. Since the chosen subtrigger is based on signals from the outer part this results in an insensitivity to signals inside a fiducial volume which is given by

$$-16.2 < x_{spac} < 8.1\,\mathrm{cm} \text{ and } -8.1 < y_{spac} < 16.2\,\mathrm{cm},$$

Run range	Reason for rejection
1 9 9 6	
168472-168488	SpaCal HV problems
169186-169222	SpaCal triggers rejected on L4
170864-170866	Test of L4 scheme for 1997
1 9 9 7	
183675-183686	COP off
184462-184469	No MWPC in readout
186020-186021	COP off and BDC tests
191550-191579	No MWPC in readout
191585-191596	Problems with z_{vtx}-trigger
192081-192088	Corrupted data logging
192094-192115	Corrupted data logging
192815-192964	Problems with central trigger hardware
193128-193235	HERA/H1 timing problems
193479-193524	HERA/H1 timing problems
194643-194644	No MWPC in readout
195681-195686	No MWPC in readout
198345-198376	Unstable tracker performance
201322-201342	Test of upgraded L4 scheme
201373-201383	Test of upgraded L4 scheme

Table 3.1: List of run ranges which have been excluded from the run selection .

where the variables x_{spac}, y_{spac} denote the position of the boundaries of that region in the SpaCal volume. In order to avoid problems at the border between the two regions, caused by the leakage of electromagnetic showers into the insensitive region, a save cut has been applied in the analysis to exclude the above fiducial volume. Two additional fiducial cuts became necessary due to hardware problems of two SpaCal super modules resulting in the exclusion of the corresponding ones for part of the data taking. The applied fiducial cuts are illustrated in Figure 3.1 and summarized as follows:

- Fiducial cuts in 1996 and 1997: $-17.5 < x_{spac} < 10.2\,\text{cm}$ and $-10.2 < y_{spac} < 17.5\,\text{cm}$. This cut excludes the central SpaCal IET region.
- Fiducial cut in 1996: $8.1 < x_{spac} < 24.5\,\text{cm}$ and $-8.1 < y_{spac} < 8.1\,\text{cm}$: This cut excludes a SpaCal super module with a faulty high voltage supply during 1996.
- Fiducial cut in 1997: $22.3 < x_{spac} < 40.5\,\text{cm}$ and $-40.5 < y_{spac} < -22.3\,\text{cm}$: This cut excludes a SpaCal super module with hardware problems during 1997.

If a DIS event has been identified inside the defined fiducial volumes of the SpaCal it is rejected.

3.3 Selection of Neutral Current DIS events

This section is devoted to discuss observables which allow the separation of DIS events from background. A large source of background to DIS events in the analyzed phase space between

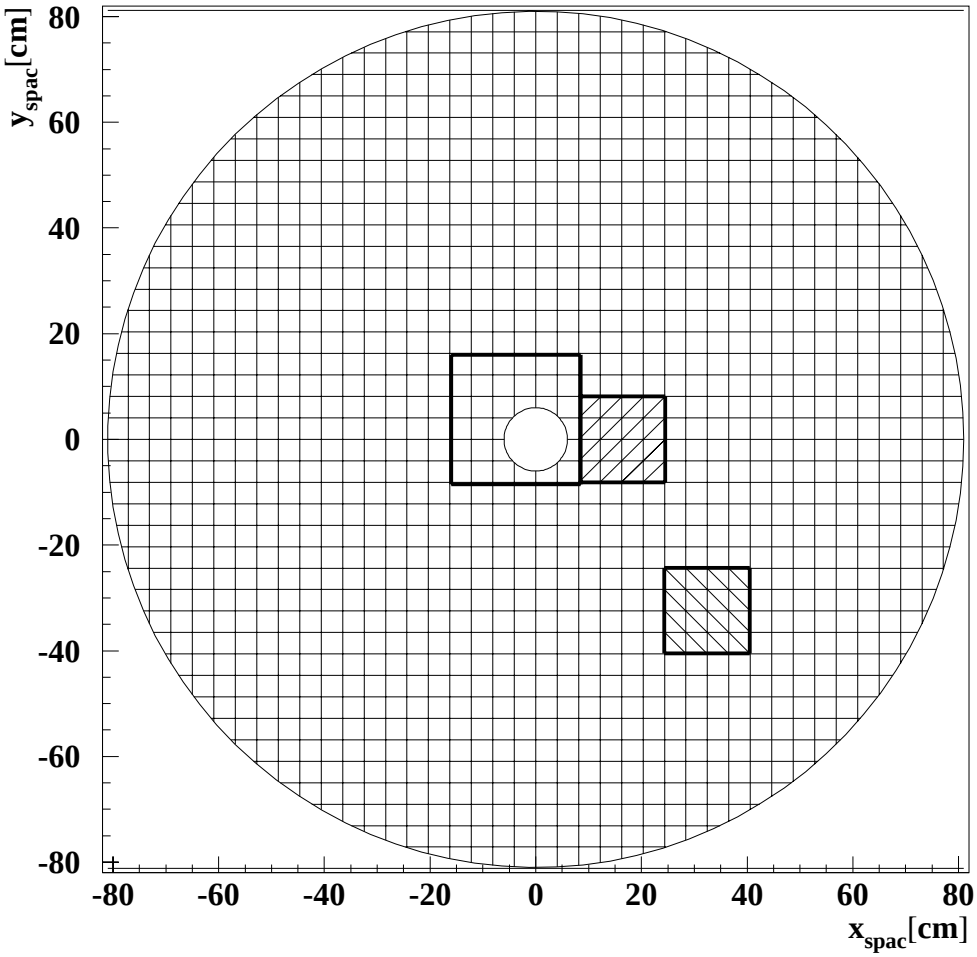

Figure 3.1: Schematic front view of the SpaCal. The thick lines surround the regions excluded from the analysis. The region without hatch lines represents the regions covered by the central IET Card (see text). The left hatched area represents the region covered by a problematic super module in 1996 and the right hatched area represents the region covered by a problematic super module in 1997 .

$5 < Q^2 < 100\,\mathrm{GeV}^2$ are events from photoproduction. In this case a quasi real photon with $Q^2 \approx 0$, is exchanged between the positron and the quark such that the positron is scattered by a small angle and escapes through the beam pipe and charge particle of the hadronic final state may mimic an positron signal. In 10% of the cases the positron is measured by the electron tagger, a fact which is used for systematic studies of this background.

Another type of background are the so called beam gas or beam wall events in which beam particles interact with gas molecules in the vacuum or collide with the wall of the beam pipes.

3.3.1 Suppression of beam gas and beam wall background

The beams are adjusted with the magnet optics of the HERA collider such that there will be a positron proton collision at a well defined point inside the H1 detector. The proton bunches have a Gaussian profile in longitudinal direction with a width of around 11 cm leading to the fact that the collisions are distributed around the nominal interaction point. The event vertices produced by beam gas or beam wall events are equally distributed along the z-axis of the H1 coordinate frame and can be suppressed if a restricted z-interval is allowed for the position of the vertex. Furthermore events are suppressed where the positron reacts with so called satellite bunches which come along with the main proton bunches at a distance of about 1.20 m. These collisions produce a vertex at large positive or large negative values along the z-axis.

The existence of an event vertex is mandatory for the determination of the kinematics of DIS events. Figure 3.2 shows the distribution of the z position of the event vertex for the data taking periods 1996 and 1997 within the chosen cut boundary of $|z_{vtx}| < 35$ cm.

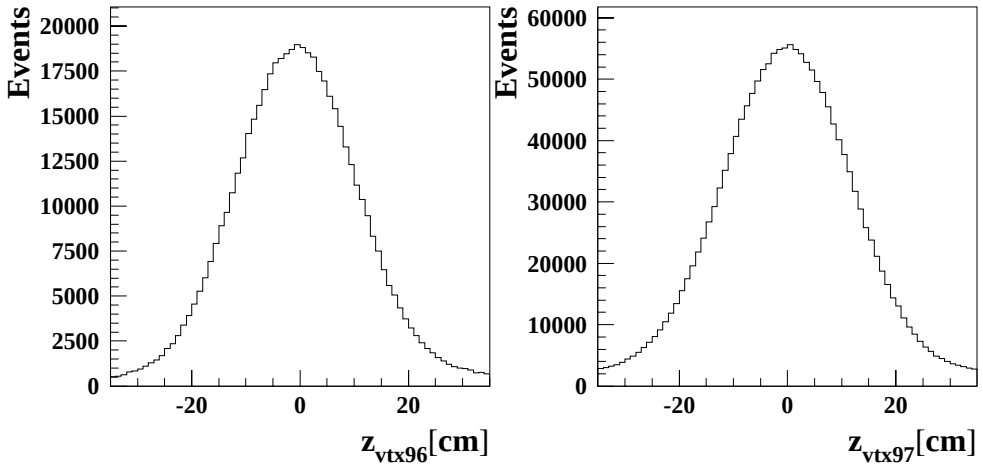

Figure 3.2: Distribution of the z vertex position as measured in the data taking period 1996 (left) and 1997 (right).

3.3.2 Suppression of γp events and QED radiation

The sum of the energies of the incoming positron (E_e) and proton (E_p) subtracted by the sum of their longitudinal momentum $p_{z,e}$ and $p_{z,p}$, respectively, is equal to twice the beam energy of

the incoming positron, i.e. equal to 55 GeV. Due to energy conservation, this holds if the same quantity is built from all final state particles including the scattered positron. This leads to the following equation:

$$(E_e + E_p) - (p_{z,e} + p_{z,p}) = 2E_e = (E - p_z) = (E_e^{'} + \sum E_i) - (p_z^{'} - \sum p_{z,i}), \qquad (3.1)$$

where $E_e^{'}$ and $p_z^{'}$ are the energy and longitudinal momentum of the scattered positron and the sum runs over all particles i of the hadronic final state.

All particles which are measured in the liquid argon calorimeter, the SpaCal and the trackers of the H1 detector contribute to the right hand side of Equation 3.1. In case of γp events the positron leaves no signal in any of these detectors and its contribution to the right hand side of Equation 3.1 is zero. Therefore, this sum will deviate strongly from the expected value of 55 GeV.

Figure 3.3 shows the $(E - p_z)$ distribution for DIS events compared to events which were unambiguously identified as γp background due to the detection of the positron in the electron tagger. The distribution of the DIS events show a clear maximum at the expected value of 55 GeV while the tagged events peak significantly below. Thus, a further separation of DIS events from γp events can be obtained by requiring

$$35\,\text{GeV} < (E - p_z) < 70\,\text{GeV}. \qquad (3.2)$$

In addition this cut suppresses effects from QED radiation where the incoming positron radiates a highly energetic photon which leaves the detector through the beam pipe.

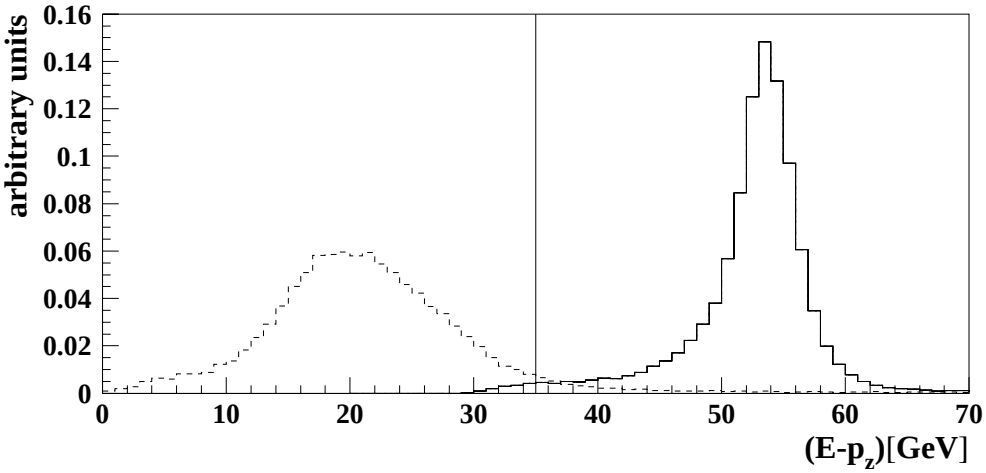

Figure 3.3: The $(E - p_z)$ spectrum for measured DIS events (full line) compared to events in which the scattered positron has been measured in the electron tagger (dashed line). The lower cut on $(E - p_z)$ is indicated by the line perpendicular to the y axis.

3.4 Identification of the Scattered Positron

Two devices, SpaCal and BDC, in the backward part of the H1 detector are used identify the scattered positron. In case of γp-events, charged hadrons of the hadronic final state may fake a positron signal and contaminate the sample of DIS events. The lower the minimal energy required for the scattered positron, the higher the background will be. The cuts presented and discussed in this section help to minimize the contamination. First, the general selection criteria are presented. The main cuts for background suppression will be discussed later on in this section. The general selection criteria are:

- Cut on cluster energy : The most energetic cluster reconstructed in the electromagnetic SpaCal defines the positron candidate. The event is accepted if

  $$E_e^{'} > 9\,\mathrm{GeV}$$

  which effectively suppresses remaining background from γp events, as indicated in Figure 3.4.

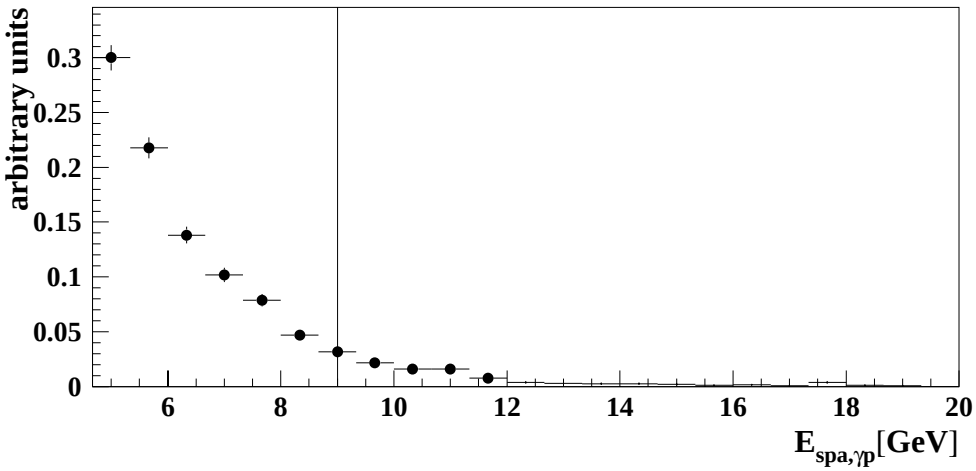

Figure 3.4: The energy spectrum of the hottest cluster in the SpaCal ($E_{spa,\gamma p}$) for measured events in which the scattered positron was tagged in the electron tagger and which could therefore be identified as γp background.

- Cut on polar angle of scattered positron: The polar angle θ_e of the scattered positron is measured by the backward drift chamber, BDC, using the algorithm BDCLEV which takes the cluster position as an input to determine the associated track [KEL98]. The requirement

  $$156^o < \theta_e < 175^o$$

  ensures that the electromagnetic shower produced by a positron is fully contained in the SpaCal volume and provides that the positron induces a signal in the acceptance region of the BDC which is mounted directly in front of the SpaCal such that their acceptance regions coincide.

- Cut on y_e : The inelasticity variable is calculated by using the positron energy E_e' and its scattering angle θ_e according to Equation 1.10. The cut

$$y_e > 0.1$$

provides (1) a substantial track activity in the central and forward jet chambers which leads to a high probability for the existence of a reconstructed event vertex and (2) the restriction of the measurement to a kinematic region where the determination of the event kinematics by the scattered positron alone reveals relatively small systematic errors (see Section 1.1.1).

3.4.1 The Cut on the Cluster Radius

An important estimator to distinguish between signals from scattered positrons and signals produced by hadrons is the transverse size of a cluster in the SpaCal. The observable which describes the transverse size is the cluster radius, R_{cl}. It is defined as

$$R_{cl} = \frac{\sum_i E_i \sqrt{(x_{cl} - x_i)^2 + (y_{cl} - y_i)^2}}{E_{cl}}. \tag{3.3}$$

The sum runs over all cells at position x_i, y_i with energy deposition E_i which to a cluster with x_{cl}, y_{cl} and E_{cl} representing the x, y position of a cluster and its energy, respectively.

Positrons are expected to produce a much more compact cluster than hadrons because of the different interactions of both particle types in the absorber material. Hence it can be expected that positrons lead to a smaller value of the cluster radius than hadrons.

To study the difference between positron and hadronic signals two event samples have been selected: one in which the signal in the SpaCal is, with a high probability, produced by the scattered positron, and one in which the signals in the SpaCal is expected to be produced by hadrons. This is realized by the following two criteria:

- The "positron sample" is selected by requiring the most energetic cluster to be above 16 GeV. Above this cut the signal is produced in 99% of the cases by positrons [WEG91] (see also Section 4.2.1).

- For the "hadron sample" it is required that the scattered positron has been identified in the electron tagger of the H1 experiment ensuring only hadronic activity in the SpaCal. Bethe-Heitler events, i.e. $ep \to ep\gamma$, are suppressed by requiring the energy measured in the photon tagger (see Section 2.8) to be zero.

Figure 3.5 compares the distributions of the cluster radius of the most energetic cluster in the electromagnetic SpaCal to the cluster radius of the most energetic cluster produced by hadrons. The figure demonstrates that the cluster radius distribution for positrons peaks at 2.5 cm with a tail to 3.2 cm compatible with the Molière Radius of the SpaCal of approximately 2.55 cm. For hadrons the tail extends far above the value of 3.5 cm such that a requirement of $R_{cl} < 3.5$ cm rejects approximately 20% of the γp-background while keeping the high selection efficiency for positrons. This is demonstrated in the right part of Figure 3.5 which shows an selection efficiency of 99%.

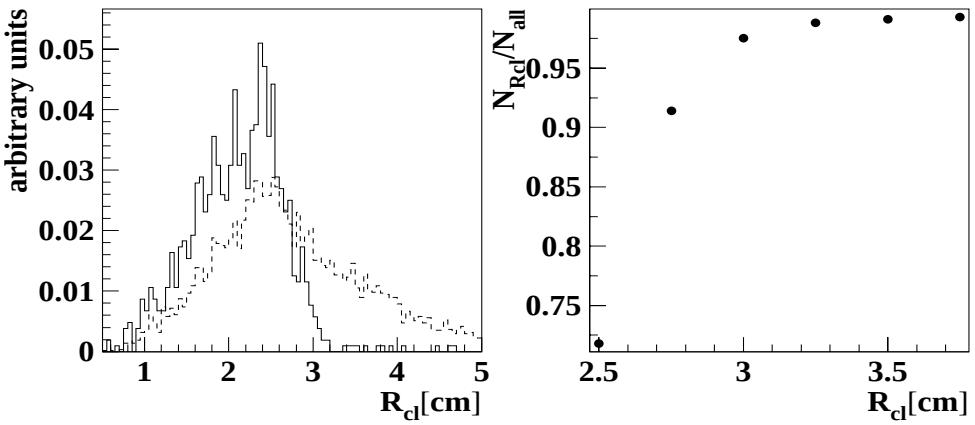

Figure 3.5: Left: Cluster radius distributions for positrons (full line) and hadrons (dashed line). Right: Efficiency of the positron selection as a function on the cut on the cluster radius.

3.4.2 The Cut on the Energy in the Hadronic SpaCal

Hadron induced signals are further reduced by means of the energy deposition in the hadronic part of the SpaCal. The electromagnetic SpaCal is constructed such that positrons with an energy up to 30 GeV can be absorbed completely with leakage losses smaller than 0.1% [H1S96-1]. The maximum energy of a scattered positron hitting the SpaCal after an ep collision is given by the elastic peak of 27.5 GeV. Therefore it is expected that showers produced by scattered positrons do not leave any substantial signal in the hadronic SpaCal. For hadrons, however, the average distance between two nuclear interactions is much larger than that for electromagnetic interactions. Therefore, the longitudinal size of a hadronic shower is expected to be much larger. As a consequence, hadron induced showers should reach into the hadronic SpaCal and lead to a sizable energy deposition.

The quantity E_{had} will serve as a measure of whether a cluster in the electromagnetic SpaCal has been produced by a positron or a hadron. The procedure to measure E_{had} will be described in the following and is illustrated in Figure 3.6. The line connecting the cluster position in the electromagnetic SpaCal and the interaction vertex defines a particle trajectory which is extrapolated to the medium z-position of the hadronic SpaCal. A ring with radius r is defined around this extrapolated point. The energy deposited in the cells inside this ring is summed up and defines the quantity E_{had}.

The value for r and the maximum E_{had} requirement have to be carefully chosen in order to (a) guarantee coverage of the full transverse size of any hadronic energy deposition and to (b) avoid the rejection of true positron signals due to hadronic final state particles near by.

By setting r to 15 cm and E_{had}^{cut} to 0.5 GeV it is ensured that always more than one cell of the hadronic SpaCal must contribute to E_{had}. This excludes situations where, due to the transverse extension of the hadronic showers, only a minor part of the hadronic energy deposition is seen. Figure 3.7a shows the fraction of positron candidates which deposit less than E_{had}^{cut} in the hadronic SpaCal; above E_{had}^{cut} more than 99.5% of the positron candidates are kept. Figure 3.7b shows the fraction of hadrons which on one hand deposit 4 GeV in the electromagnetic SpaCal and on the other hand deposit less than E_{had}^{cut} in the hadronic SpaCal. It can be deduced that approximately 70% of the hadrons deposit less than 0.5 GeV in the hadronic section which means on the other

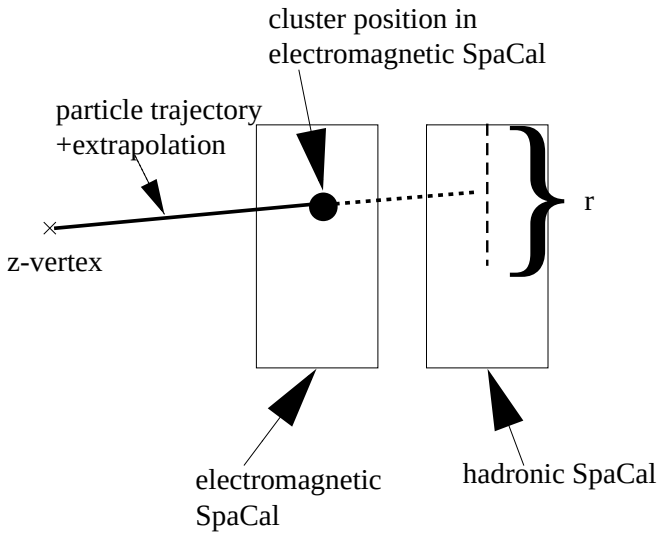

Figure 3.6: Extrapolation of a trajectory defined by the z-vertex and the cluster position in the electromagnetic SpaCal into the hadronic SpaCal.

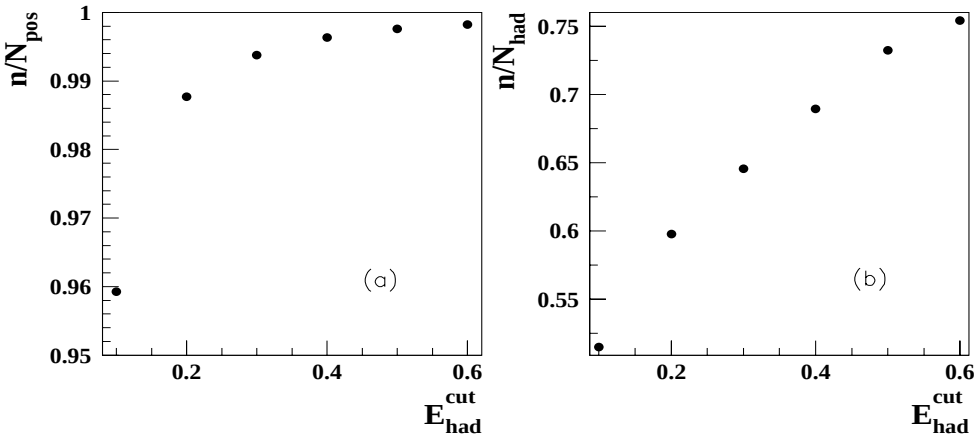

Figure 3.7: (a)Fraction of positron candidates which deposit less than E_{had}^{cut} in the hadronic SpaCal. (b) Fraction of hadrons which deposit less than E_{had}^{cut} in the hadronic SpaCal.

hand that 30% of the hadrons are rejected by this cut.

3.5 Trigger Studies

The intended measurement of the dijet rate at moderate Q^2 requires that a trigger be optimized to measure DIS events. DIS events in the analyzed kinematic range are mainly determined by a scattered positron in the SpaCal and an event vertex. The subtrigger (S_1) is therefore composed of the following elements:

$$S_1 = (\text{IET} > 2) \wedge (\text{Ray} - T0) \wedge (\text{zVtx}_{mul} < 7) \wedge (\text{TOF})$$

- IET > 2: An energy deposition of at least 5.7 GeV in one trigger tower of the outer SpaCal.
- Ray-T0 : Signals in either the central or forward proportional chambers.
- $\text{zVtx}_{\text{mul}} < 7$: The number of entries in the z-Vertex histogram (see Section 2.3) is coded in three bits and is a measure for the activity in the track chambers. If all three bits are set the z-Vertex histogram contains more than 200 entries. Beam gas and beam wall background lead to a large track multiplicity. Hence, this trigger element is used to reject beam gas background.
- TOF: Signals in the forward TOF counters have to fall into the time window which is characteristic for DIS events [WIS98].

This trigger was used until run 198027 when an additional L2 condition was imposed, cutting out the inner region SpaCal to reduce the trigger rate. Afterwards 75% of events with $Q^2 < 30\,\text{GeV}$ which fulfill the selection criteria given in Sections 3.4 and 3.3 were rejected and the subtrigger S_0 had to be used. This subtrigger has the IET > 2 and the TOF conditions in common with the subtrigger S_1 without the Ray-T0 and the $\text{zVtx}_{\text{mul}} < 7$ requirements. Approximately 5.5 pb^{-1} of data were collected with this trigger setup. The Ray-T0 condition is required off-line to ensure track activity and a large probability for the existence of an event vertex. Concerning the $\text{zVtx}_{\text{mul}} < 7$, it has been found that it does not reject interesting DIS events in the investigated phase space (see also Section 4.2.2).

At this point, it must be mentioned that in many runs, the subtrigger S_0 was operated with a prescale factor which varies between 2 and 5. This is compensated by simply applying the prescale factor as a weight to these events.

3.5.1 Trigger Efficiencies Studies

The main components of the chosen trigger setup are the trigger elements IET>2 and the Ray-T0 condition which ensure the existence of an energy deposition in the SpaCal and activity in the track chambers needed for the reconstruction of an event vertex. Therefore, their efficiency is studied in detail in the following sections. For the inefficiencies of the TOF trigger elements it is referred to [WIS98] where a $(99.2 \pm 0.4)\%$ efficiency is derived. An approximately 100% efficiency is also found for the $\text{zVtx}_{\text{mul}} < 7$ condition as mentioned above and investigated in detail in Section 4.2.2.

The trigger efficiency determines the probability that an event which fulfills the selection criteria is registered by a given trigger. It is defined as

$$\epsilon = \frac{\#\text{events which fulfill selection criteria and have been registered by the trigger}}{\#\text{events which fulfill selection criteria}}. \qquad (3.4)$$

Obviously, the event sample used to study the trigger efficiency must have been collected by a trigger which is independent from the trigger under study. The efficiency can then be parameterized as function of a suitable test variable x_T according the following equation [KUR93]:

$$\epsilon(x_T) = \frac{p_3}{e^{\frac{p_1 - x_T}{p_2}} + 1}. \tag{3.5}$$

where P_1 denotes the threshold at which the efficiency reaches 50% and P_2 parameterizes the threshold behavior. At $P_1 \pm 3 \cdot P_2$ the efficiency reaches a value of 95% and 5%, respectively. Finally, P_3 defines the maximal available efficiency.

For the trigger element IET>2, the variable used for the parameterization is naturally given by the energy $E_e^{'}$ of the scattered positron. P_1 of this trigger element has been identified earlier (see Section 2.6.1.2) and is, with $P_1 = 5.7\,\text{GeV}$, well below the 9 GeV energy cut described in Section 3.4. Figure 3.8 shows the trigger efficiency of IET>2 as a function of the energy of the hottest cluster in the SpaCal generally identified as $E_e^{'}$. Since the threshold of the IET>2 trigger element is well below the energy cut of 9 GeV the exponential defined in Equation 3.5 turns into a constant leaving only the parameter P_3 different from zero. The averaged efficiencies are shown separately for the data taking periods 1996 and 1997. Figure 3.8 demonstrates that the

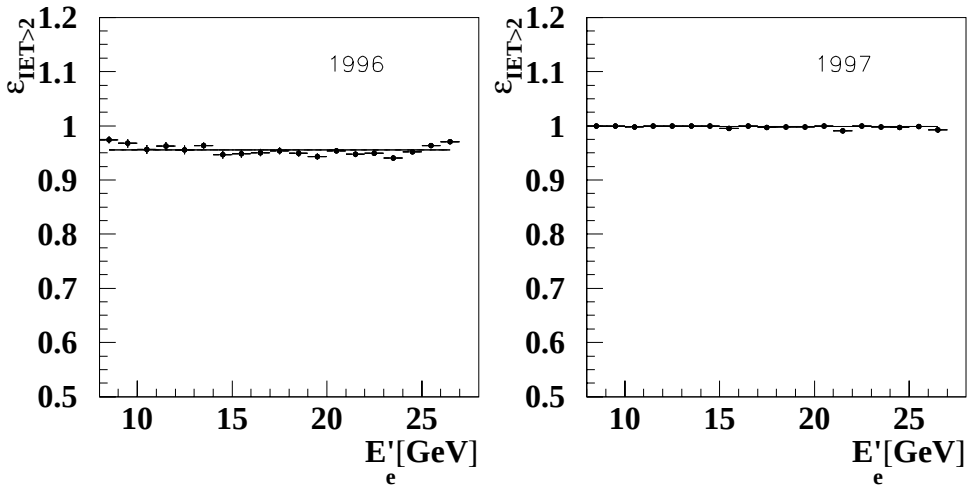

Figure 3.8: Efficiency of the trigger element IET>2 averaged over the data taking periods 1996 and 1997. The fit applied to the curve is explained in the text.

SpaCal-IET trigger provides a trigger efficiency of more than 96% in the chosen energy range. The deviation from 100% can be explained by data taking periods where the *ep* interaction time was shifted by 2 ns with respect to its nominal value. Therefore 'good' *ep* events have been measured outside the SpaCal-TOF window and have been rejected by the H1 trigger system as background. The data are subdivided into different periods to study the development of the trigger efficiency in more detail. The obtained trigger efficiencies for the different run ranges are summarized in Table 3.2.

They are generally close to 100% and only for the run range 165000-169000 they do fall below the 90% margin due to wrong beam timing. This leads to the averaged efficiency of 96% for 1996 data taking period. For the 1997 data taking period some run ranges with large inefficiencies

Run range	IET>2	Ray-T0		
1 9 9 6				
	p3	p1	p2	p3
158007-158570	0.99 ± 0.01	1.59 ± 0.20	3.62 ± 0.12	1.00 ± 0.01
158571-159061	0.99 ± 0.01	1.84 ± 0.22	3.70 ± 0.14	0.99 ± 0.01
159062-159340	1.00 ± 0.01	2.06 ± 0.18	3.25 ± 0.11	1.00 ± 0.01
159341-159877	1.00 ± 0.01	1.99 ± 0.20	3.37 ± 0.12	1.00 ± 0.01
159878-160598	0.99 ± 0.01	1.62 ± 0.19	3.39 ± 0.12	1.00 ± 0.01
160599-160856	0.99 ± 0.01	1.41 ± 0.22	3.49 ± 0.12	0.99 ± 0.01
160857-162472	1.00 ± 0.01	1.80 ± 0.20	3.37 ± 0.12	1.00 ± 0.01
162743-163317	1.00 ± 0.01	1.75 ± 0.17	3.31 ± 0.10	1.00 ± 0.01
163318-163862	1.00 ± 0.01	1.58 ± 0.23	3.29 ± 0.14	1.00 ± 0.01
163863-164623	0.99 ± 0.01	1.75 ± 0.21	3.52 ± 0.13	1.00 ± 0.01
164624-165345	0.99 ± 0.01	1.71 ± 0.22	3.48 ± 0.14	1.00 ± 0.01
165346-166608	0.80 ± 0.01	3.18 ± 0.25	4.88 ± 0.17	0.99 ± 0.01
166609-167821	0.89 ± 0.01	1.17 ± 0.28	3.82 ± 0.16	1.00 ± 0.01
167822-169048	0.87 ± 0.01	1.24 ± 0.22	3.53 ± 0.12	1.00 ± 0.01
169049-169851	0.97 ± 0.01	1.76 ± 0.18	3.34 ± 0.11	1.00 ± 0.01
168852-170361	1.00 ± 0.01	1.52 ± 0.32	4.57 ± 0.23	0.98 ± 0.02
170362-170800	1.00 ± 0.01	2.08 ± 0.23	3.22 ± 0.15	0.99 ± 0.01
170801-171156	0.99 ± 0.03	2.11 ± 0.28	3.20 ± 0.20	1.00 ± 0.01
1 9 9 7				
182017-187308	0.99 ± 0.01	0.92 ± 0.10	3.47 ± 0.06	0.99 ± 0.01
187309-192525	0.99 ± 0.01	1.36 ± 0.08	3.17 ± 0.10	0.99 ± 0.01
192526-196369	0.98 ± 0.01	1.57 ± 0.07	3.27 ± 0.04	1.00 ± 0.01
196370-198857	1.00 ± 0.01	1.65 ± 0.06	3.08 ± 0.03	1.00 ± 0.01
198857-200445	1.00 ± 0.01	1.31 ± 0.07	3.14 ± 0.04	1.00 ± 0.01
200446-201519	1.00 ± 0.01	0.93 ± 0.07	3.62 ± 0.04	0.99 ± 0.01

Table 3.2: Values of the parameters used to parameterize the IET>2 and Ray-T0 efficiency. The interpretation of the parameters $P_1 ... P_3$ is given in the text .

have been excluded as can be seen in Table 3.1. Here the averaged efficiency is $(99.7 \pm 0.1)\%$. The trigger element is hence perfectly suited to select DIS events as analyzed in this thesis.

The Ray-T0 trigger element is closely related to the existence of an event vertex. Drift chamber cells of the central and forward proportional chambers of the H1 detector are grouped to patterns to build this trigger signal [H1C96]. If all cells of such a pattern carry signal in a time t_0 after an ep interaction the trigger element delivers a positive signal and the event is classified as a potentially 'good' ep event. Since measured tracks in the proportional chambers are tightly coupled to the existence of a reconstructed event vertex, this trigger element allows the first trigger level to separate events with a vertex from those without one.

Figure 3.9 shows the efficiency of the Ray-T0 trigger signal as a function of the sum of the number of central and forward tracks $(N_{ctr} + N_{ftr})$. The trigger efficiency is again parameterized

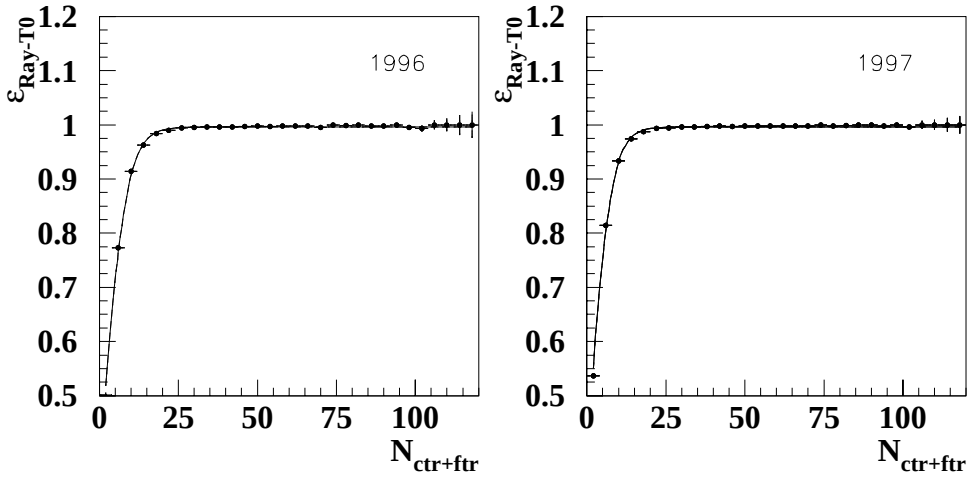

Figure 3.9: Efficiency of the trigger element Ray-T0 averaged over the data taking periods 1996 and 1997. The fit applied to the curve is explained in the text.

using Equation 3.5. For events with more than 20 tracks the trigger element is nearly one hundred percent efficient. DIS events which lead to a small number of tracks are those in which the inelasticity variable y takes very small values. In that case, only a little energy is transferred to the proton leading to small hadronic activity in the final state of the ep interaction. Therefore only very few tracks are produced by charged particles of the hadronic final state. This is demonstrated in Figure 3.10 where the track multiplicity is plotted as a function of y_e. Apart from the lower track multiplicity at low y_e the figure shows that above the cut value $y_e > 0.1$ the averaged number of tracks is in the range where the Ray-T0 element provides an efficiency of $(99.6 \pm 0.1)\%$. This result justifies the y_e-cut applied in this analysis.

3.5.2 Higher Trigger Levels

The huge amount of data collected in 1996 and 1997 made it necessary to reduce the data volume written to tape. Several selection criteria have therefore been implemented on the trigger levels 4 and 5. Due to these criteria, recorded and selected events may obtain weights. In several reports on the regular H1 data quality meetings it was shown that these selection criteria acted properly

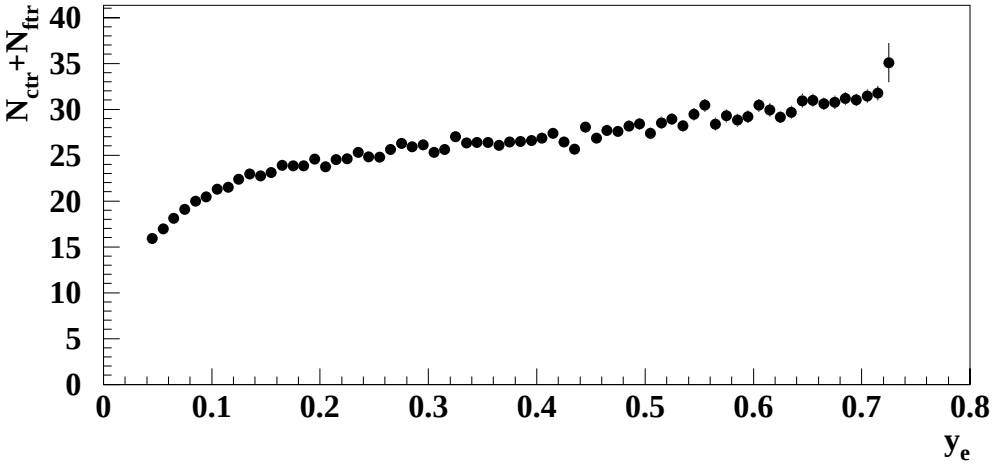

Figure 3.10: Number of central and forward tracks ($N_{ctr} + N_{ftr}$) as a function of the inelasticity variable y_e.

on the data and that the weights applied to the events selected by this analysis are always one [OLS97].

3.6 Selection of 2-Jet Events

If an event has passed the selection criteria given in Sections 3.4 and 3.3 and fulfills the criteria imposed on the jet selection as defined in this section it will be called a dijet event here after. The selection criteria for dijet events are as follows :

- Cut on the transverse energy E_t^* of a jet: As mentioned in Section 1.6.2 the jet identification is performed in the hadronic center-of-mass frame. It is required that at least two jets are identified with $E_t^* > 5\,\text{GeV}$. This cut restricts the analysis to a phase space region which is accessible by perturbative QCD calculations and, as will be shown below, guarantees a good jet resolution provided by the experimental devices.

- Cut on the jet position: At least two of the identified jets must be situated in a pseudo rapidity region in the laboratory η_{lab} of $-1 < \eta_{lab} < 2.5$. This ensures that the jets are well measured within the acceptance of the LAr calorimeter, which is the main carrier of the hadronic final state in the H1 detector.

In order to impose these requirements, jets have to be defined. However, the hadrons emerging after hadronization from the hard scattering process cannot be measured directly by the experimental devices but appear as tracks and clusters in the detector. The basic experimental question is now how to treat the signals produced by the hadronic final state in order to identify jets and thus to make the measurement a reliable image of the underlying physics processes. In this analysis the method of the **Combined Objects** is adapted [SPI97] and its merits are investigated.

The H1 liquid argon calorimeter is designed to provide an almost complete absorption of high energetic hadrons such that most of the energy flow of the hadronic final state can be measured correctly. Therefore it is rather attractive to calculate four vectors from these clusters and to use these objects as an input to the jet algorithm. However, there are two caveats to this naive approach:

1. Low momentum particles: Charged particles with low momentum might be bent away by the magnetic field such that they cannot reach the calorimeter and thus cannot contribute to the jet finding.

2. The capacitance of the cells in the liquid argon calorimeter produce noise which makes it difficult to measure low energy particles. Typical noise values for cells are 30 MeV to 50 MeV [BOR98]. The fact that a cluster is built up of many calorimeter cells enhances the difficulty to measure low energy particles. Hence, a noise cut is applied on a cell by cell basis to reject those which carry an energy below a threshold of three or four standard deviations above the average noise level.

Considering the fact that the transverse momentum spectrum of jets is steeply falling, it is clear that the jet identification is rather sensitive to the low energy particles of the hadronic final state. This is, in particular, true for jets with a polar angle of $\pi/2$ in the laboratory frame when the transverse energy is equal to the total energy of the jet.

In order to compensate for the energy losses described one uses the tracking information. To avoid double counting, the maximum momentum assigned to a track is limited by an upper bound P_{limit}. The bound should be of the order of a few hundred MeV such that the energy assigned to the tracks just compensates the expected energy losses.

Figure 3.11 shows the ratio between the number of dijet events on detector level, N_{det}, and on hadron level, N_{had}, as a function of η_{lab} for events, simulated with DJANGO/CDM, for three values of P_{limit}. Choosing $P_{limit} = 0$ means that the hadronic final state consists only of objects

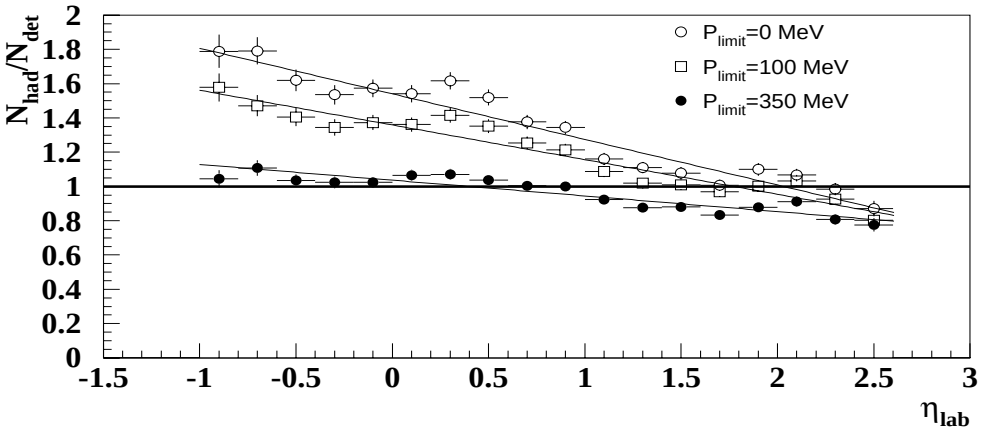

Figure 3.11: Ratio of number of jets detected on hadron level (N_{had}) and the corresponding number of jets detected on detector level (N_{det}) as a function of the jet position in the laboratory frame η_{lab} for different values of P_{limit} .

measured in the calorimeter. The figure demonstrates that the agreement between the number

of jets on hadron level and on detector level is strongly dependent on η_{lab}. This dependency is reduced by the addition of tracks to the objects of the hadronic final state which enter the jet algorithm. Choosing $P_{limit} = 350\,\text{MeV}$ nearly eliminates the dependency on η_{lab}.

This defines the objects which will be passed to the jet algorithm:

- The four vectors of all clusters measured in the calorimeters of the H1 detector, except the forward plug.
- The four vectors of all tracks measured in the central and forward track chambers of the H1 detector. If their momentum is below 350 MeV they are included as such. If however their momentum larger than 350 MeV their momentum is limited to the upper bound of 350 MeV.

The sample of objects consisting of the calorimeter clusters and the (rescaled) tracks which are passed to the jet algorithm will be called combined objects, hereafter.

Recent developments in the H1 collaboration have established another way of treating the objects of the hadronic final state [MAR98]. The benefits that this analysis may gain from the new approach will be discussed in Section 4.6.

Chapter 4

Measurement of the Differential Dijet Rate

In this chapter, the observable R_2 (see Chapter 1) will be determined on the basis of events selected as specified in the previous chapter. First the division of the kinematic plane is presented. Then the data are compared to the predictions of Monte Carlo simulations to prepare the correction of the data for background, detector effects and effects from QED radiations. At the end of this chapter the fully corrected dijet rate will be presented, single and double differentially, as a function of x_B and Q^2.

4.1 Division of the analyzed Phase Space

The measurement presented in this thesis is a detailed investigation of dijet production in the low to medium x_B and Q^2 regime. To study the dependence of the observable R_2 on x_B and Q^2 the phase space has to be subdivided. For the single differential measurement a choice of the bins has been adopted to match a similar analysis using data recorded with the H1 detector in the year 1994 [SPI97, H1C98]. No attempt is made to revise this binning. The bins are listed in Table 4.1.

Bins in Q^2	Bins in x_B
$5 < Q^2 < 11\,\mathrm{GeV}^2$	$10^{-4} < x_B < 2.5\,10^{-4}$
$11 < Q^2 < 15\,\mathrm{GeV}^2$	$2.5 \cdot 10^{-4} < x_B < 5 \cdot 10^{-4}$
$15 < Q^2 < 20\,\mathrm{GeV}^2$	$5 \cdot 10^{-4} < x_B < 10^{-3}$
$20 < Q^2 < 30\,\mathrm{GeV}^2$	$10^{-3} < x_B < 2.5 \cdot 10^{-3}$
$30 < Q^2 < 50\,\mathrm{GeV}^2$	$2.5 \cdot 10^{-3} < x_B < 5 \cdot 10^{-3}$
$50 < Q^2 < 100\,\mathrm{GeV}^2$	$5 \cdot 10^{-3} < x_B < 10^{-2}$

Table 4.1: Division of the phase space for the single differential measurement of R_2.

For the double differential measurement, the bins given in Table 4.1 have been further subdivided according to the following guidelines:

1. The bin size is adapted to the available resolution for the investigated variables.
2. The selected dijet events are equally distributed amongst the chosen bins.

The final binning of the phase space for the double differential measurement of R_2 is presented in Figure 4.1; the exact values are given in Table 4.2.

4.2 Quality of the DIS Selection

After the final selection as described in Chapter 3 approximately 1,3 million DIS events and 50,000 dijet events remain for the analysis. In order to compare the inclusive spectra to pre-

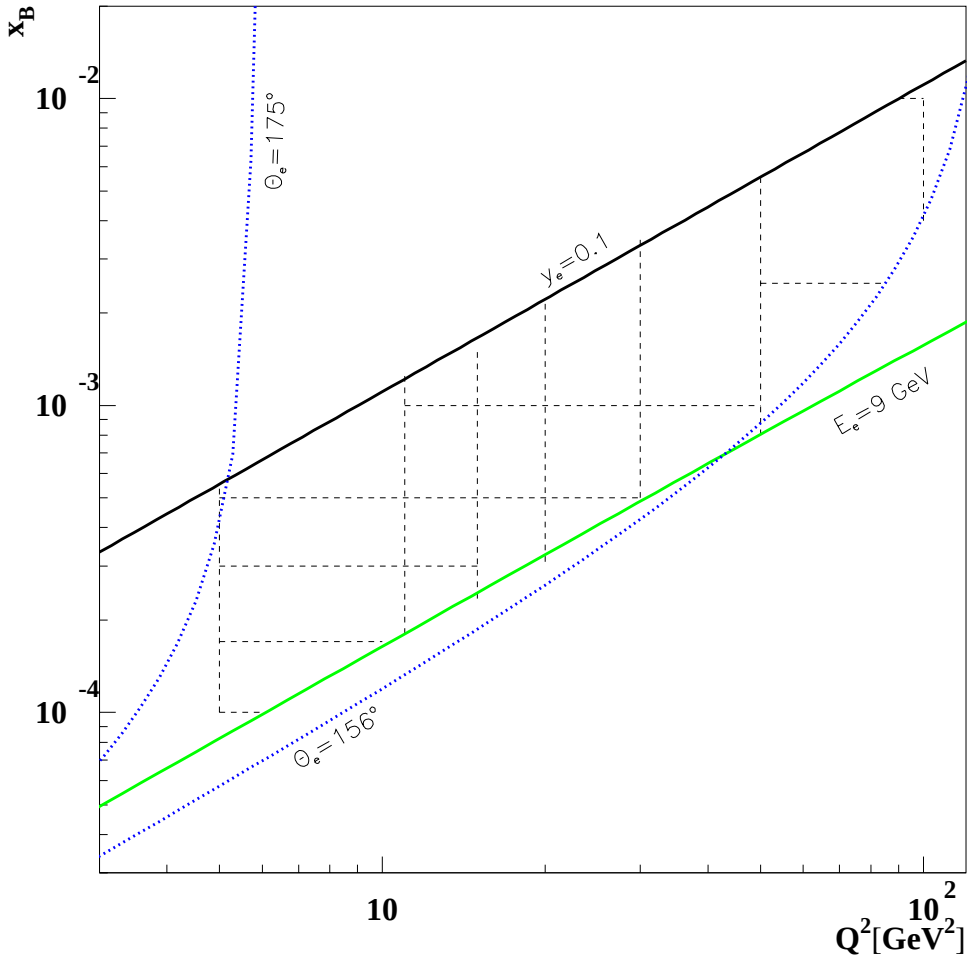

Figure 4.1: Division of the kinematic plane for the double differential measurement of R_2.

Bins in Q^2/GeV^2	Subdivision in bins of x_B	$< Q^2 >$ /GeV^2	$< x_B >$
$5 < Q^2 < 11$	$10^{-4} < x_B < 1.7 \cdot 10^{-4}$	6	$1.4 \cdot 10^{-4}$
	$1.7 \cdot 10^{-4} < x_B < 3 \cdot 10^{-4}$	7	$2.3 \cdot 10^{-4}$
	$3 \cdot 10^{-4} < x_B < 5 \cdot 10^{-4}$	7	$3.9 \cdot 10^{-4}$
	$5 \cdot 10^{-4} < x_B < 1.3 \cdot 10^{-3}$	8	$6.8 \cdot 10^{-4}$
$11 < Q^2 < 15$	$1.7 \cdot 10^{-4} < x_B < 3 \cdot 10^{-4}$	13	$2.5 \cdot 10^{-4}$
	$3 \cdot 10^{-4} < x_B < 5 \cdot 10^{-4}$	13	$3.9 \cdot 10^{-4}$
	$5 \cdot 10^{-4} < x_B < 10^{-3}$	13	$7.2 \cdot 10^{-4}$
	$10^{-3} < x_B < 1.8 \cdot 10^{-3}$	13	$1.2 \cdot 10^{-4}$
$15 < Q^2 < 20$	$2.4 \cdot 10^{-4} < x_B < 5 \cdot 10^{-4}$	17	$3.8 \cdot 10^{-4}$
	$5 \cdot 10^{-4} < x_B < 10^{-3}$	17	$7.2 \cdot 10^{-4}$
	$10^{-3} < x_B < 2.2 \cdot 10^{-3}$	17	$1.4 \cdot 10^{-3}$
$20 < Q^2 < 30$	$3 \cdot 10^{-4} < x_B < 5 \cdot 10^{-4}$	23	$4.3 \cdot 10^{-4}$
	$5 \cdot 10^{-4} < x_B < 10^{-3}$	25	$7.2 \cdot 10^{-4}$
	$10^{-3} < x_B < 3.3 \cdot 10^{-3}$	25	$1.7 \cdot 10^{-3}$
$30 < Q^2 < 50$	$5 \cdot 10^{-4} < x_B < 10^{-3}$	37	$7.8 \cdot 10^{-4}$
	$10^{-3} < x_B < 5.5 \cdot 10^{-3}$	39	$2.2 \cdot 10^{-3}$
$50 < Q^2 < 100$	$8 \cdot 10^{-4} < x_B < 2.5 \cdot 10^{-3}$	60	$1.8 \cdot 10^{-3}$
	$2.5 \cdot 10^{-3} < x_B < 10^{-2}$	71	$4.7 \cdot 10^{-3}$

Table 4.2: Kinematic intervals and average $Q^2$and x_B for the double differential measurement of R_2.

dictions of Monte Carlo simulations events generated with RAPGAP and DJANGO/CDM are used for which the detector response has been simulated. The luminosity of the simulated events correspond to twice that of the data . The background originating from γp events is estimated with the generator PHOJET [ENG95].

Before the comparison between data and Monte Carlo events is performed, both sets of events have, however, to be corrected for various effects. The data have been corrected for the inefficiencies and prescaling of the chosen subtrigger. The $z-$axis of the positron and the proton beam do not coincide which each other resulting in a beam tilt of typically 1.6 mrad which has to be taken into account in the reconstruction of the polar and azimuthal angles of the scattered positron. For the Monte Carlo simulation four effects have been considered. (1) The vertex position varied during the data taking period but the Monte Carlo events are simulated with an average value for the 1996 and 1997 data taking periods. Hence, the simulated vertex has to be reweighted by the vertex positions measured in the data. The procedure of the reweighting is described in [GLA98]. (2) For the initial generation of the Monte Carlo events which are later subject to the detector simulation structure functions have been used for the incoming proton. The GRV 94 HO [GLU95] parameterizations was used for the 1996 Monte Carlo generation while the CTEQ4M [CTE97] was used for the 1997 Monte Carlo generation. The generated events have been reweighted according to the structure function measured in [GLA98] leading to a correction of the order of 5%. (3) The spectra of the polar and of the azimuthal angle of the scattered positron have been corrected for beam tilt effects included in the simulation of the data of the year 1997 . (4) The cluster radii calculated after detector simulation have been multiplied by a factor 1.05 to obtain a reasonable agreement between the data and the simulation.

4.2.1 Control Distributions of inclusive variables

In Figure 4.2 the observables used to select DIS events are compared to simulated DIS and γp events. It demonstrates a reasonable agreement between the measured data and the Monte Carlo simulations. This also holds for the energy spectrum, the polar angle spectrum and the azimuthal angle spectrum shown in Figure 4.3. The deviation of the azimuthal angle spectrum from the expected flat shape can be explained by the fiducial cuts which are applied in the event selection according to Section 3.2. The shape is approximately described by the simulation. The shaded part of the plots reflects the background originating from γp interactions.

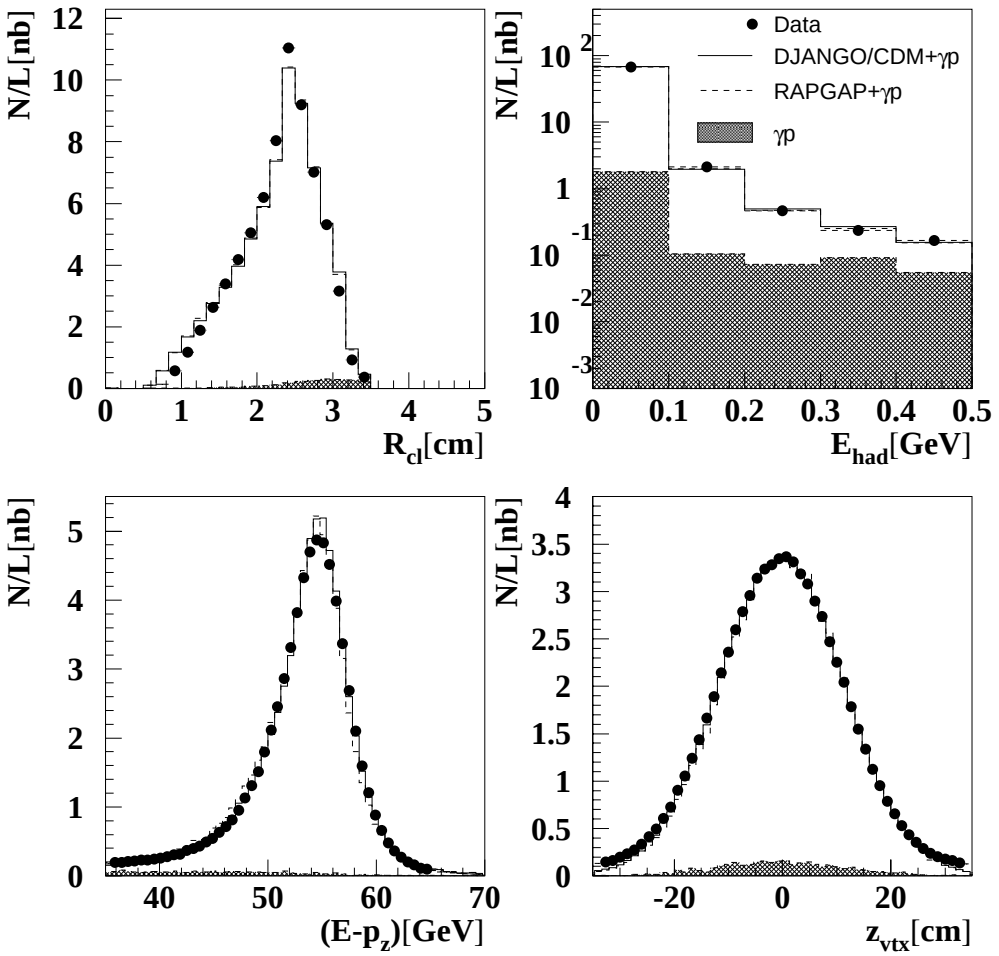

Figure 4.2: Comparison of the measured observables which are used to select DIS events as measured in the data (points) compared to the predictions of DJANGO/CDM (full line) and RAPGAP (dashed line) to which the amount of photoproduction background (γp, shaded part) was added. Upper Left: Cluster radius distribution, Upper right: Energy distribution in the hadronic SpaCal, Lower left: $(E - p_z)$ distribution, Lower Right: z-vertex distribution. The spectra are normalized to the integrated luminosity of the data sets.

A more detailed investigation of the inclusive variables is done in Figures 4.4 through 4.7 where the kinematics of the scattered positron is shown for different parts of the phase space for

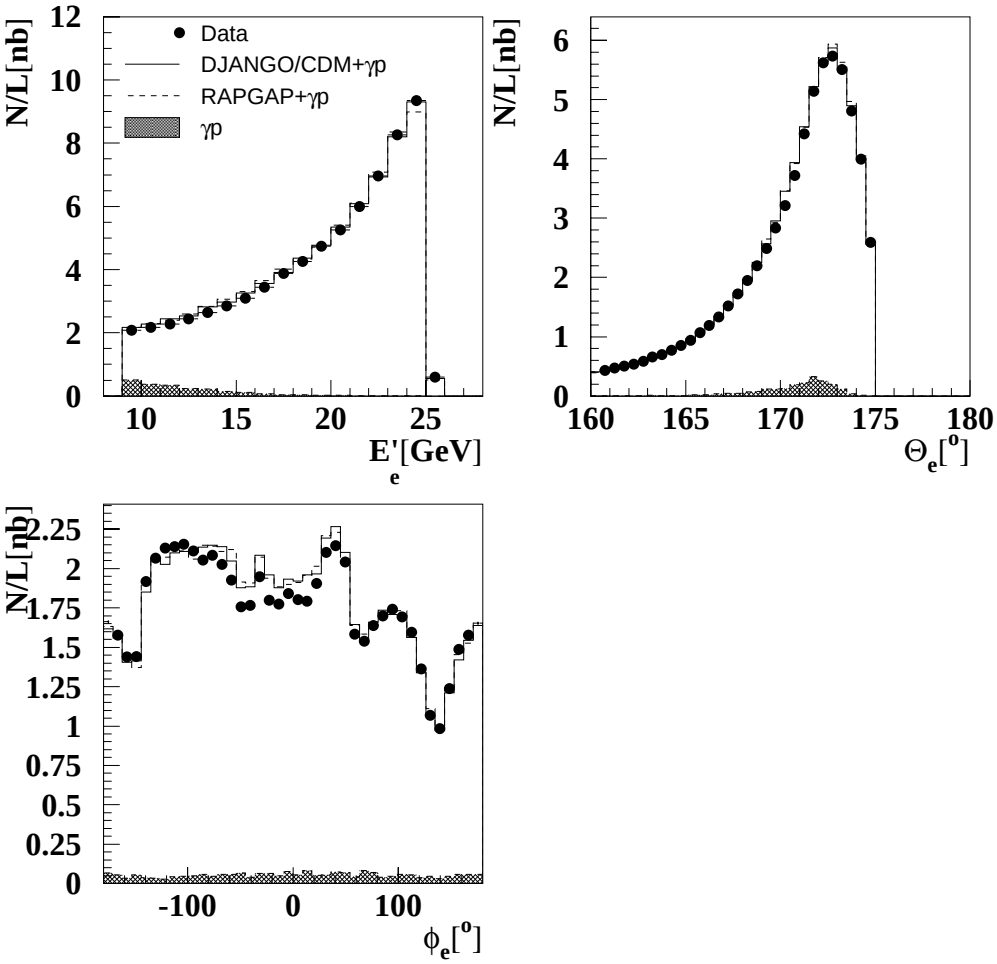

Figure 4.3: Inclusive spectra of measured DIS events (points) in terms of the energy of the scattered positron $E_e^{'}$, its polar angle θ_e and its azimuthal angle ϕ_e compared to the predictions of DJANGO/CDM (full line) and RAPGAP (dashed line) to which the amount of photoproduction background (γp, shaded part) was added. The spectra are normalized to the integrated luminosity of the data sets.

the inclusive DIS sample and the restricted dijet sample. The measured energy distributions and the polar angle spectra are compared to the predictions of Monte Carlo simulations. For the

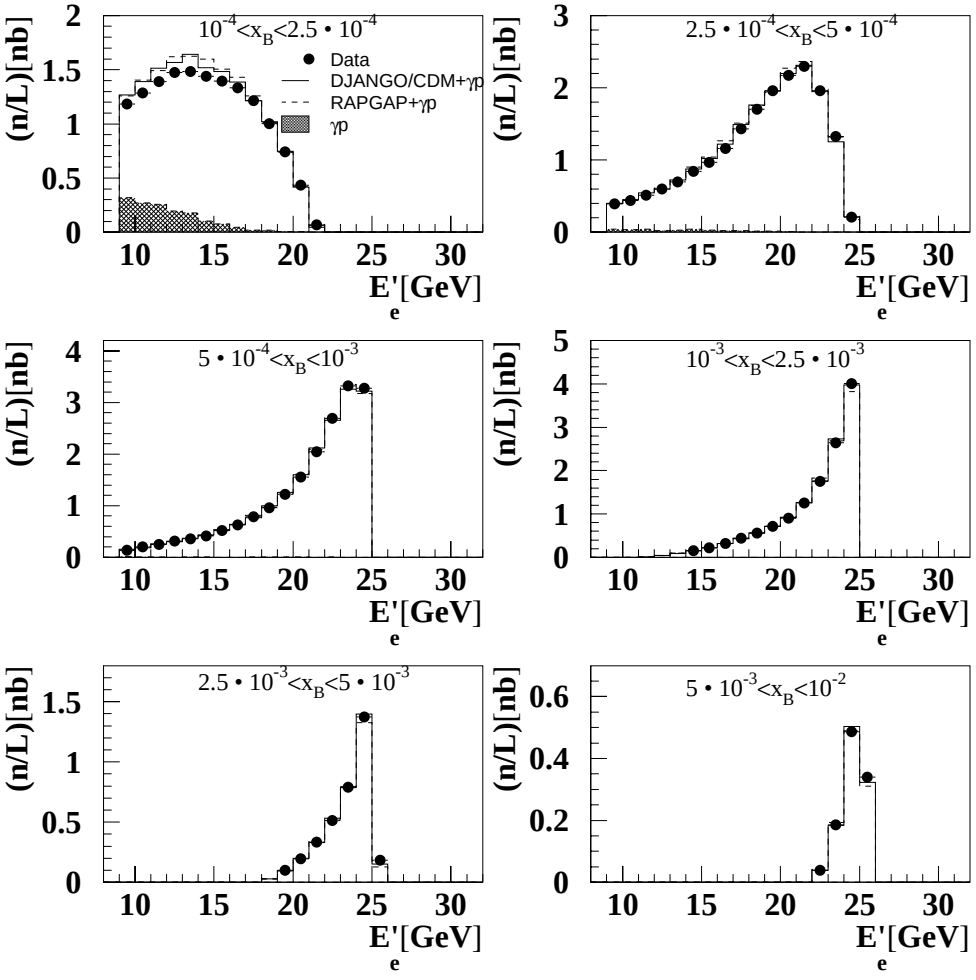

Figure 4.4: Energy spectra of the scattered positron for measured DIS events (bullets) for six ranges in x_B compared to the predictions of DJANGO/CDM (full line) and RAPGAP (dashed) to which the amount of photoproduction background (γp, shaded part) simulated with PHOJET is added. The spectra are normalized to the integrated luminosity of the data sets.

investigation of the Q^2 bins the polar angle is chosen since the calculation of Q^2 is very sensitive to the accurate measurement of the scattering angle of the positron. The energy of the scattered positron is chosen for the investigation of the x_B bins because in this case more sensitivity is expected from the energy of the scattered positron.

In general, the simulated spectra describe the measured spectra in the entire analyzed phase space. However, at low x_B the sum of simulated $\gamma p + DIS$ events overshoot the data. Since the spectra are well reproduced in regions which are not contaminated by γp background, concentrated at low x_B, it is concluded that the estimated amount of γp background is too large. This will be taken into account in the systematic error of the final result.

The studies prove that the simulated DIS events give a reliable description of the measure-

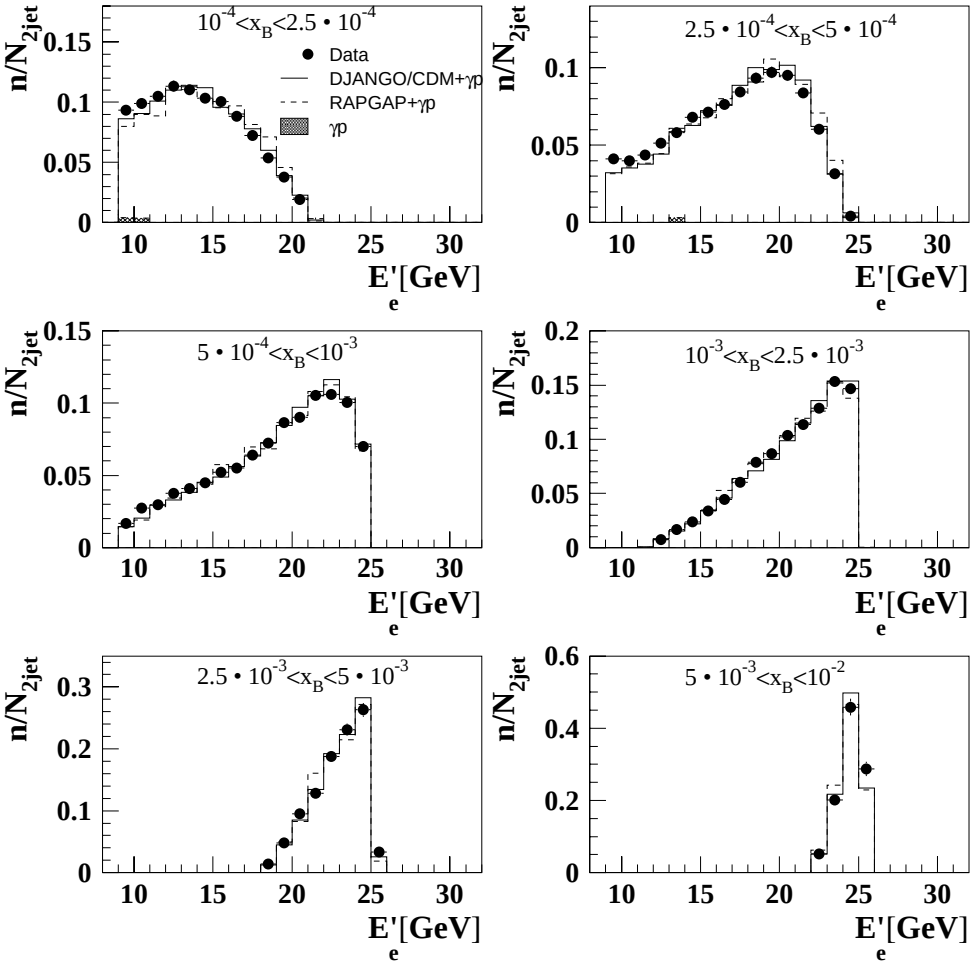

Figure 4.5: Energy spectra of the scattered positron in measured dijet events (bullets) for six ranges in x_B compared to the predictions of DJANGO/CDM (full line) and RAPGAP (dashed) to which the amount of photoproduction background (γp, shaded part) simulated with PHOJET is added.

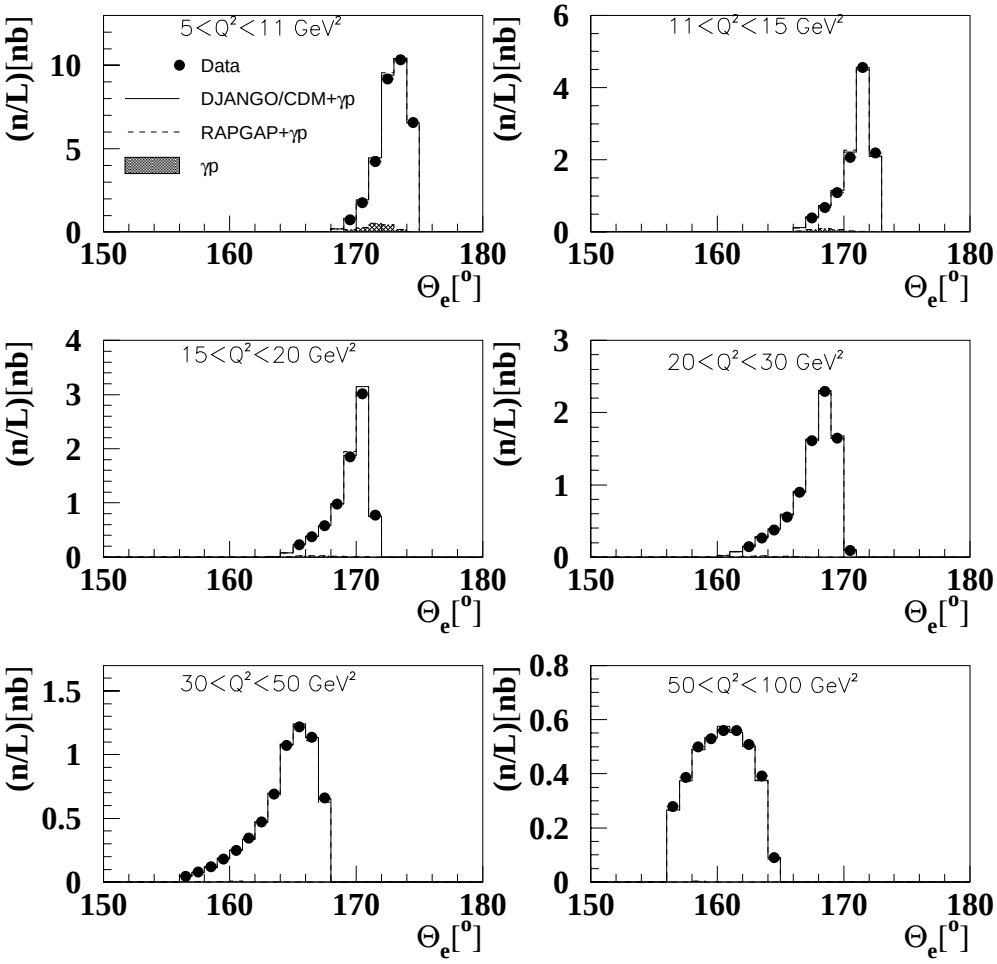

Figure 4.6: Polar angle spectra of the scattered positron for measured DIS events (bullets) for six ranges in Q^2 compared to the predictions of DJANGO/CDM (full line) and RAPGAP (dashed) to which the amount of photoproduction background (γp, shaded part) simulated with PHOJET is added. The spectra are normalized to the Luminosity of the data sets.

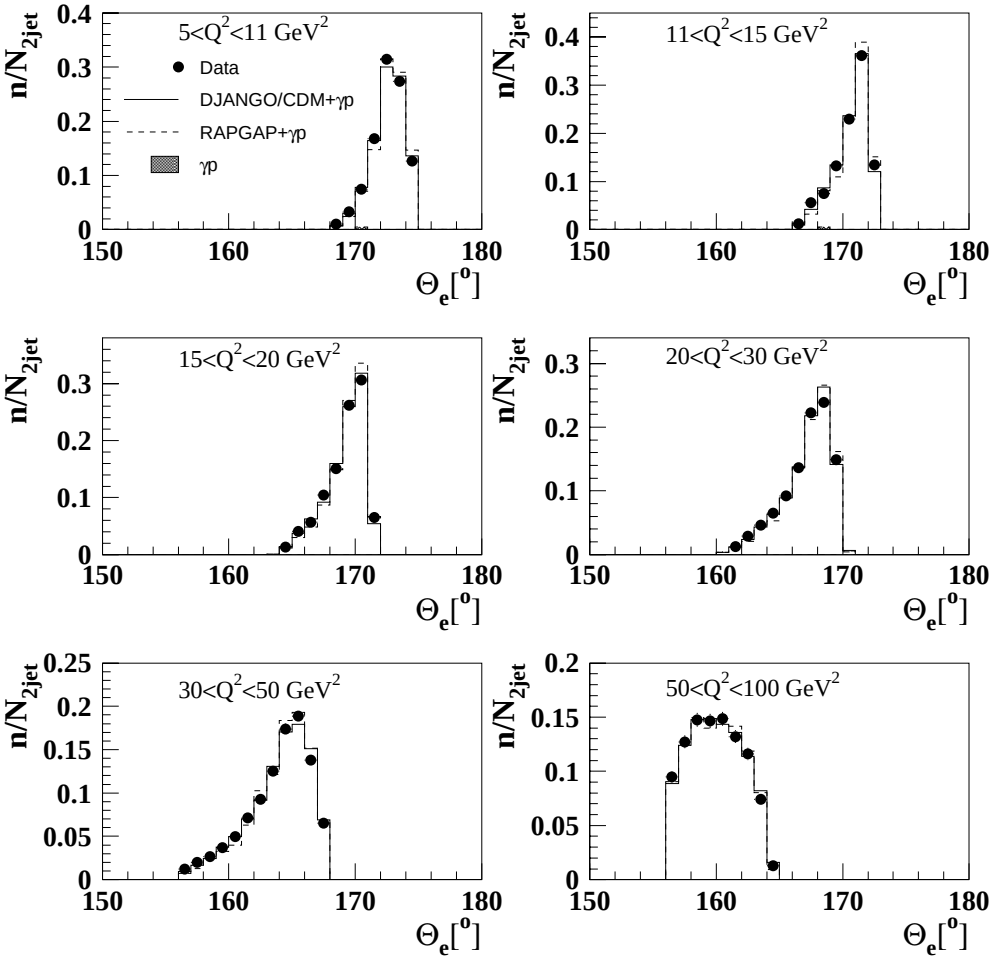

Figure 4.7: Polar angle spectra of the scattered positron in measured dijet events (bullets) for six ranges in x_B compared to the predictions of DJANGO/CDM (full line) and RAPGAP (dashed line) to which the amount of photoproduction background (γp, shaded part) simulated with PHOJET is added.

ment. Therefore, they can be used to study the detector resolution for different x_B and Q^2 ranges which is done by comparing within the Monte Carlo the generated kinematic variables with the reconstructed ones.

The general criteria to estimate the quality of the reconstruction are the stability S and the purity P of the defined analysis bins. They are defined as

$$S = \frac{N_{gen \cap rec}}{N_{gen}} \tag{4.1}$$

$$P = \frac{N_{gen \cap rec}}{N_{rec}}. \tag{4.2}$$

Here N_{gen} is the number of generated DIS events and N_{rec} is the number of reconstructed DIS events in each bin; $N_{gen \cap rec}$ then represents the number of DIS events which are generated and reconstructed in one and the same bin. Table 4.3 show that the stability and the purity are usually better than 70% and approximately of the same size. This leads to the conclusion that for the given binning migration, effects are well under control. Together with the good accuracy seen in the reproduction of the measured spectra by the Monte Carlo simulation, this gives confidence that the determination of the event kinematics is very reliable.

kinematic range		S	P
$5 < Q^2 < 11$	$1 \cdot 10^{-4} < x_B < 1.3 \cdot 10^{-3}$	0.95	0.94
	$1 \cdot 10^{-4} < x_B < 1.7 \cdot 10^{-4}$	0.79	0.83
	$1.7 \cdot 10^{-4} < x_B < 3 \cdot 10^{-4}$	0.81	0.81
	$3 \cdot 10^{-4} < x_B < 5 \cdot 10^{-4}$	0.76	0.73
	$5 \cdot 10^{-4} < x_B < 1.3 \cdot 10^{-4}$	0.85	0.78
$11 < Q^2 < 15$	$1 \cdot 10^{-4} < x_B < 1.8 \cdot 10^{-3}$	0.86	0.85
	$1 \cdot 10^{-4} < x_B < 3 \cdot 10^{-4}$	0.72	0.77
	$3 \cdot 10^{-4} < x_B < 5 \cdot 10^{-4}$	0.74	0.75
	$5 \cdot 10^{-4} < x_B < 10^{-3}$	0.75	0.72
	$10^{-3} < x_B < 1.8 \cdot 10^{-3}$	0.74	0.66
$15 < Q^2 < 20$	$2.3 \cdot 10^{-4} < x_B < 2.2 \cdot 10^{-3}$	0.86	0.84
	$2.3 \cdot 10^{-4} < x_B < 5 \cdot 10^{-4}$	0.76	0.79
	$5 \cdot 10^{-4} < x_B < 10^{-3}$	0.76	0.75
	$10^{-3} < x_B < 2.2 \cdot 10^{-3}$	0.83	0.77
$20 < Q^2 < 30$	$2.5 \cdot 10^{-4} < x_B < 3.3 \cdot 10^{-3}$	0.90	0.88
	$2.5 \cdot 10^{-4} < x_B < 5 \cdot 10^{-4}$	0.71	0.77
	$5 \cdot 10^{-4} < x_B < 10^{-3}$	0.80	0.80
	$10^{-3} < x_B < 3.3 \cdot 10^{-3}$	0.89	0.83
$30 < Q^2 < 50$	$5 \cdot 10^{-4} < x_B < 5.5 \cdot 10^{-3}$	0.93	0.90
	$5 \cdot 10^{-4} < x_B < 10^{-3}$	0.81	0.83
	$10^{-3} < x_B < 5.5 \cdot 10^{-3}$	0.92	0.87
$50 < Q^2 < 100$	$8 \cdot 10^{-4} < x_B < 10^{-2}$	0.96	0.91
	$8 \cdot 10^{-4} < x_B < 2.5 \cdot 10^{-3}$	0.84	0.84
	$2.5 \cdot 10^{-3} < x_B < 10^{-2}$	0.94	0.86

Table 4.3: Stabilities S and purities P for the reconstruction of the kinematic variables x_B and Q^2. The table contains the stabilities and purities obtained for DIS events for the six bins in Q^2 chosen for the single differential analysis of R_2 and its subsequent subdivision into bins of x_B.

4.2.2 Quality of the Jet Measurement

After it has been verified that the event kinematics can be reconstructed with good accuracy from the scattered positron, it will now be investigated whether the simulation is able to describe the properties of the jets formed out of the hadronic final state. If these properties are described then the Monte Carlo can be trusted to give a good image of the detector response.

The most important parameter for the jet selection is the transverse momentum E_t^* of the selected jets because this transverse momentum is the minimum requirement a jet must fulfill before being classified as a dijet event. The E_t^* spectrum of the jets decreases rapidly with increasing transverse momentum of the jets. Therefore, it is rather sensitive to migrations, which are due to the limited angular and energy resolution of the experimental devices. A good reproduction of the migration effects by the simulation can only be expected if the measured and the simulated transverse momentum spectrum agree.

Figure 4.8 shows the measured E_t^* spectrum of the selected jets compared to the results of Monte Carlo simulations, both in linear and logarithmic presentation. The shown spectra are

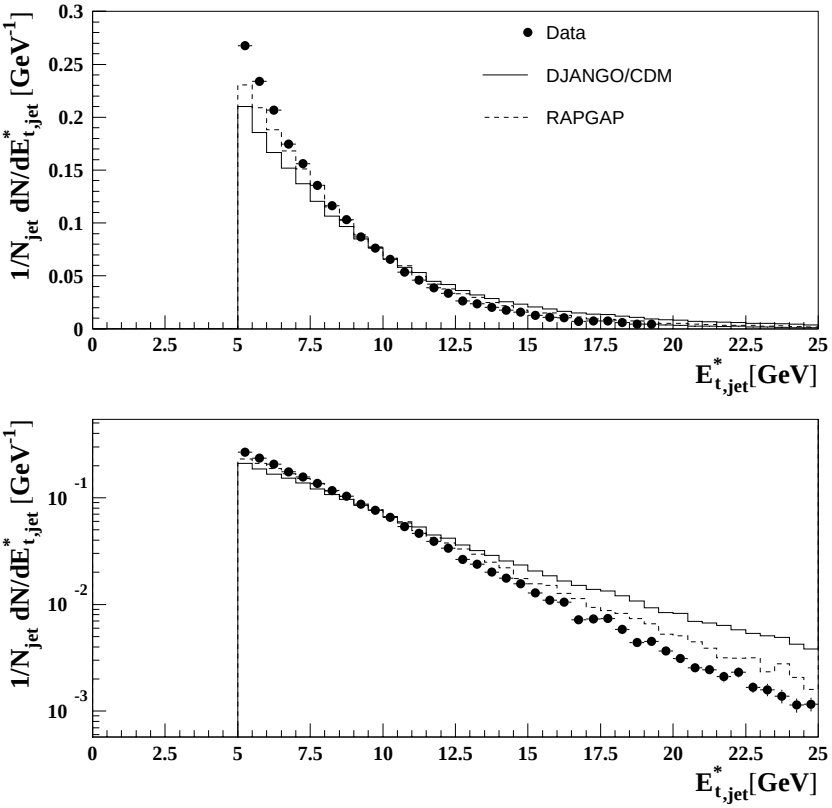

Figure 4.8: Spectra of the transverse momenta E_t^* of the jets in linear and logarithmic representation. The bullets represent the data, the full line represent events simulated with the CDM model and the dashed line represent events simulated with RAPGAP.

normalized to the number of dijet events in the corresponding data samples. Obviously, the measured transverse momentum spectrum is not reproduced by the simulation. The slope of the distributions is quite different. This is true for both Monte Carlo programs which produce an

insufficient number of jets close to the threshold at 5 GeV while at the same time predicting too many jets with large transverse momentum. The situation is better for RAPGAP than for the predictions based on the CDM model.

One possible explanation for the observed difference [CAR99] could be the rejection of events with large transverse energy by the $\mathrm{zVtx_{mul}} < 7$ condition, due to the larger number of tracks expected for high E_t^* jet events. Therefore the analysis has been repeated using only the sub-trigger S_0 (see Section 3.5) which does not contain the $\mathrm{zVtx_{mul}} < 7$ condition. If this condition would be responsible for the discrepancy between the measured transverse momentum spectrum and the simulated one, a better agreement should be found by choosing a trigger setup where the $\mathrm{zVtx_{mul}} < 7$ condition is not used. Figure 4.9 shows a comparison of the E_t^* spectra with and without the inclusion of the $\mathrm{zVtx_{mul}} < 7$ condition. No significant difference is found suggesting

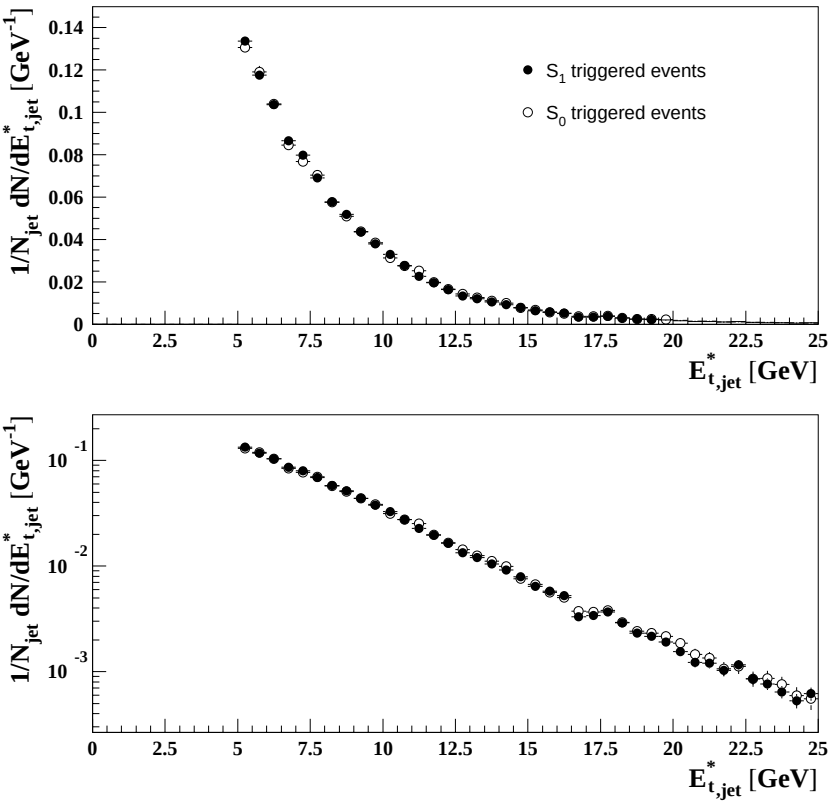

Figure 4.9: Transverse momenta, E_t^*, of the jets the for events which have been triggered by different sub-triggers where one subtrigger, S_1, does contain the $\mathrm{zVtx_{mul}} < 7$ condition, the other subtrigger, S_0, does not contain this trigger element.

that this potential source of the disagreement between the measured and simulated E_t^* spectra can be excluded for the analyzed range of transverse momenta.

Since this deviation has been seen in other analyzes [JET99] and no evidence for an experimental source of the disagreement was found it is necessary to correct the generated and simulated DIS events to the measured E_t^* spectrum in order to ensure that the migrations at the cut boundaries, especially at $E_t^* = 5\,\mathrm{GeV}$, are correctly taken into account.

For a dijet event it is required that two jets composed by the k_t algorithm have to pass

the minimum threshold of 5 GeV. The naive expectation would be that the jet with the lower transverse momentum, referred to as the second jet hereafter, is more sensitive to migration effects than the other because its E_t^* value is closer to the threshold. This assumption is supported by Figure 4.10 where the E_t^* spectra are shown separately for the first and the second jet. While the E_t^* spectrum of the first jet shows a maximum clearly separated from the threshold

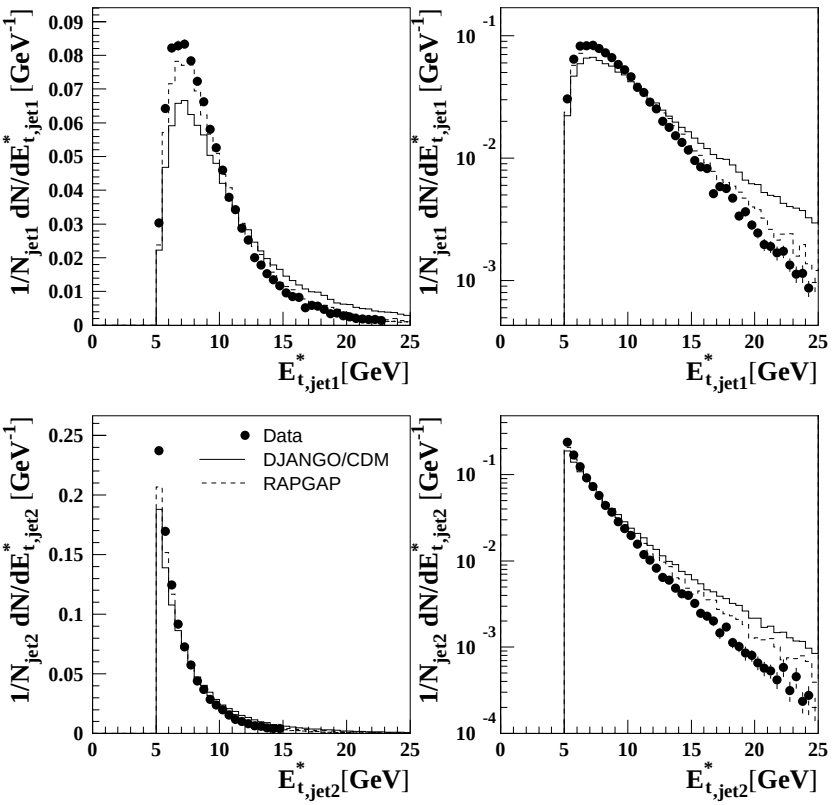

Figure 4.10: The measured E_t^* spectra are shown separately for the hardest jet (jet1) and the second hardest jet (jet2) in comparison to the corresponding spectra of events simulated with the CDM Model (full line) and RAPGAP (dashed line).

the spectrum of the second jet falls sharply immediately from the 5 GeV threshold. Therefore the correction procedure focuses on the correction of the E_t^* spectrum of the second jet. The correction is done by fitting the measured and simulated E_t^* spectra of the second jet as function of its $E_t^* = E_{t,jet2}^*$ as shown in Figure 4.11. The fit starts at $E_t^* = 4$ GeV and uses a superposition of two exponentials

$$f_{corr}(E_{t,jet2}^*) = e^{a \cdot E_{t,jet2}^* + b} + e^{c \cdot E_{t,jet2}^* + d}. \tag{4.3}$$

Figure 4.11 reveals that the shape of the spectra can be well described by such a fit.The obtained fit values are listed in Table 4.4 together with the χ^2 values of the fit. The correction factors are given the following Equation:

$$c_{Et2} = \frac{f_{corr,data}}{f_{corr,MC}}. \tag{4.4}$$

This factor is applied to the simulated events when a dijet event is identified on hadron level under the condition that the second hardest jet on hadron level has at least 4 GeV. Since the Monte

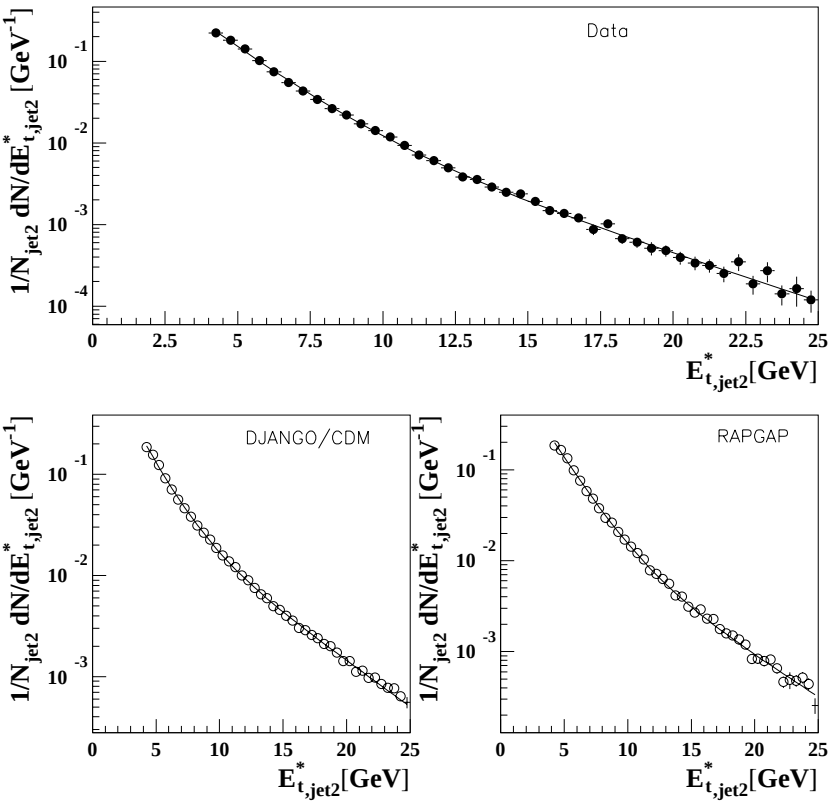

Figure 4.11: The measured and simulated E_t^*spectra of the second jet together with the resulting fit using a superposition of two exponential functions according to Equation 4.3.

	a	b	c	d	χ^2
Data	-0.618 ± 0.008	1.023 ± 0.022	-0.269 ± 0.010	-2.357 ± 0.173	3.85
CDM	-0.584 ± 0.009	0.609 ± 0.036	-0.209 ± 0.003	-2.363 ± 0.064	3.29
RAPGAP	-0.529 ± 0.013	0.510 ± 0.052	-0.208 ± 0.009	-2.874 ± 0.174	2.80

Table 4.4: Parameters to fit the transverse momentum spectrum of the second jet according to Equation 4.3

Carlo generators include leading order matrix elements both jets are to a first approximation balanced in their E_t^* leading to an automatic reweighting of the E_t^* spectrum of the first jet as well.

In Figure 4.12 the corrected transverse momentum spectrum of the simulated events is compared to the (unchanged) E_t^* spectrum as observed in the data. Much better agreement is found

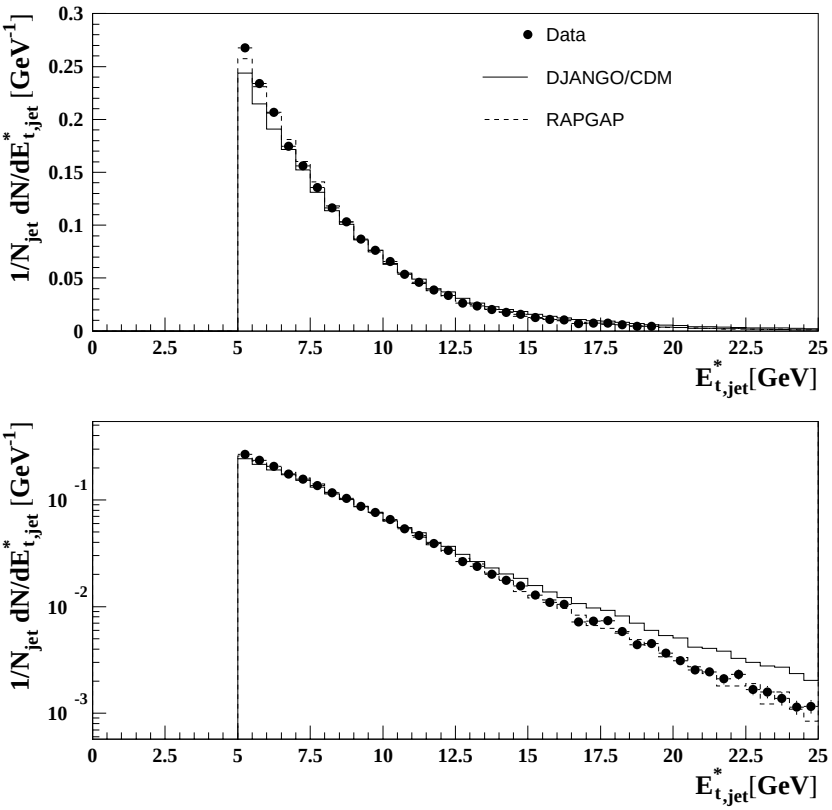

Figure 4.12: The measured E_t^* spectrum (points) is compared to the corrected transverse momentum spectra as given by the Monte Carlo generators CDM (full line) and RAPGAP (dashed line) after detector simulation.

after applying the correction. This leads to the conclusion that migration effects are correctly taken into account. This is supported by Figure 4.13 which shows the corrected E_t^* spectra of the Monte Carlo simulation separately for the first and the second jet in comparison to the measured E_t^* distribution.

A powerful test to check the similarity of the identified jets in the measurement and in the simulation have similar characteristics is the investigation of the transverse energy flow around the jet axis. The transverse energy flow around the jet axes can be illustrated by so called jet profiles where the distance in η^* and ϕ^* between the objects of the hadronic final state and the jet axis weighted by the transverse energy of each object is displayed.

In Figure 4.14 the jet profile is shown for four different ranges in E_t^* of the jets. Here, it is shown as a function of the $\Delta\phi^*$ between the ϕ^* position of the jet axis (ϕ^*_{jet}) and the ϕ^* positions of the objects which contribute to the jet (ϕ^*_{obj}). The objects are taken from a band $|\Delta\eta^*| < 1$ as indicated in the figure. The increase of the energy flow towards $\pm\pi$ shows the presence of

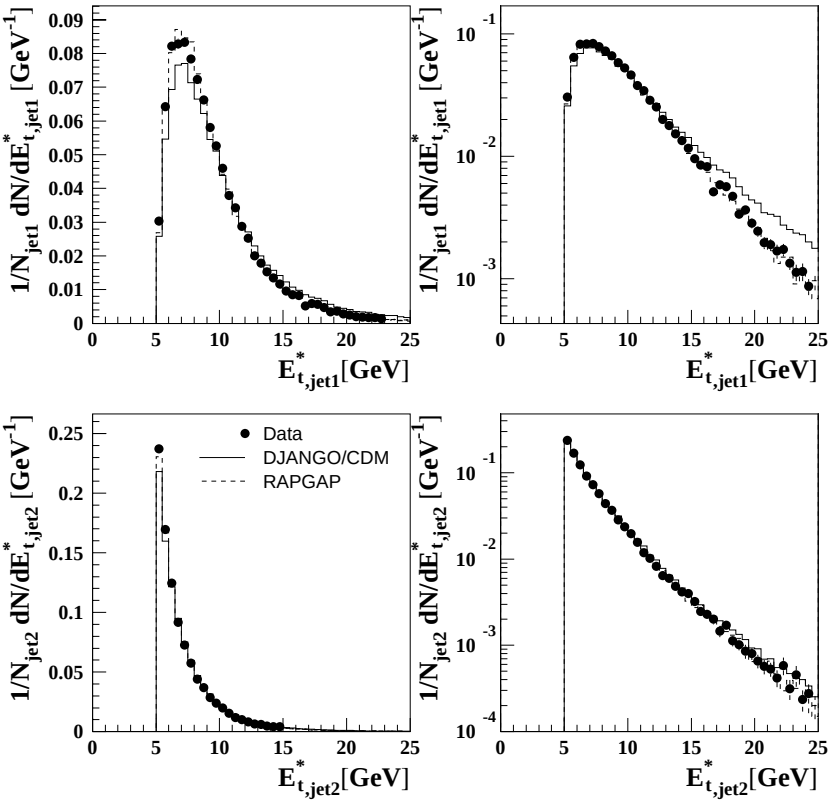

Figure 4.13: The measured E_t^* spectrum (points) is shown separately for the first and the second jet in comparison to the corrected transverse momentum spectra as given by the Monte Carlo generators CDM (full line) and RAPGAP (dashed) line after detector simulation.

the second jet. The different figures are normalized to the number of jets in their respective E_t^* ranges. The separation into various E_t^* regions is necessary since since it is intended to study R_2 for different values of Δ (see Chapter 1), since Δ is equivalent to a different minimum E_t^* required for the first jet. The measured jet profiles are well reproduced by the Monte Carlo simulation.

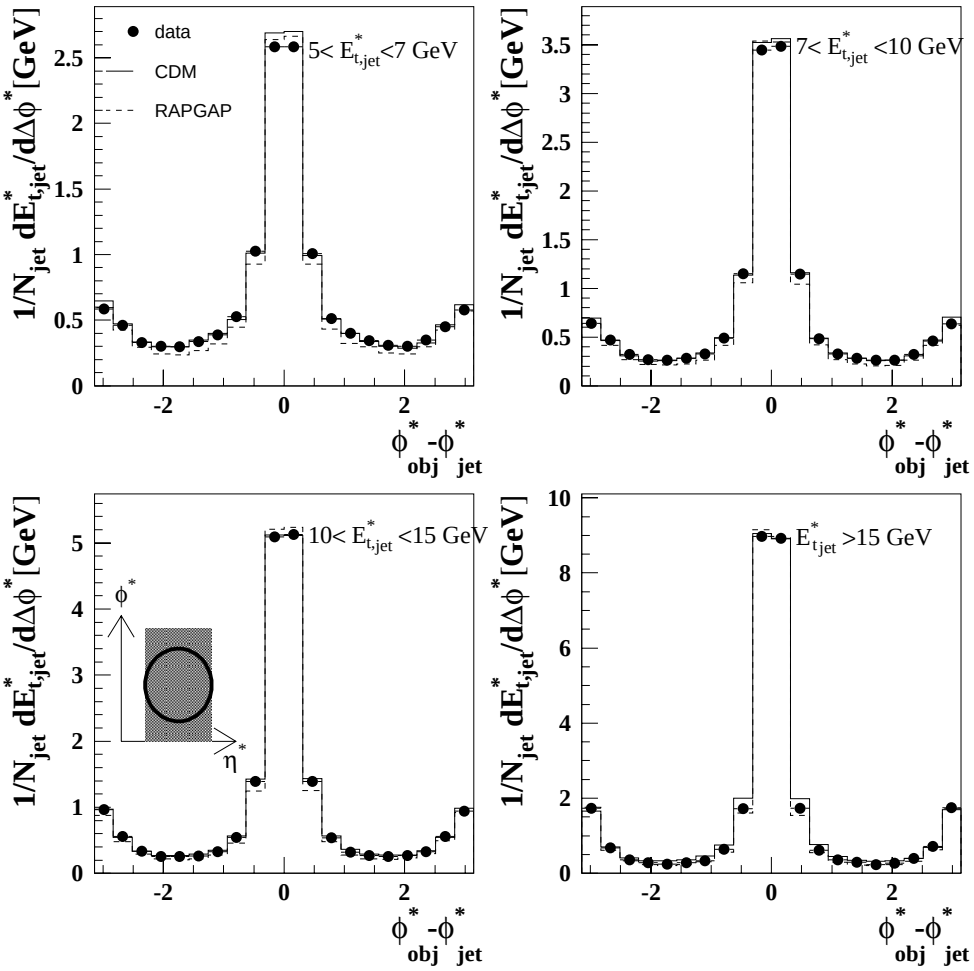

Figure 4.14: Transverse energy flow in dependence of the distance $\Delta\phi^* = \phi^*_{obj} - \phi^*_{jet}$ to the jet axis for different ranges in E_t^*. The band in $\eta^*$from where the objects are taken is corresponds to two times the distance parameter $R = 1$ and is illustrated in the small box in the lower left plot. The data are represented by the points while the simulated events are represented by a full line (CDM) and a dashed line (RAPGAP), respectively.

The energy flow with respect to the η^* position of the jet axis has also been studied and is presented in Figure 4.15. In this case the objects are taken from a band $|\Delta\phi^*| < 1$. Again a good agreement between the measured jet profiles and the simulated jet profiles is observed. The asymmetry in the distribution showing an enhancement for positive $\Delta\eta^*$ reflects the higher energy flow in the direction of the proton remnant caused by color interactions between the proton remnant and the jets originating from the hard subprocess.

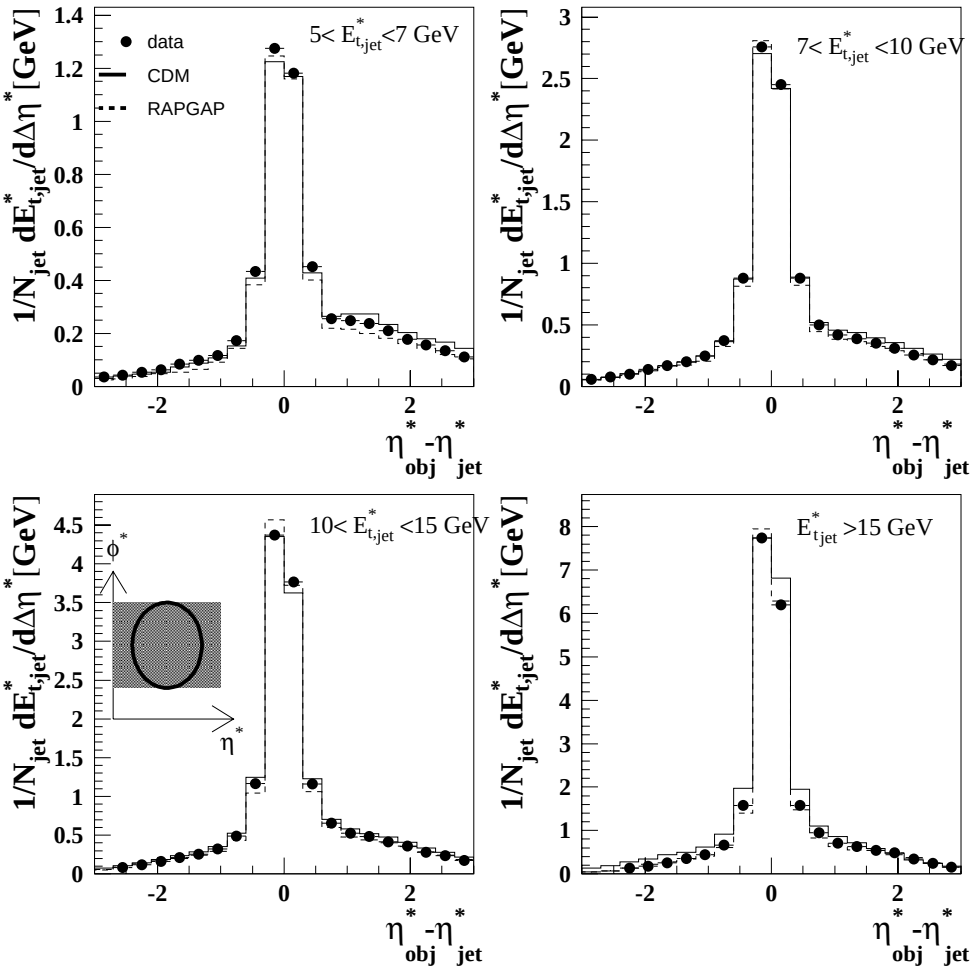

Figure 4.15: Transverse energy flow in dependence of the distance $\Delta\eta^* = \eta^*_{obj} - \eta^*_{jet}$ to the jet axis for different ranges in the transverse momentum of the jets. The band in ϕ^* from where the objects are taken corresponds to two times the distance parameter $R = 1$ and is illustrated in the lower left plot. The data are represented by the points while the simulated events are represented by a full line (CDM) and a dashed line (RAPGAP), respectively.

After demonstrating that the transverse momentum as well as the jet profiles can be reproduced by the Monte-Carlo simulation several other jet variables must be studied before the Monte Carlo Models can be trusted to provide a correction for detector effects. A first step in this respect is the investigation of the angular distributions of the jets. This is important to ensure that acceptance limitations of the experimental devices are correctly taken into account when correcting the data to the hadron level. Figures 4.16 and 4.17 show the distributions of pseudo rapidities of the jets for different bins in x_B and Q^2. The figures demonstrate that the

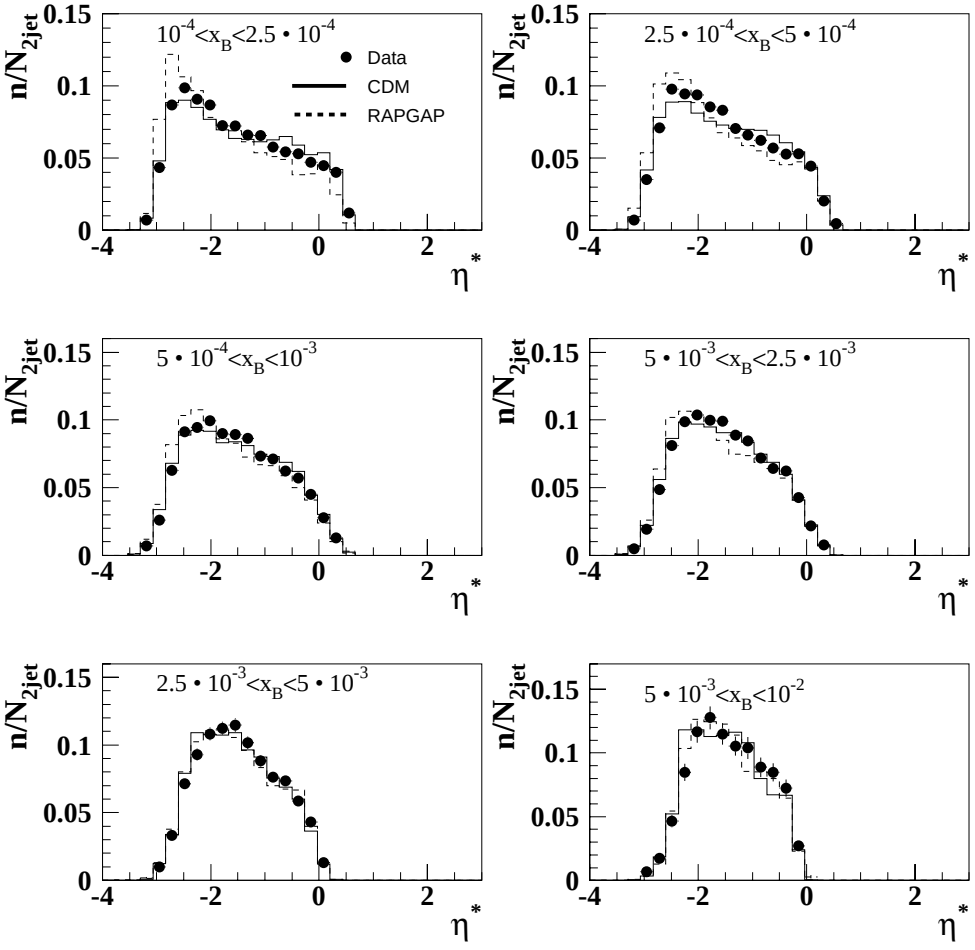

Figure 4.16: Distribution of pseudo rapidities η^* for different bins in x_B as measured in the data (points) compared to Monte Carlo predictions using the CDM Model (full line) and the RAPGAP event generator (dashed line).

measured η^* distributions are reasonably reproduced by the Monte Carlo simulation. The CDM model provides a slightly better description of the data especially at small values of η^*. However, in most cases, the measured spectra are situated between the prediction of the RAPGAP and the CDM Model indicating that acceptance effects can adequately be taken into account by averaging both models before the determination of any correction factor.

The longitudinally invariant k_t algorithm defines the jets in terms of the pseudo rapidity η^*,

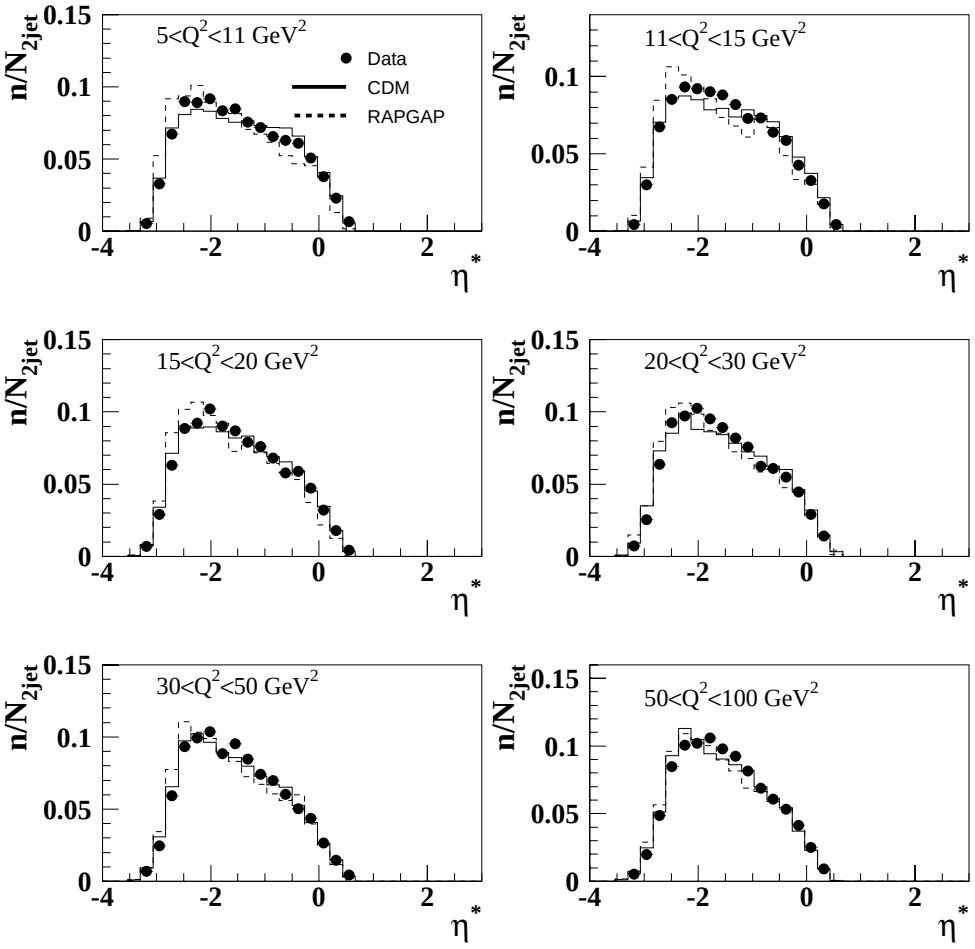

Figure 4.17: Distribution of pseudo rapidities η^* for different bins in Q^2 as measured in the data compared to Monte Carlo predictions using the CDM Model (full line) and the RAPGAP event generator (dashed line).

the azimuthal angle ϕ^*, and the transverse momentum E_t^* of the jets, see Section 1.6.1. Therefore, it is natural to study the jet resolution in these variables as well. The study is performed by comparing the quantities as measured on the hadron level (had) to the corresponding quantities on the detector level (det). The resolution in E_t^* is of particular interest here for the intended measurement of R_2 as a function of Δ; the E_t^* resolution will define the minimal step-width in Δ.

Figure 4.18 shows the resolution in η^* separately for the forward and the backward jet. The

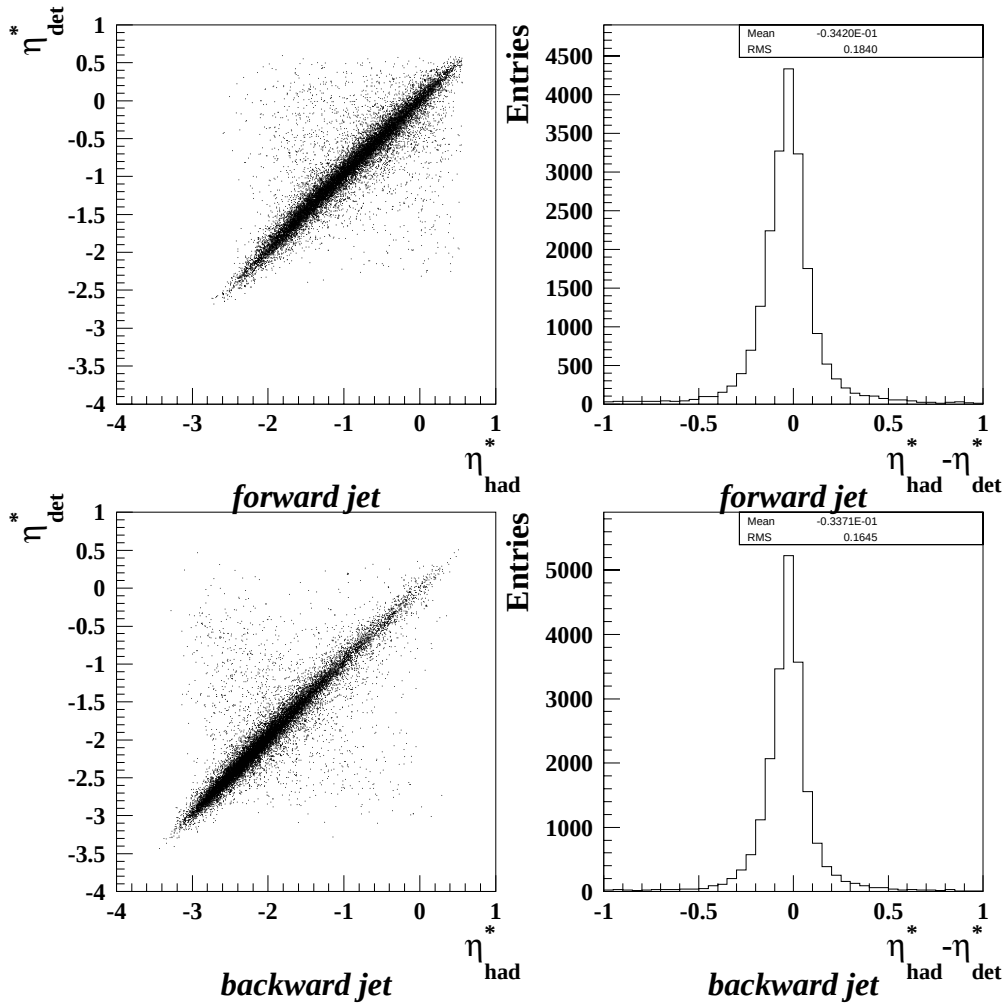

Figure 4.18: Left part: Correlation in the pseudo rapidity η^* between the jets on detector level η^*_{det} and on hadron level η^*_{had} for the forward (upper part) and the backward jet (lower part). Right part: Resolution in η^* estimated by the difference between the η^*positions on detector and on hadron level.

forward jet is labeled as that with the larger pseudo rapidity value. The correlation is visualized by the scatter plots in the left part of the figure. The right part of the figure shows the differences in η^* of the jets on detector level relative to that on the hadron level. From these plots, the resolution (RMS) in η^* can be quantified to 0.18 for the forward and to 0.17 for the backward jet. The slightly better resolution achieved for the backward jet can be explained by the fact

that it is measured more in the central part of the H1 detector where the spatial resolution in pseudo-rapidity is better than in the forward region.

In Figure 4.19 the resolution in terms of ϕ^* is shown. When plotting the value on detector level

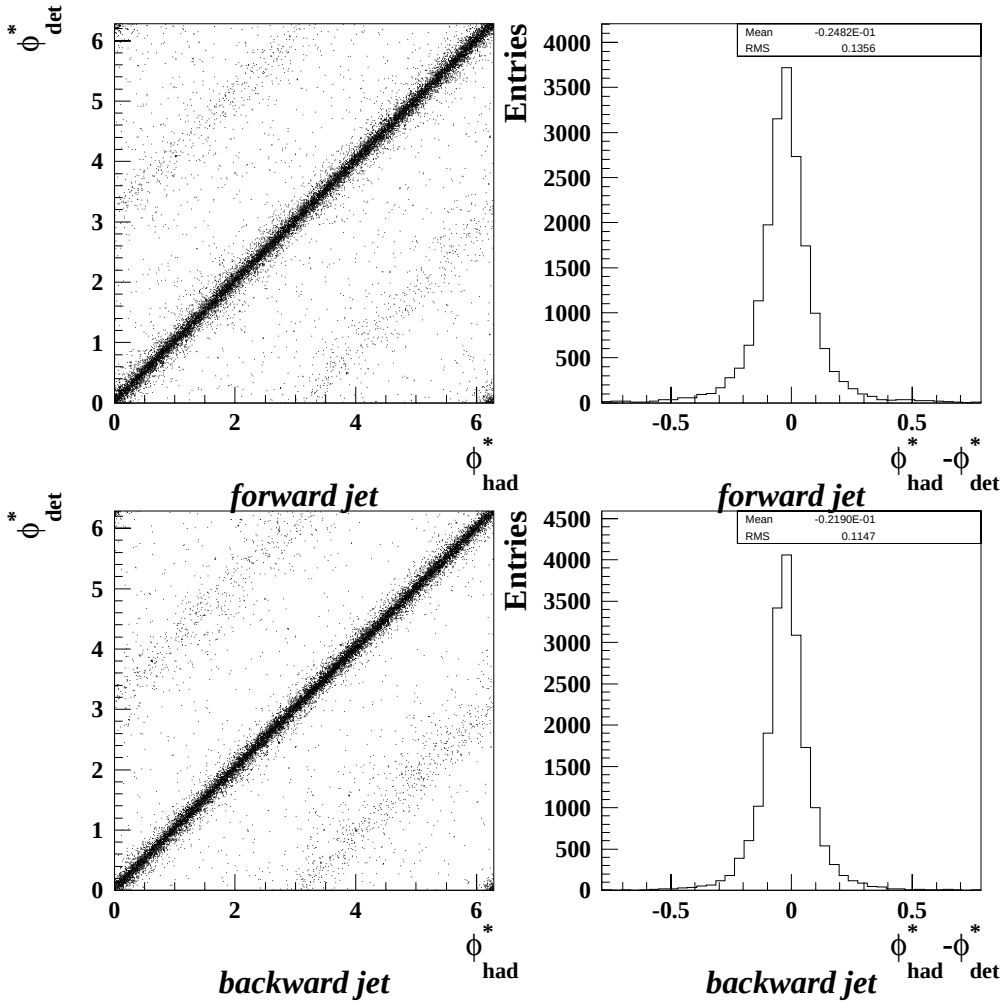

Figure 4.19: Left part: Correlation in the azimuthal angle ϕ^* between the jets on detector level ϕ^*_{det} and on hadron level ϕ^*_{had} for the forward (upper part) and the backward jet (lower part). Right part: Resolution in ϕ^* estimated by the difference between the ϕ^* positions on detector and on hadron level.

(ϕ^*_{det}) versus the value on hadron level (ϕ^*_{had}), three different bands are observed, one around the axis $\phi^*_{det} = \phi^*_{had}$ and two around the axis $\phi^*_{det} = \phi^*_{had} \pm \pi$. The latter two bands are due to events in which the η^* position of the forward and the backward jets have been misidentified. Since the two hardest jets are mainly back-to-back in the $\gamma^* p$ frame this misidentification results in a $\Delta\phi = \pm\pi$ difference in the azimuthal angle. Fortunately, the bands at $\phi^*_{had} \pm \pi$ are only weakly populated which underlines that the detector level provides a good image of the hadron level. From the histograms in the right part of Figure 4.19, the resolution in ϕ^* can be quantified to 0.14 rad for the forward and to 0.12 rad for the backward jet.

The resolution of the transverse momentum measurement is investigated in Figure 4.20. The

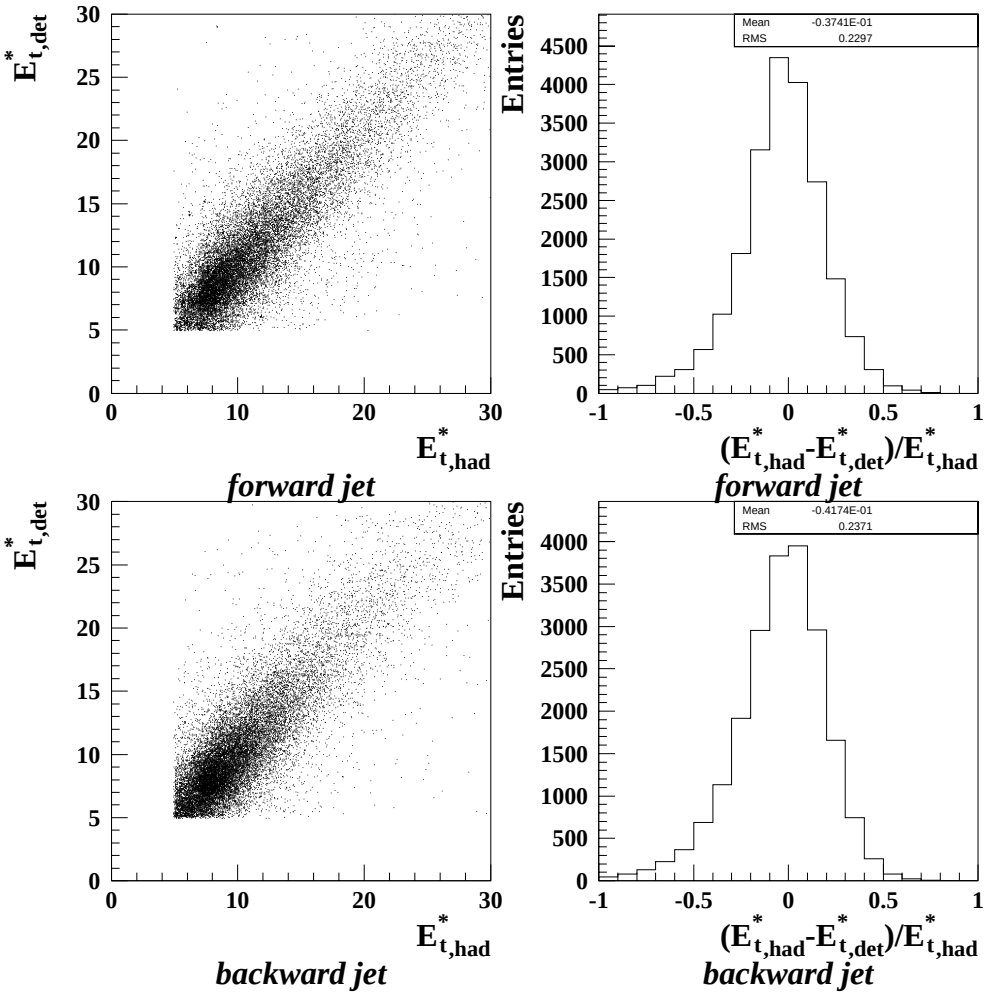

Figure 4.20: Left part: Correlation in the transverse momentum E_t^* between the jets on detector level $E^*_{t,det}$ and on hadron level $E^*_{t,had}$ for the forward (upper part) and the backward jet (lower part). Right part: Resolution in E_t^* estimated by the difference between the E_t^* values on detector and on hadron level normalized to the E_t^* on hadron level.

edges visible in the scatter plots reflect the imposed cuts on the E_t^* on the jets. As a result, one obtains a resolution of $(23.0 \pm 0.2)\%$ for the forward and $(23.7 \pm 0.2)\%$ for the backward jet. This limits the step width for the intended investigation of R_2 as function of Δ to $\Delta = 1\,\mathrm{GeV}$.

Requiring that a DIS event has been identified simultaneously on detector and on hadron level, one can define the jet selection efficiency as the number of jets identified on detector and hadron level divided by the number of jets identified on hadron level. In Table 4.5 the efficiencies are listed for five different values of Δ, showing that the jets on hadron level can be reconstructed

Δ/GeV	0	1	2	4	7
$N_{2jet,had}$	33647	31249	26513	17445	9409
$N_{2jet,det}$	34405	31979	25597	19205	10851
$N_{2jet,both}$	25827	24382	21255	14315	7975
Efficiency=$\frac{N_{2jet,both}}{N_{2jet,had}}$	0.768	0.780	0.802	0.821	0.848

Table 4.5: The efficiencies for the jet identification. Here $N_{2jet,had}$ denotes the number of jets identified on hadron level, $N_{2jet,det}$ denotes the number of jets on detector level and $N_{2jet,both}$ denotes the number of on both levels .

on the detector level with an efficiency of around 80%.

4.3 Determination of Correction Factors

Since the Monte Carlos reproduce the data rather well for all the relevant distributions, they can be used to correct the data for background contamination, finite detector acceptance and resolution and for QED effects. For this a bin-by-bin correction is performed such that for each chosen analysis bin, as defined in Section 4.1, two corrections are applied:

1. For each bin the remaining γp background is subtracted, which reaches 15% for the lowest x_B, Q^2 bin for the DIS events. For the dijet subsample, however, it never exceeds 2.5%. As mentioned before (see Section 4.2.1) the uncertainties especially at low x_B, Q^2 will be included in the systematic error.

2. The raw R_2 measurement is corrected bin-by-bin by multiplying it with the ratio

$$C'_{corr} = \frac{R^{nrad}_{2,had}}{R^{rad}_{2,det}}, \tag{4.5}$$

as determined from the Monte-Carlo simulations. Here, $R^{nrad}_{2,had}$ is the dijet rate calculated on the hadron level for events which have been generated without QED radiation while $R^{rad}_{2,det}$ represents the dijet rate on detector level with QED radiation effects included. In this way, the influence of QED radiation and effects of the limited detector acceptances are corrected in one step. The correction factor C_{corr} which is taken as the average value of the correction factors C'_{corr} obtained by ARIADNE (CDM Model) and RAPGAP. The differences between the correction factors determined from the two models is taken as a systematic error such that all observed differences in the various distributions (see previous sections) are accounted for automatically. The resulting values for C_{corr} are given in Table 4.6 and 4.7 for the single differential measurement for three values of Δ.

For the double differential measurement they are listed in Table 4.8 and a graphical overview is shown in Figure 4.21.

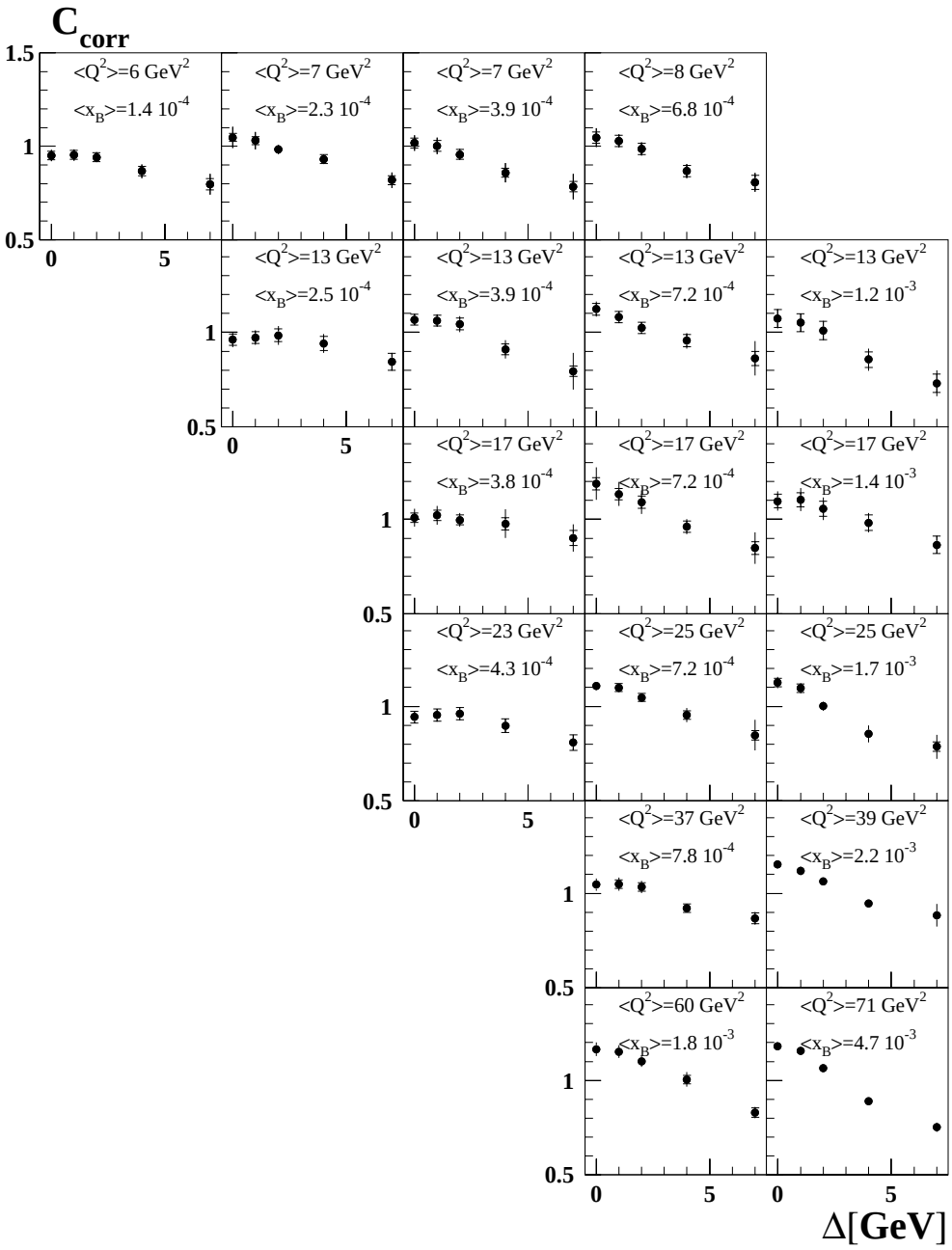

Figure 4.21: Correction functions for the x_B, Q^2 bins used double differential measurement of R_2. The inner error bars reflects the statistical error and the outer error bars statistical and the systematic error added in quadrature.

kinematic range	C_{corr}		
x_B	$\Delta = 0$	$\Delta = 2$	$\Delta = 7$
$10^{-4} < x_B < 2.5\,10^{-4}$	$0.981 \pm 0.015 \pm 0.025$	$0.948 \pm 0.015 \pm 0.002$	$0.798 \pm 0.029 \pm 0.046$
$2.5\,10^{-4} < x_B < 5\,10^{-4}$	$0.986 \pm 0.012 \pm 0.033$	$0.944 \pm 0.013 \pm 0.025$	$0.771 \pm 0.016 \pm 0.026$
$5\,10^{-4} < x_B < 10^{-3}$	$1.013 \pm 0.011 \pm 0.030$	$0.947 \pm 0.011 \pm 0.014$	$0.767 \pm 0.013 \pm 0.051$
$10^{-3} < x_B < 2.5\,10^{-3}$	$1.121 \pm 0.011 \pm 0.017$	$1.046 \pm 0.012 \pm 0.006$	$0.833 \pm 0.015 \pm 0.027$
$2.5\,10^{-3} < x_B < 5\,10^{-3}$	$1.143 \pm 0.017 \pm 0.003$	$1.049 \pm 0.028 \pm 0.032$	$0.755 \pm 0.022 \pm 0.046$
$5\,10^{-3} < x_B < 10^{-2}$	$1.185 \pm 0.028 \pm 0.028$	$1.049 \pm 0.028 \pm 0.032$	$0.725 \pm 0.034 \pm 0.028$

Table 4.6: Correction factors for the different kinematic ranges in x_B of the single differential measurement of R_2 for three different values of Δ together with their statistical and systematic error.

kinematic range	$C_{corr} \pm \sigma_{stat} \pm \sigma_{syst.}$		
Q^2/GeV^2	$\Delta = 0$	$\Delta = 2$	$\Delta = 7$
$5 < Q^2 < 11$	$1.008 \pm 0.011 \pm 0.042$	$0.954 \pm 0.011 \pm 0.017$	$0.786 \pm 0.014 \pm 0.037$
$11 < Q^2 < 15$	$1.062 \pm 0.016 \pm 0.020$	$1.015 \pm 0.017 \pm 0.018$	$0.817 \pm 0.020 \pm 0.058$
$15 < Q^2 < 20$	$1.106 \pm 0.017 \pm 0.056$	$1.052 \pm 0.017 \pm 0.042$	$0.874 \pm 0.022 \pm 0.007$
$20 < Q^2 < 15$	$1.097 \pm 0.013 \pm 0.013$	$1.018 \pm 0.013 \pm 0.009$	$0.823 \pm 0.017 \pm 0.061$
$30 < Q^2 < 50$	$1.124 \pm 0.012 \pm 0.010$	$1.056 \pm 0.012 \pm 0.001$	$0.879 \pm 0.017 \pm 0.031$
$50 < Q^2 < 100$	$1.171 \pm 0.012 \pm 0.014$	$1.075 \pm 0.012 \pm 0.007$	$0.781 \pm 0.016 \pm 0.001$

Table 4.7: Corrections factors for the different kinematic ranges in Q^2 of the single differential measurement of R_2 for three different values of Δ together with their statistical and systematic errors.

With this the corrected dijet rate, R_2, is defined as

$$R_2 = \frac{N_{2jet,DIS} - N_{2jet,\gamma p}}{N_{DIS} - N_{\gamma p}} \ . \tag{4.6}$$

To study the influence of QED radiation alone an additional correction factor has been determined

$$C_{rad} = \frac{R^{nrad}_{2,had}}{R^{rad}_{2,had}} \ , \tag{4.7}$$

for each bin used in the single differential measurement of R_2. The influence is studied for the central cut scenario i.e. $\Delta = 2\,\mathrm{GeV}$ since QED radiation primarily affects the event kinematics and will therefore be approximately the same for different values of Δ. Figure 4.22 shows the distribution of C_{rad} as a function of x_B and Q^2 indicating an 18% effect on average which is relatively independent of x_B and Q^2.

4.4 Experimental Uncertainties

In this section the main experimental uncertainties are estimated. Primary emphasis is put on the precision of the electromagnetic energy scale of the SpaCal and on the investigation of the precision of the hadronic energy scale, which turns out to be the dominant error source for the measurement.

kinematic range		C_{corr}				
Q^2/GeV^2	$x_B/10^{-4}$	$\Delta = 0$	$\Delta = 1$	$\Delta = 2$	$\Delta = 4$	$\Delta = 7$
$5-11$	$1-1.7$	$0.950 \pm 0.024 \pm 0.017$	$0.954 \pm 0.024 \pm 0.018$	$0.941 \pm 0.025 \pm 0.009$	$0.867 \pm 0.025 \pm 0.026$	$0.797 \pm 0.029 \pm 0.046$
	$1.7-3$	$1.047 \pm 0.022 \pm 0.051$	$1.030 \pm 0.022 \pm 0.040$	$0.984 \pm 0.021 \pm 0.014$	$0.930 \pm 0.024 \pm 0.004$	$0.818 \pm 0.025 \pm 0.034$
	$3-5$	$1.017 \pm 0.027 \pm 0.031$	$1.001 \pm 0.028 \pm 0.033$	$0.957 \pm 0.027 \pm 0.010$	$0.858 \pm 0.023 \pm 0.047$	$0.784 \pm 0.028 \pm 0.063$
	$5-13$	$1.046 \pm 0.030 \pm 0.040$	$1.029 \pm 0.030 \pm 0.018$	$0.986 \pm 0.030 \pm 0.016$	$0.868 \pm 0.030 \pm 0.024$	$0.807 \pm 0.038 \pm 0.032$
$11-15$	$1.7-3$	$0.961 \pm 0.030 \pm 0.025$	$0.971 \pm 0.031 \pm 0.024$	$0.984 \pm 0.034 \pm 0.036$	$0.941 \pm 0.038 \pm 0.032$	$0.844 \pm 0.045 \pm 0.016$
	$3-5$	$1.067 \pm 0.028 \pm 0.040$	$1.062 \pm 0.029 \pm 0.015$	$1.044 \pm 0.032 \pm 0.029$	$0.909 \pm 0.029 \pm 0.040$	$0.794 \pm 0.028 \pm 0.092$
	$5-10$	$1.122 \pm 0.032 \pm 0.026$	$1.080 \pm 0.030 \pm 0.007$	$1.023 \pm 0.030 \pm 0.002$	$0.955 \pm 0.032 \pm 0.027$	$0.861 \pm 0.038 \pm 0.083$
	$10-18$	$1.073 \pm 0.048 \pm 0.016$	$1.051 \pm 0.047 \pm 0.004$	$1.010 \pm 0.050 \pm 0.006$	$0.855 \pm 0.041 \pm 0.043$	$0.730 \pm 0.048 \pm 0.048$
$15-20$	$2.4-5$	$1.008 \pm 0.026 \pm 0.039$	$1.021 \pm 0.027 \pm 0.042$	$0.997 \pm 0.026 \pm 0.024$	$0.977 \pm 0.032 \pm 0.069$	$0.902 \pm 0.039 \pm 0.061$
	$5-10$	$1.189 \pm 0.032 \pm 0.080$	$1.134 \pm 0.030 \pm 0.056$	$1.091 \pm 0.032 \pm 0.054$	$0.961 \pm 0.029 \pm 0.028$	$0.848 \pm 0.033 \pm 0.078$
	$10-22$	$1.097 \pm 0.036 \pm 0.037$	$1.104 \pm 0.038 \pm 0.048$	$1.056 \pm 0.041 \pm 0.044$	$0.982 \pm 0.040 \pm 0.032$	$0.864 \pm 0.046 \pm 0.007$
$20-30$	$3-5$	$0.943 \pm 0.031 \pm 0.002$	$0.953 \pm 0.032 \pm 0.012$	$0.961 \pm 0.033 \pm 0.010$	$0.898 \pm 0.035 \pm 0.008$	$0.808 \pm 0.041 \pm 0.006$
	$5-10$	$1.109 \pm 0.021 \pm 0.009$	$1.099 \pm 0.021 \pm 0.006$	$1.047 \pm 0.022 \pm 0.002$	$0.954 \pm 0.022 \pm 0.029$	$0.848 \pm 0.025 \pm 0.078$
	$10-33$	$1.125 \pm 0.023 \pm 0.019$	$1.095 \pm 0.023 \pm 0.015$	$1.002 \pm 0.021 \pm 0.014$	$0.855 \pm 0.020 \pm 0.041$	$0.787 \pm 0.025 \pm 0.058$
$30-50$	$5-10$	$1.046 \pm 0.021 \pm 0.024$	$1.049 \pm 0.021 \pm 0.027$	$1.034 \pm 0.022 \pm 0.023$	$0.921 \pm 0.022 \pm 0.002$	$0.868 \pm 0.029 \pm 0.017$
	$10-55$	$1.152 \pm 0.016 \pm 0.003$	$1.119 \pm 0.015 \pm 0.018$	$1.063 \pm 0.016 \pm 0.007$	$0.947 \pm 0.017 \pm 0.004$	$0.884 \pm 0.021 \pm 0.056$
$50-100$	$8-25$	$1.164 \pm 0.020 \pm 0.030$	$1.152 \pm 0.020 \pm 0.026$	$1.101 \pm 0.020 \pm 0.022$	$1.005 \pm 0.023 \pm 0.031$	$0.830 \pm 0.025 \pm 0.018$
	$25-100$	$1.180 \pm 0.017 \pm 0.006$	$1.156 \pm 0.018 \pm 0.009$	$1.064 \pm 0.017 \pm 0.001$	$0.890 \pm 0.017 \pm 0.004$	$0.751 \pm 0.020 \pm 0.012$

Table 4.8: Correction factors for the double differential measurement of R_2 as a function of x_B in bins of Q^2. The given errors are the statistical errors given by the limited amount of Monte Carlo events and the systematic error from the model uncertainty .

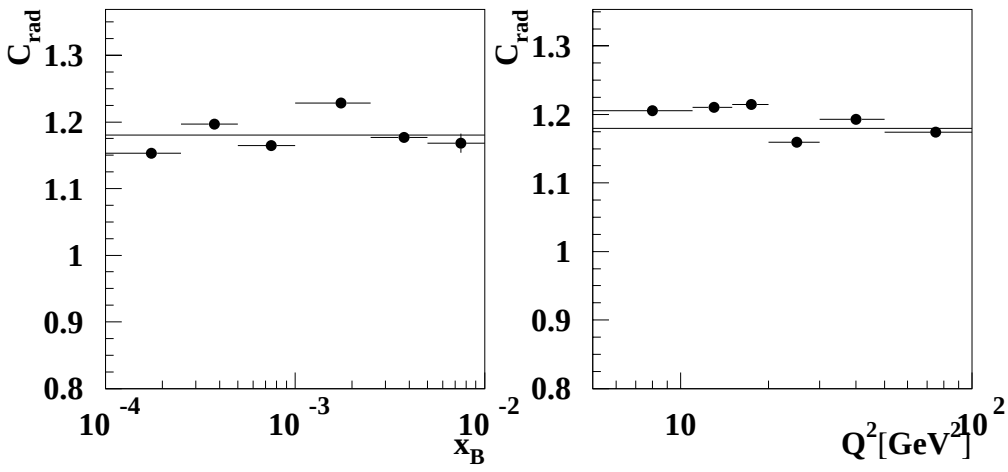

Figure 4.22: The ratio C_{rad} of the dijet rate between events which have been generated without QED radiation and events which have been generated including QED radiation, shown as a function of x_B and Q^2.

The uncertainty of the electromagnetic energy scale of the SpaCal leads to a systematic error in the determination of the event kinematics, in particular in the region of large x_B, i.e. low y (see Section 1.1.1).

To estimate the precision, a reference scale is needed. Such a scale is given when determining the energy of the scattered positron by the double angle method, E_{DA}, which is independent of the energy measurement in the SpaCal. For a perfect detector the ratio $E_e^{'}/E_{DA}$ is expected to be one. In Figure 4.23 the $(E_e^{'}/E_{DA})$ distributions, measured for three ranges of Q^2, are compared to the corresponding Monte Carlo distributions. Good agreement between the measured

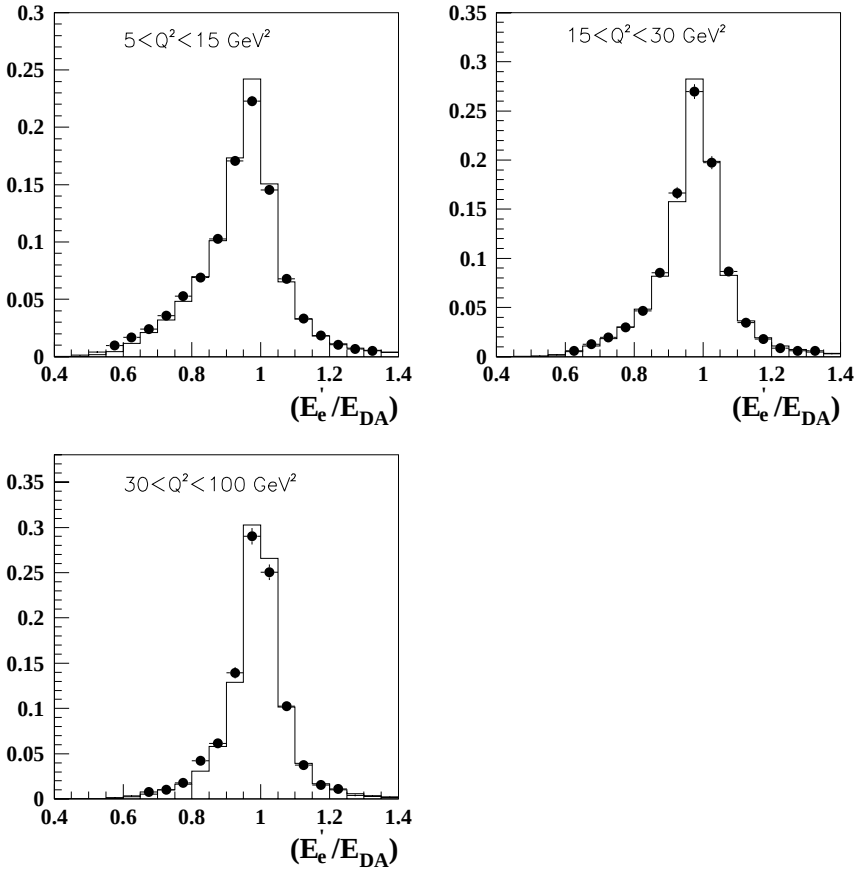

Figure 4.23: Ratio of measured energy of the scattered positron to the energy as obtained by the double angle method. The ratios are shown for three different regions in Q^2 for data (bullets) and simulated events (full line).

and the simulated spectra is observed. The mean values of these distributions listed in Table 4.9 indicate that the electromagnetic energy scale of the SpaCal is known to the level of 1%. The precise knowledge of the electromagnetic energy scale is mandatory for the precise determination of the hadronic energy scale. From momentum conservation, it can be derived that the transverse momentum $E_{t,e}$ of the scattered positron has to be balanced by the total transverse momentum $E_{t,h}$ of the hadronic final state which allows a coupling of the hadronic energy measurement to the well known electromagnetic energy scale of the SpaCal. The E_t balance, i.e. $E_{t,h}/E_{t,e}$, is again expected to be close to unity and can serve as a measure of the precision of

	$5 < Q^2 < 15$	$15 < Q^2 < 30$	$30 < Q^2 < 100$
$< E_e^{'}/E_{DA} >_{Data}$	0.939	0.968	0.985
$< E_e^{'}/E_{DA} >_{MC}$	0.946	0.970	0.989
Ratio	0.993	0.998	0.996

Table 4.9: Mean values of the $< E_e^{'}/E_{DA} >$ratios for three different kinematic ranges for data and simulated (MC) events. The double ratio which is built from the single ratios serves as an estimation for the precision of the electromagnetic energy scale of the SpaCal.

the hadronic energy scale. However, to account for the unknown loss of transverse energy by hadronic final state particles escaping through the beam-pipe the measured E_t balance has to be compared to the E_t balance obtained from simulated events. Therefore, the E_t balance is built for measured and simulated events and only the deviations from unity of the double ratio, i.e. $((E_{t,h}/E_{t,e})_{Data}/(E_{t,h}/E_{t,e})_{MC})$ are taken for the estimation of the uncertainty of the hadronic energy scale.

Simulated DIS Events generated by RAPGAP have been used for the investigation of the hadronic energy scale uncertainties. The E_t balance obtained for measured and simulated DIS events is shown in Figure 4.24 as a function of the angle of the hadronic final state γ_h (see Section 1.1.1) together with the defined double ratio. The figure reveals good agreement between measurement and simulation to a precision of better than 2.5% in most of the regions of the accessible phase space.

In Figure 4.25, the E_t balance is shown for dijet events as a function of the position in rapidity for the most forward jet. The agreement between the measurement and the detector simulation is quantified in Figure 4.26, where the mean values of the measured and simulated E_t balance are compared. The results are compatible with the 4% precision of the hadronic energy scale of the LAr calorimeter as quoted in [FLE98]. An uncertainty of $\pm 4\%$ will therefore be assigned to the hadronic energy scale.

Part of the hadronic final state, especially at low x_B, is scattered into the backward region and absorbed by the SpaCal calorimeters. Therefore its response to hadronic energy flow has to be investigated as well. This is done by studying the y-balance, y_h/y_e (a) for all DIS events (Figure 4.27a) and (b) for those events with $\gamma_h > 170^o$ where the hadronic energy in the SpaCal is enhanced (Figure 4.27b) . Both distributions are well reproduced by the Monte Carlo simulation demonstrating that also the hadronic response of the SpaCal is reasonably well understood. However, more detailed studies within the ELAN working group of the H1 collaboration, see [ZHO99] and [GLA98], and of the response of the SpaCal to single charged π [GAR00] reveal a 7% systematic uncertainty for the hadronic energy scale of the SpaCal calorimeters which will be used hereafter.

4.4.1 Summary of Systematic Uncertainties

The typical change of the rate obtained by the variation of the different sources of experimental and theoretical uncertainties within their given limits is summarized in Table 4.10.

The dominant error source is the 4% uncertainty of the hadronic energy scale for which the systematic error is typically 10% and increases to 20% for large Δ. The other error sources among which the uncertainty of the electromagnetic energy scale of the SpaCal is the most prominent one have an relatively small influence on the systematic uncertainty. The typical systematic error as induced the SpaCal electromagnetic energy scale is 6%.

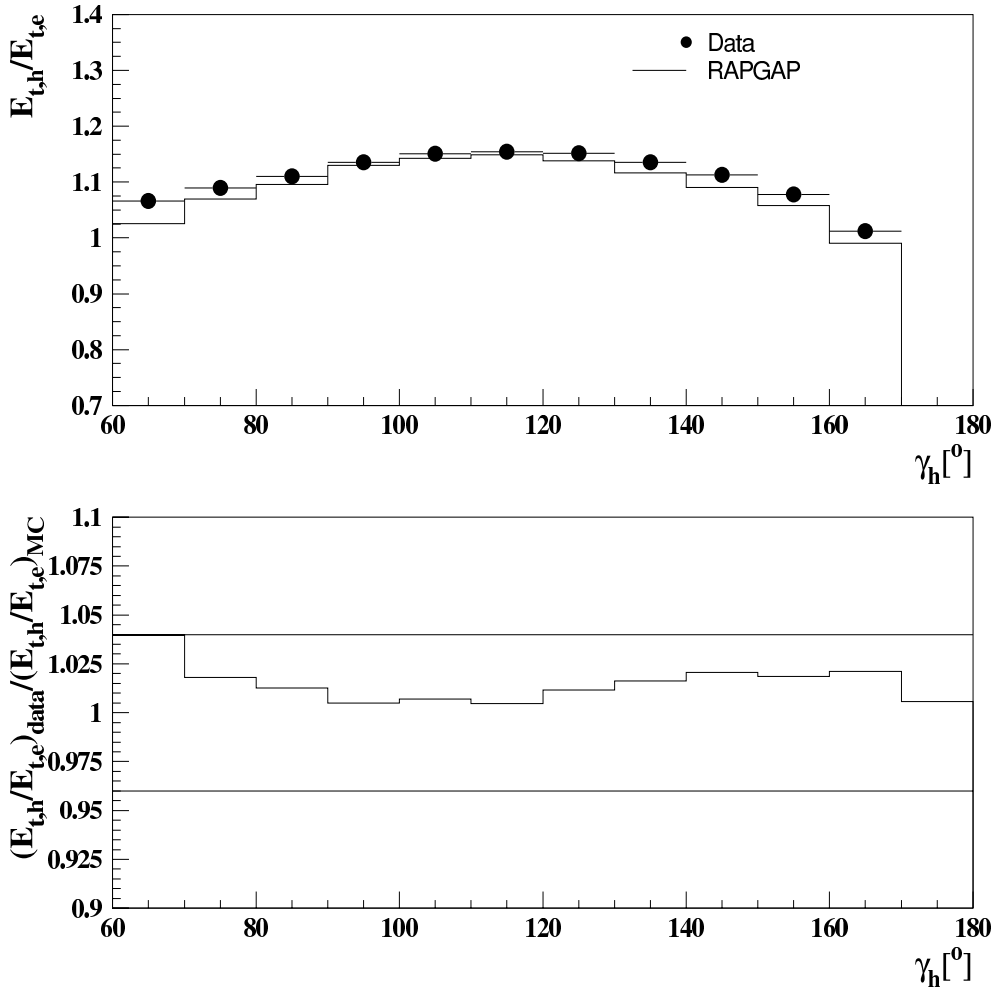

Figure 4.24: E_t balance for measured DIS events (bullets) compared to the E_t balance obtained for simulated DIS events (RAPGAP, full line). The lower part of the figure shows the double ratio built from the E_t balance determined in the measurement and in the simulation.

Error source	Variation	Typical change of rate
Hadronic energy scale (LAr+Tracks)	$\pm 4\%$	10-15%
SpaCal electromagnetic energy scale	$\pm 1\%$	6%
SpaCal hadronic energy scale	$\pm 7\%$	2%
Angular uncertainty (BDC)	± 1 mrad	2%
γp-background	$\pm 30\%$	4-7%
model uncertainty	-	5%

Table 4.10: Overview on the influence of the different contributions to the systematic error.

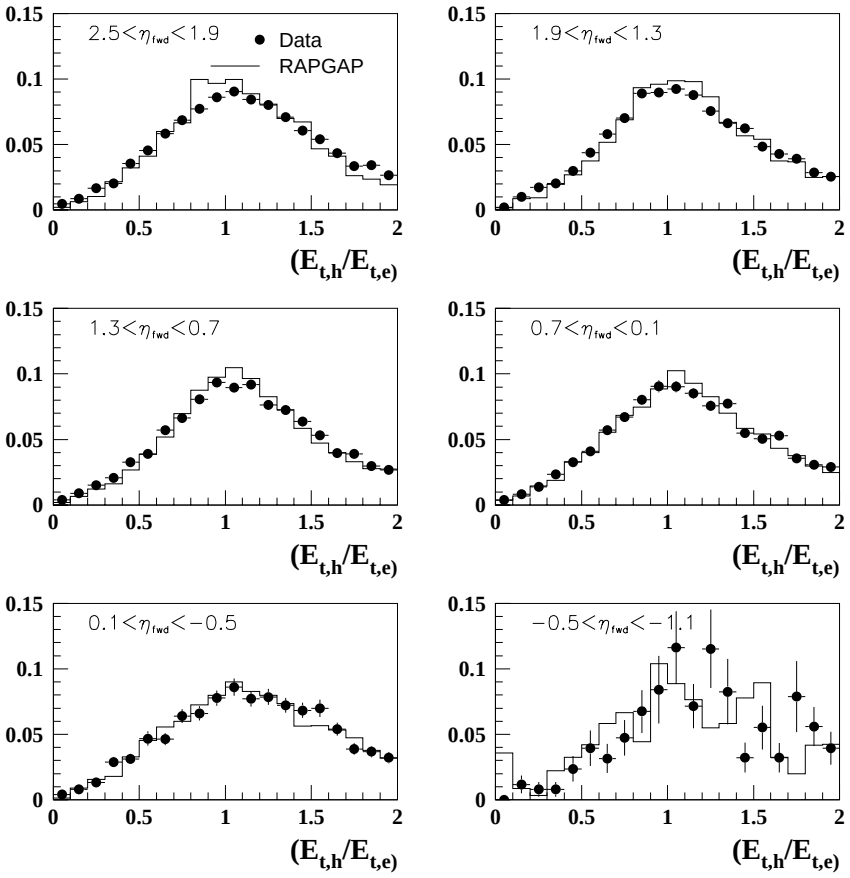

Figure 4.25: Transverse momentum balance spectrum for dijet events in bins of the η_{lab} position of the most forward detected jet η_{fwd}. The measured E_t balance (points) is compared to the E_t balance of simulated events (RAPGAP, full line).

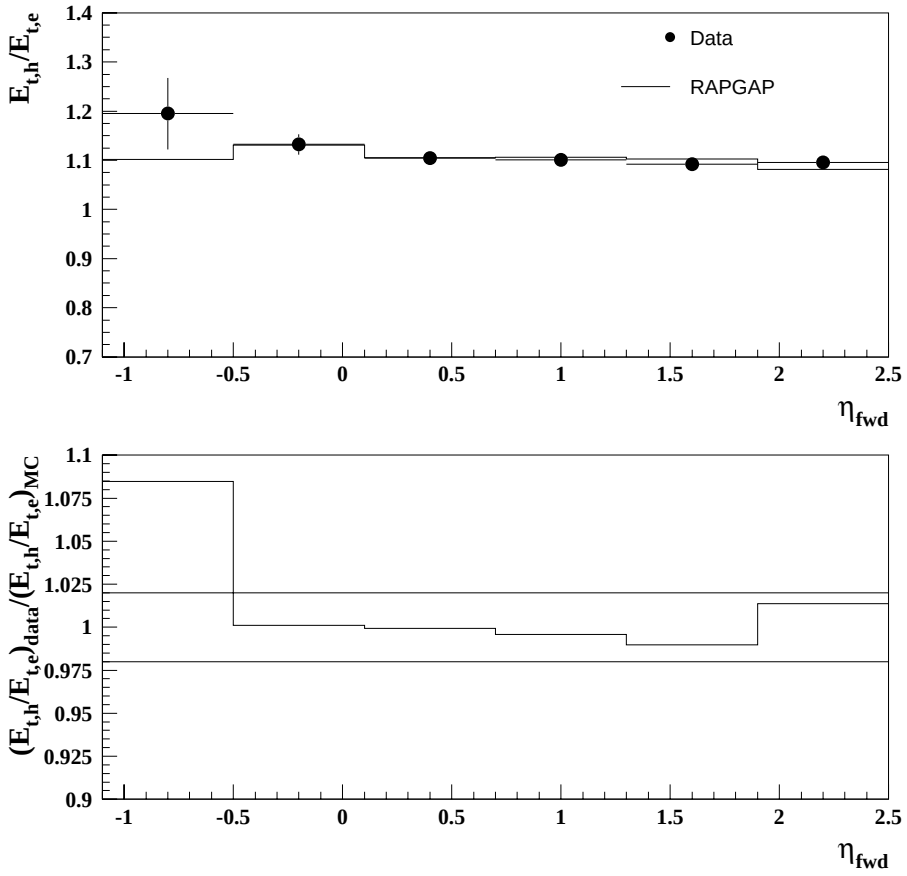

Figure 4.26: Measured E_t balance for measured dijet events (points) compared to the E_t balance as obtained for simulated events (RAPGAP, full line) as a function of the pseudo-rapidity of the most forward jet, η_{fwd}. The lower part shows the double ratio built from the measured and simulated E_t balance.

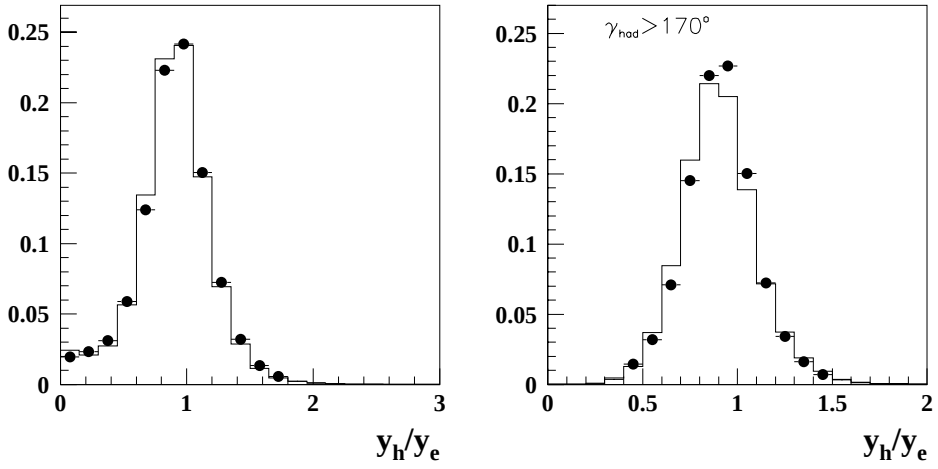

Figure 4.27: y balance, y_h/y_e for inclusive DIS events. The right plot shows the y balance for events where the direction of the struck points to the backward region.

4.5 Results

The final values of the dijet rate R_2 ($R_2(x_B)$ and $R_2(Q^2)$, respectively) as obtained in this measurement are summarized in Tables 4.11 to 4.13 together with their statistical and systematic errors The statistical error combines effects from the number of data, the corrections factors as well as from the subtraction of γp background. The statistical error is always significantly smaller than the systematic error.

kinematic range	$(R_2(\Delta/\text{GeV}) \pm \sigma_{stat.} \pm \sigma_{sys.})/10^{-3}$		
x_B	$\Delta = 0$	$\Delta = 2$	$\Delta = 7$
$10^{-4} < x_B < 2.5\,10^{-4}$	$34.7 \pm 0.7^{+3.6}_{-3.8}$	$24.8 \pm 0.6^{+2.5}_{-2.7}$	$5.1 \pm 0.2^{+0.9}_{-0.7}$
$2.5\,10^{-4} < x_B < 5\,10^{-4}$	$31.6 \pm 0.5^{+3.4}_{-3.3}$	$22.5 \pm 0.4^{+2.3}_{-2.4}$	$4.4 \pm 0.1^{+0.7}_{-0.6}$
$5\,10^{-4} < x_B < 10^{-3}$	$34.3 \pm 0.5^{+3.5}_{-3.6}$	$23.6 \pm 0.4^{+2.6}_{-2.4}$	$4.6 \pm 0.1^{+0.7}_{-0.7}$
$10^{-3} < x_B < 2.5\,10^{-3}$	$47.6 \pm 0.7^{+5.0}_{-4.6}$	$33.2 \pm 0.5^{+3.5}_{-3.2}$	$6.9 \pm 0.2^{+1.0}_{-1.1}$
$2.5\,10^{-3} < x_B < 5\,10^{-3}$	$63.7 \pm 1.5^{+5.6}_{-5.9}$	$56.0 \pm 1.3^{+5.2}_{-5.1}$	$7.8 \pm 0.4^{+1.2}_{-1.3}$
$5\,10^{-3} < x_B < 10^{-2}$	$71.7 \pm 2.8^{+7.1}_{-6.6}$	$48.4 \pm 2.1^{+6.1}_{-5.9}$	$9.2 \pm 0.8^{+1.4}_{-1.7}$

Table 4.11: Corrected dijet rates in bins of x_B together with the statistical ($\sigma_{stat.}$) and their systematic errors ($\sigma_{sys.}$).

The corrected single differential R_2 distributions are shown in Figure 4.28 as a function of x_B and Q^2. The figure includes the R_2 for three values of the variable Δ. For $\Delta = 0$ R_2 lies between 3% and 9% while in the case $\Delta = 7$ GeV less than 1% of the DIS events can be identified as dijet events. The plots show further that R_2, increases with increasing x_B as well as for increasing Q^2.

The double differential measurement of R_2 is presented in Figure 4.29 for the central cut scenario with $\Delta = 2$. It can be observed that the dependence of the dijet rate on x_B is entirely different than the shape observed in the single differential measurement of R_2. For fixed Q^2 the

Kinematic range	$(R_2(\Delta/\text{GeV}) \pm \sigma_{stat.} \pm \sigma_{sys.})/10^{-3}$		
Q^2/GeV^2	$\Delta = 0$	$\Delta = 2$	$\Delta = 7$
$5 < Q^2 < 11$	$27.7 \pm 0.3^{+3.3}_{-3.2}$	$18.7 \pm 0.2^{+2.1}_{-2.1}$	$3.4 \pm 0.1^{+0.6}_{-0.5}$
$11 < Q^2 < 15$	$34.3 \pm 0.5^{+3.8}_{-3.7}$	$24.0 \pm 0.4^{+2.6}_{-2.7}$	$4.5 \pm 0.1^{+0.8}_{-0.7}$
$15 < Q^2 < 20$	$42.4 \pm 1.8^{+5.0}_{-4.3}$	$30.0 \pm 0.5^{+3.3}_{-3.3}$	$5.7 \pm 0.1^{+0.9}_{-0.8}$
$20 < Q^2 < 30$	$49.3 \pm 0.6^{+4.3}_{-4.7}$	$34.4 \pm 0.5^{+3.3}_{-3.3}$	$7.4 \pm 0.2^{+1.1}_{-1.1}$
$30 < Q^2 < 50$	$65.5 \pm 0.7^{+5.6}_{-5.6}$	$47.9 \pm 0.6^{+4.3}_{-4.1}$	$11.1 \pm 0.2^{+1.4}_{-1.4}$
$50 < Q^2 < 100$	$84.6 \pm 0.9^{+7.2}_{-6.8}$	$60.8 \pm 0.7^{+5.5}_{-5.0}$	$13.1 \pm 0.3^{+1.6}_{-1.7}$

Table 4.12: Corrected dijet rate in bins of Q^2 together with the statistical ($\sigma_{stat.}$) and systematic errors ($\sigma_{sys.}$).

Kinematic range		$(R_2(\Delta/\text{GeV}) \pm \sigma_{stat} \pm \sigma_{sys})/10^{-3}$				
Q^2/GeV^2	$x_B/10^{-4}$	$\Delta = 0$	$\Delta = 1$	$\Delta = 2$	$\Delta = 4$	$\Delta = 7$
$5 - 11$	$1 - 1.7$	$35.3 \pm 1.2^{+3.1}_{-3.8}$	$32.1 \pm 1.1^{+2.8}_{-3.2}$	$26.0 \pm 0.9^{+2.3}_{-2.9}$	$14.0 \pm 0.6^{+1.9}_{-1.7}$	$5.6 \pm 0.3^{+1.0}_{-0.9}$
	$1.7 - 3$	$32.6 \pm 0.8^{+3.9}_{-3.7}$	$28.8 \pm 0.8^{+3.2}_{-3.2}$	$22.1 \pm 0.6^{+2.5}_{-2.3}$	$12.0 \pm 0.4^{+1.5}_{-1.4}$	$4.0 \pm 0.2^{+0.8}_{-0.5}$
	$3 - 5$	$24.4 \pm 0.4^{+3.2}_{-3.0}$	$21.2 \pm 0.7^{+2.8}_{-2.4}$	$16.1 \pm 0.6^{+1.9}_{-1.9}$	$7.9 \pm 0.3^{+1.1}_{-1.1}$	$2.7 \pm 0.2^{+0.5}_{-0.5}$
	$5 - 13$	$19.1 \pm 0.7^{+2.6}_{-2.7}$	$16.3 \pm 0.6^{+2.5}_{-2.1}$	$11.9 \pm 0.3^{+1.9}_{-1.6}$	$5.3 \pm 0.3^{+0.9}_{-0.8}$	$1.7 \pm 0.1^{+0.3}_{-0.3}$
$11 - 15$	$1.7 - 3$	$42.1 \pm 2.4^{+5.0}_{-4.0}$	$39.9 \pm 2.2^{+3.7}_{-4.0}$	$34.5 \pm 1.9^{+3.3}_{-3.5}$	$21.3 \pm 1.3^{+2.7}_{-3.0}$	$8.8 \pm 0.7^{+1.4}_{-1.2}$
	$3 - 5$	$39.7 \pm 1.4^{+4.1}_{-4.2}$	$35.6 \pm 1.3^{+3.7}_{-4.1}$	$28.4 \pm 1.2^{+3.0}_{-3.1}$	$14.0 \pm 0.7^{+2.1}_{-1.9}$	$4.8 \pm 0.3^{+1.1}_{-0.8}$
	$5 - 10$	$32.4 \pm 1.2^{+3.9}_{-3.7}$	$28.1 \pm 1.0^{+3.0}_{-3.3}$	$21.0 \pm 0.8^{+2.6}_{-2.8}$	$10.6 \pm 0.5^{+1.6}_{-1.7}$	$3.6 \pm 0.3^{+0.6}_{-0.8}$
	$10 - 18$	$23.2 \pm 1.4^{+2.9}_{-3.1}$	$19.9 \pm 1.2^{+2.4}_{-2.5}$	$14.6 \pm 1.0^{+2.2}_{-1.9}$	$6.5 \pm 0.5^{+1.1}_{-0.9}$	$2.2 \pm 0.3^{+0.3}_{-0.5}$
$15 - 20$	$2.4 - 5$	$47.4 \pm 1.8^{+5.0}_{-4.3}$	$44.5 \pm 1.8^{+4.6}_{-4.3}$	$37.3 \pm 1.4^{+3.4}_{-3.8}$	$23.0 \pm 1.1^{+3.3}_{-3.0}$	$9.3 \pm 0.6^{+1.3}_{-1.5}$
	$5 - 10$	$48.3 \pm 1.7^{+5.7}_{-5.4}$	$41.5 \pm 1.5^{+4.5}_{-4.7}$	$32.2 \pm 1.3^{+3.7}_{-3.6}$	$15.4 \pm 0.7^{+2.7}_{-1.9}$	$5.1 \pm 0.4^{+1.0}_{-0.8}$
	$10 - 22$	$30.9 \pm 1.4^{+4.2}_{-3.6}$	$27.3 \pm 1.3^{+3.5}_{-3.2}$	$21.0 \pm 1.1^{+2.7}_{-2.8}$	$11.1 \pm 0.7^{+1.5}_{-2.0}$	$3.5 \pm 0.3^{+0.6}_{-0.8}$
$20 - 30$	$3 - 5$	$56.2 \pm 2.7^{+2.1}_{-5.3}$	$53.0 \pm 2.7^{+4.0}_{-4.5}$	$46.6 \pm 2.5^{+3.7}_{-4.0}$	$29.6 \pm 1.9^{+1.7}_{-3.1}$	$12.7 \pm 1.1^{+1.4}_{-1.5}$
	$5 - 10$	$57.0 \pm 1.6^{+4.8}_{-5.1}$	$52.1 \pm 1.5^{+4.9}_{-5.0}$	$41.2 \pm 1.3^{+3.6}_{-3.6}$	$23.9 \pm 0.9^{+2.4}_{-2.5}$	$8.9 \pm 0.5^{+1.5}_{-1.3}$
	$10 - 33$	$41.9 \pm 1.2^{+4.6}_{-4.5}$	$36.7 \pm 1.1^{+4.3}_{-4.2}$	$26.9 \pm 0.9^{+2.9}_{-3.2}$	$13.4 \pm 0.5^{+1.7}_{-1.7}$	$5.1 \pm 0.3^{+0.9}_{-1.0}$
$30 - 50$	$5 - 10$	$73.4 \pm 2.6^{+5.1}_{-6.5}$	$68.0 \pm 2.5^{+5.0}_{-5.7}$	$58.6 \pm 2.0^{+4.6}_{-4.4}$	$35.7 \pm 1.5^{+2.8}_{-3.1}$	$16.8 \pm 1.0^{+1.2}_{-1.7}$
	$10 - 55$	$62.8 \pm 1.3^{+6.0}_{-5.5}$	$56.0 \pm 1.2^{+5.4}_{-4.9}$	$44.3 \pm 1.0^{+4.3}_{-4.1}$	$23.8 \pm 0.7^{+2.9}_{-2.9}$	$9.2 \pm 0.4^{+1.5}_{-1.4}$
$50 - 100$	$8 - 25$	$94.3 \pm 2.7^{+9.0}_{-7.2}$	$86.3 \pm 2.6^{+8.1}_{-6.6}$	$71.2 \pm 2.3^{+5.8}_{-4.8}$	$44.2 \pm 1.7^{+4.5}_{-3.8}$	$17.7 \pm 1.0^{+2.0}_{-2.0}$
	$25 - 100$	$79.5 \pm 1.9^{+6.5}_{-6.9}$	$71.7 \pm 1.8^{+6.2}_{-6.6}$	$55.4 \pm 1.5^{+5.5}_{-5.4}$	$29.2 \pm 1.0^{+3.6}_{-3.8}$	$10.7 \pm 0.5^{+1.4}_{-1.6}$

Table 4.13: Corrected dijet rate R_2 including the statistical and systematic errors for various Q^2,in GeV^2, ranges as a function of x_B, divided by 10^{-4}.

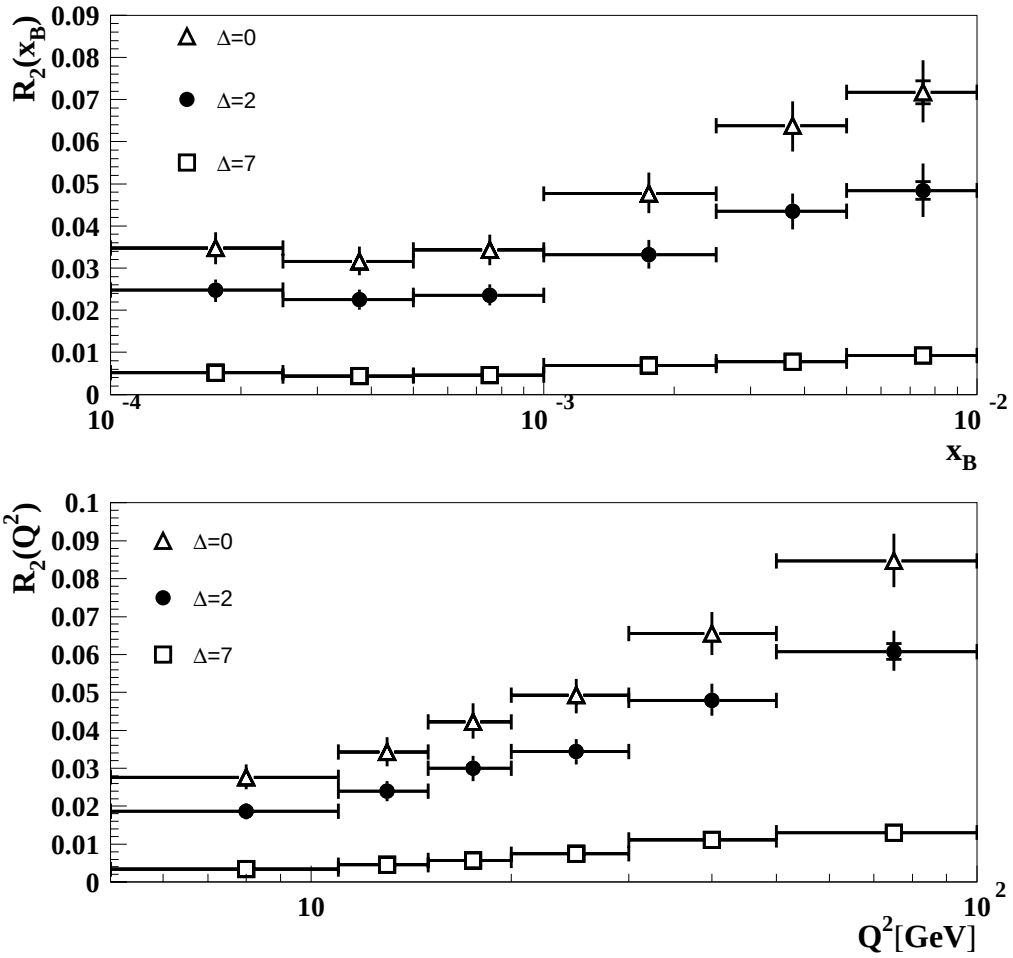

Figure 4.28: Corrected R_2 as a function of x_B and Q^2 for three different choices of the variable Δ. The inner errors bars are the statistical errors and the outer error bars reflects the sum of the statistical and systematic error added in quadrature.

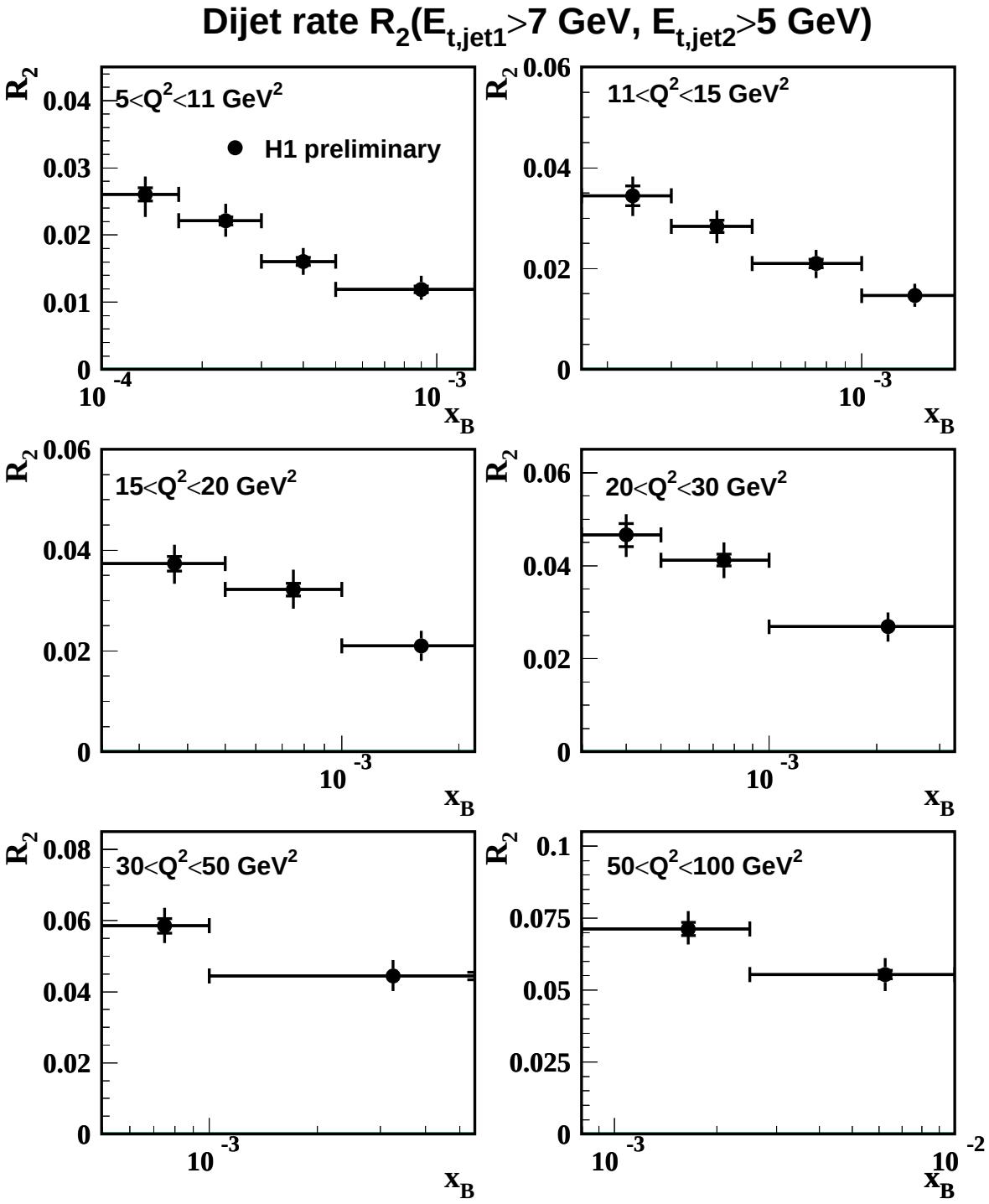

Figure 4.29: The corrected dijet rate as a function of x_B in bins of Q^2 for the $\Delta = 2$ scenario. The error bars reflect the statistical and systematic errors added quadrature.

amount of dijet events relatively to the total ep cross section increases with decreasing x_B. In the lowest Q^2 bin the dijet rate increases by more than a factor of two. Part of this increase can be explained by Equation 1.34. For dijet production the parton-γ^* center-of-mass energy $\hat{s}$ has to be considerably large. For fixed Q^2 a sufficient amount of $\hat{s}$ needed for jet production can only be obtained if $x_p = x_B/\xi$ is very small which is more likely to occur at low x_B. It is now interesting to investigate to which extent theoretical models are able to predict the slope of the increase towards low x_B. This question will be addressed in the next chapter. In Figure 4.30 the measured dijet rate is shown in different bins of x_B and Q^2 as a function of Δ. As expected the

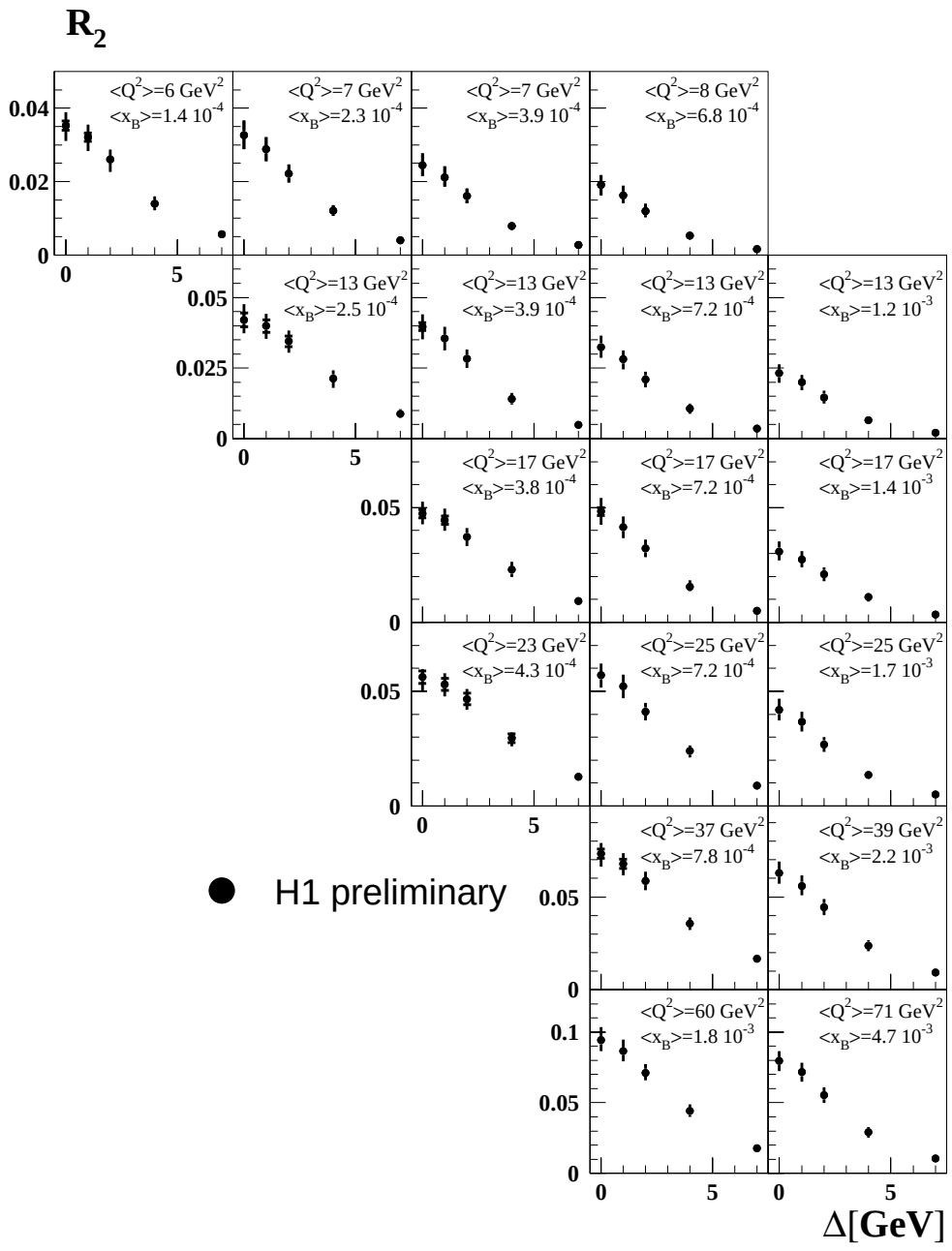

Figure 4.30: R_2 in bins of x_B and Q^2 as a function of the NLO threshold parameter Δ.

dijet rate drops in all bins with increasing Δ. These distributions will be discussed further in Chapter 5.

4.5.1 Comparison to an Earlier Measurement

As a cross check, the analysis presented in [H1C98] has been repeated for the new data set analyzed in this thesis. For the sake of comparison, the cuts and jet definitions used in this analysis were modified such that they meet the cuts used in the previous analysis.

For the positron selection, the following kinematic cuts are applied:

$$E_e^{'} > 11\,\mathrm{GeV}$$

$$y_e > 0.05$$

$$156^o < \theta_e < 173^o$$

The jets are defined by the CDF Cone Algorithm [CDF92] in the hadronic center-of-mass frame with the following settings:

$$R = 1$$

$$f_{ovlim} = 0.75$$

$$E_t^* > 5\,\mathrm{GeV}$$

Exactly two jets have to meet these requirements. The analysis has been restricted to distances $|\Delta\eta^*| < 2$ between the two identified jets. For the correction of the data for detector effects and radiative effects RAPGAP has been used. The results for $\Delta = 2\,\mathrm{GeV}$ are shown in Figure 4.31

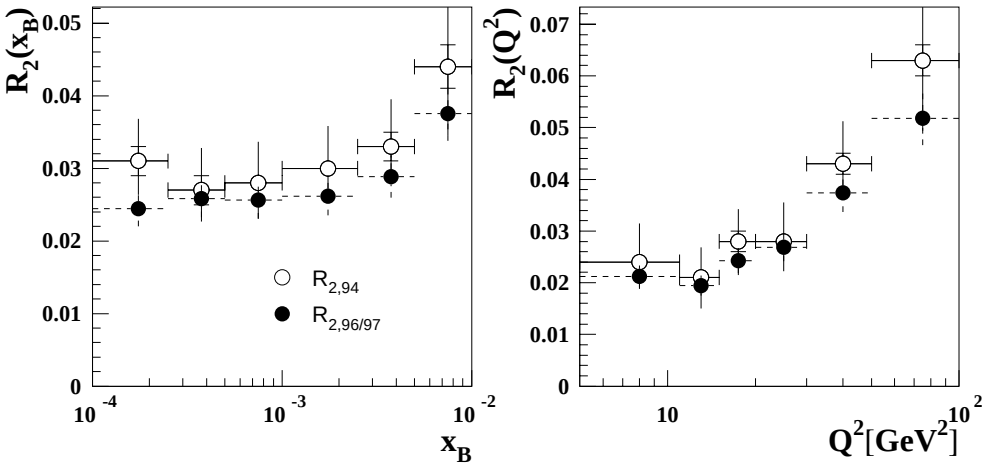

Figure 4.31: Comparison between R_2 as measured by the H1 collaboration using 94 data the corresponding measurement using 1996/97 data.

and compared to the published R_2 measurement. Both results agree within the systematic errors confirming the results published in [H1C98].

4.6 Final Remarks on Recent Developments

The strong increase of luminosity collected with the H1 detector in the years 1996 and 1997 allowed a refining of the calibration of the hadronic energy energy scale beyond the scope of the methods used previously. In order to improve the precision of the measurement of the inclusive proton structure function F_2, the LAr calorimeter has been re-calibrated using the E_t balance between the hadronic system and the scattered positron. For the calibration, an iterative method has been used which was originally invented for the fine tuning of the electromagnetic energy scale of the backward SpaCal calorimeter (see [GLA98], [HEI99] and [ARK99]).

Recently, the H1 collaboration has reported and published two measurements of the inclusive structure function F_2. One of these covers the kinematic region above $Q^2 > 100\,\mathrm{GeV}$ [H1C99] while the other exploits the region of small Q^2 [KLE99]. For these two analysis the estimated uncertainty in the hadronic energy scale is only 2%, see also [NAU99]. For the two measurements, different sets of calibration factors have been developed. Since the latter analysis was performed in a phase space region covered also by this analysis this set of calibration factors will be tested here in order to estimate the improvement concerning the precision of the hadronic energy scale.

In addition to the derivation of updated calibration factors, the inclusion of tracks into the hadronic final state has been revised. Well measured central tracks are extrapolated to the calorimeter surface. Subsequently, the energy in a cylinder with a radius of 25 cm in the electromagnetic section of the H1 LAr calorimeter and 50 cm in its hadronic section is summed up. If the energy in the cylinder in the electromagnetic part is lower than the track momentum this energy is neglected in the total sum of hadronic energy, otherwise the calorimetric energy is used. Further details to this procedure can be found in [MAR98] and [HEI99].

Figure 4.32 shows the E_t balance for inclusive DIS events measured in the data taking period 1996 when the previously mentioned calibration and the explained technique to combine tracking and calorimeter information have been applied. The figure demonstrates that the agreement between data and the Monte Carlo simulation is indeed better than 2% in the accessible phase space region for the present analysis. However, it has to be investigated further whether this precision will also hold for more exclusive measurements like the determination of dijet cross Sections.

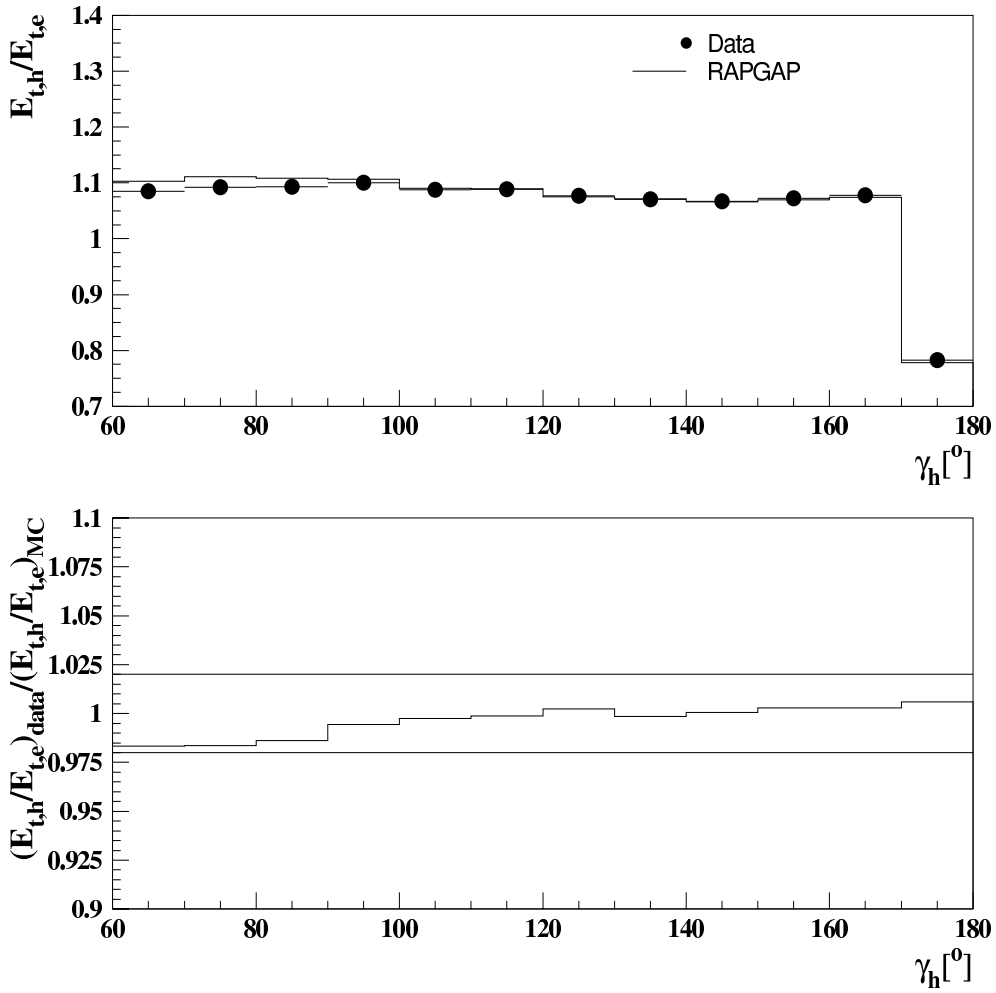

Figure 4.32: E_t balance for inclusive DIS events as observed in the measurement and for simulated DIS events. In contrast to the results shown in Figure 4.24 the results here are based on the treatment of the hadronic final state objects as described in Section 4.6.

Chapter 5

Comparison of the Data to NLO QCD calculations

If QCD in next-to-leading order (NLO) is employed to confront theory with measurement, the dependence of the theoretical prediction on the choice of the renormalization scale μ_r^2 is expected to be small. However, the correct choice of μ_r^2 remains a matter of concern especially at low x_B and low Q^2 where higher orders in the perturbation series might be of more importance. For the study of dijet events in DIS, at least two scales are suggested by the nature of the process. The first of which is the four-momentum transfer Q^2 and the other possible scale for jet production is the transverse energy of the outgoing jets. The comparison of the measured dijet rate as presented in the previous chapter with NLO predictions for these different scales is addressed by this chapter.

In general the NLO QCD programs provide the partonic final state after the calculation of the cross section. For NLO QCD calculations no consistent prescription to fragment the partonic final state into observable hadrons is yet available. Thus, in order to compare the NLO predictions to the measured data it is necessary to estimate the influence of the hadronization corrections. It has been shown in [WOB99] that these hadronization corrections can be estimated based on the predictions from the hadronization model JETSET as implemented in the event generators LEPTO and ARIADNE (CDM model). As an example Figure 5.1 shows for the $\Delta = 2$ scenario the ratio between the dijet rate on hadron level and on parton level for LEPTO and the CDM model. The resulting correction factors are given by the average of both models and are multiplied to the predicted dijet rate. The spread between the two models will be taken as the systematic error of the hadronization correction.

First the corrected dijet rates are compared to predictions of analytical NLO QCD calculations using the DISENT program; the form of the presentation of the NLO predictions is illustrated in Figure 5.2. The comparison between the data and DISENT predictions for the $\Delta = 2$ scenario is shown in Figure 5.3 with two choices of the renormalization scale μ_r^2. The factorization scale μ_f^2 is always set to Q^2.

With the choice $\mu_r^2 = Q^2$, the NLO QCD calculation is able to describe the data in the entire analyzed phase space. However, the scale uncertainty, estimated by varying μ_r^2 by a factor of two up and down, is large for this choice of μ_r^2 resulting in an error on the prediction of around 30%. This indicates that the NLO calculation is not stable necessitating the inclusion of higher order contributions. However, concerning jet physics there exists a second hard scale given by the transverse energy E_t of the outgoing jets and providing a more natural choice for the renormalization scale. Here a combination of both Q^2 and E_t^2 , i.e. $\mu_r^2 = Q^2 + E_t^2$, is chosen to compare the measured data to the theoretical predictions as proposed in [KRA98]. This choice has been made in order to be consistent with the choice of μ_r^2 used for later studies with JETVIP (see below). It has, however, been checked that the results for the choices $\mu_r^2 = E_t^2$ and $\mu_r^2 = Q^2 + E_t^2$ agree within 10%. As can be seen from Figure 5.3, the NLO prediction is able to describe the data in the largest x_B bins for all Q^2 ranges while it cannot follow the slope of

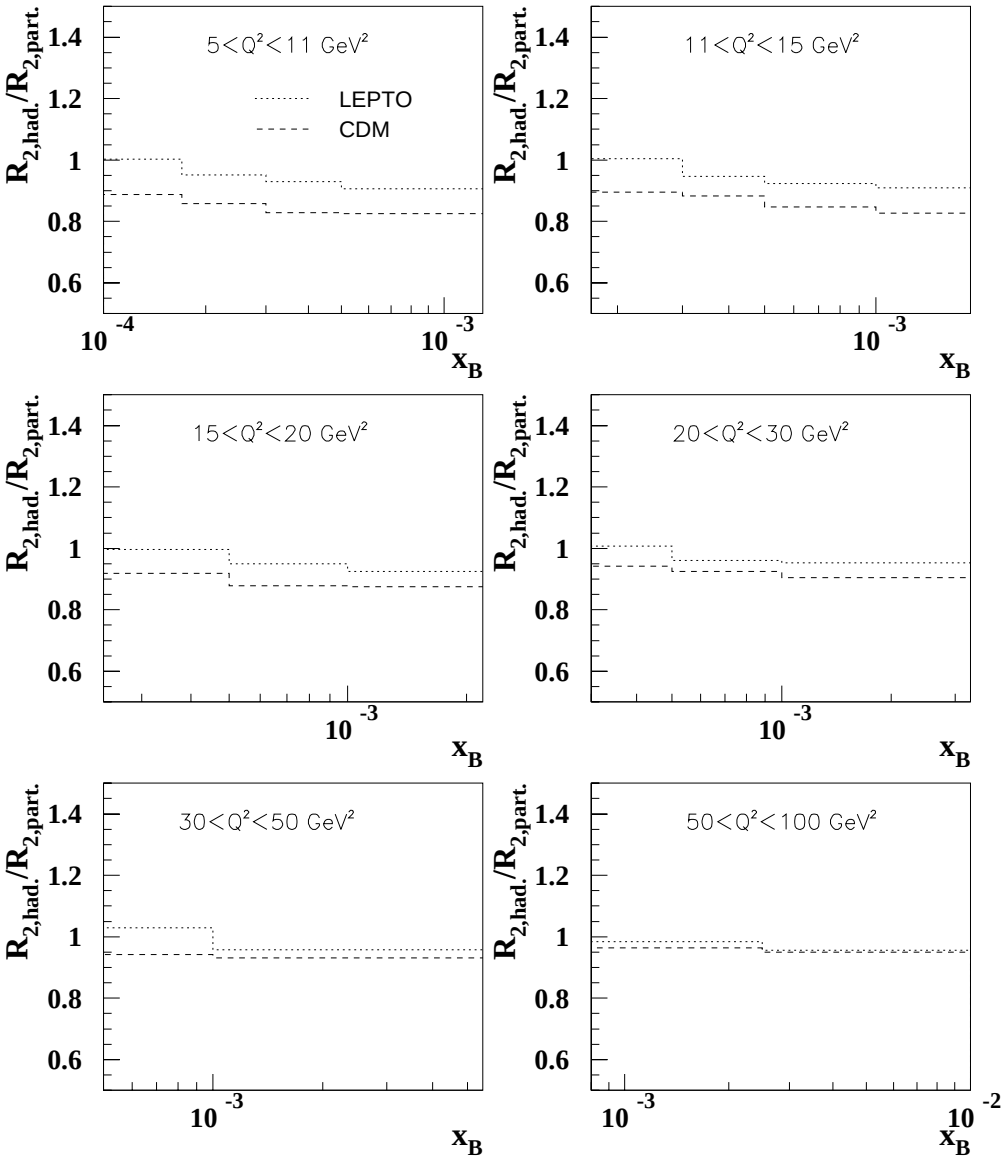

Figure 5.1: Ratio of the dijet rate on the hadron- and on the parton level for the double differential measurement of R_2 as a function of x_B.

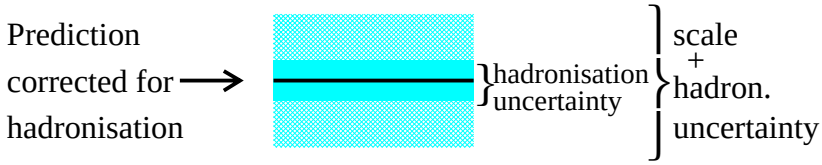

Figure 5.2: Explanation for the presentation of the NLO predictions. The black line represents the NLO predictions corrected for hadronization effects. The full error band represents the uncertainty of the hadronization corrections. The hatched error band represents the hadronization uncertainty and the renormalization scale uncertainty added in quadrature.

the data towards low x_B. However, the scale uncertainties are much smaller for this choice of μ_r^2 and the results should therefore have more predictive power. This leaves room for introducing additional contributions to dijet production like graphs where the photon acts as a source of partons (virtual photon structure) or like a different evolution of the parton density function (BFKL dynamics).

Hence, the data are compared to calculations using the JETVIP program. As with DISENT it offers the possibility to calculate dijet cross sections in NLO QCD for the direct coupling of the virtual γ. In addition JETVIP allows the inclusion of resolved contributions where the photon interacts hadronically by fluctuating into partons which take part in the hard subprocess. In order to avoid double counting in the full NLO QCD calculation, it is necessary to subtract the contribution from the virtual photon splitting ($\gamma^* \to q\bar{q}$) where one of the quarks subsequently interacts with the partons from the photon to produce two high E_t jets. This process is already included in the parameterization of the virtual photon structure function SAS-1D which is used for the following studies. This perturbatively calculated contribution will be named 'splitting' and the contribution from the resolved virtual photon will be called 'resolved'.

Before the comparison between the data and the prediction from JETVIP are performed, a few further comments to the usage of JETVIP have to be made. Partons from the photon side propagate with a fraction $x_\gamma Q$ of the photon momentum into the hard interaction. Therefore their invariant mass squared can be calculated to be $\mathrm{m}^2 = (x_\gamma Q)^2$. The existing parameterizations for the photon structure and the matrix elements for the hard subprocess, however, are based on massless, on-shell partons. Obviously this requirement gets more and more violated with increasing virtuality Q^2 of the photon. The most recent version of JETVIP [POE99] puts the masses of the partons from the photon side artificially to zero in order to be consistent in the calculation. This, however, breaks energy momentum conservation and leads to unphysical predictions of the program if Q^2 becomes too large. It should be noted, that JETVIP originally was not designed for Q^2 above $20\,\mathrm{GeV}^2$ and it is still in discussion whether the concept of a virtual photon structure is valid for large virtualities of the photon.

As an alternative JETVIP, can be set up such that the partons carry their mass into the hard subprocess (massive scheme). This is inconsistent with the use of massless matrix elements and massless parton evolutions of the photon. It is also expected that the predictions based on the massive scheme depend on the phase space slicing parameter y_{cut}, which is not the case if the partons from the photon [POE00] are on-shell (massless scheme). Since the predictions depend now on the phase space slicing parameter they are more a model than a full prediction.

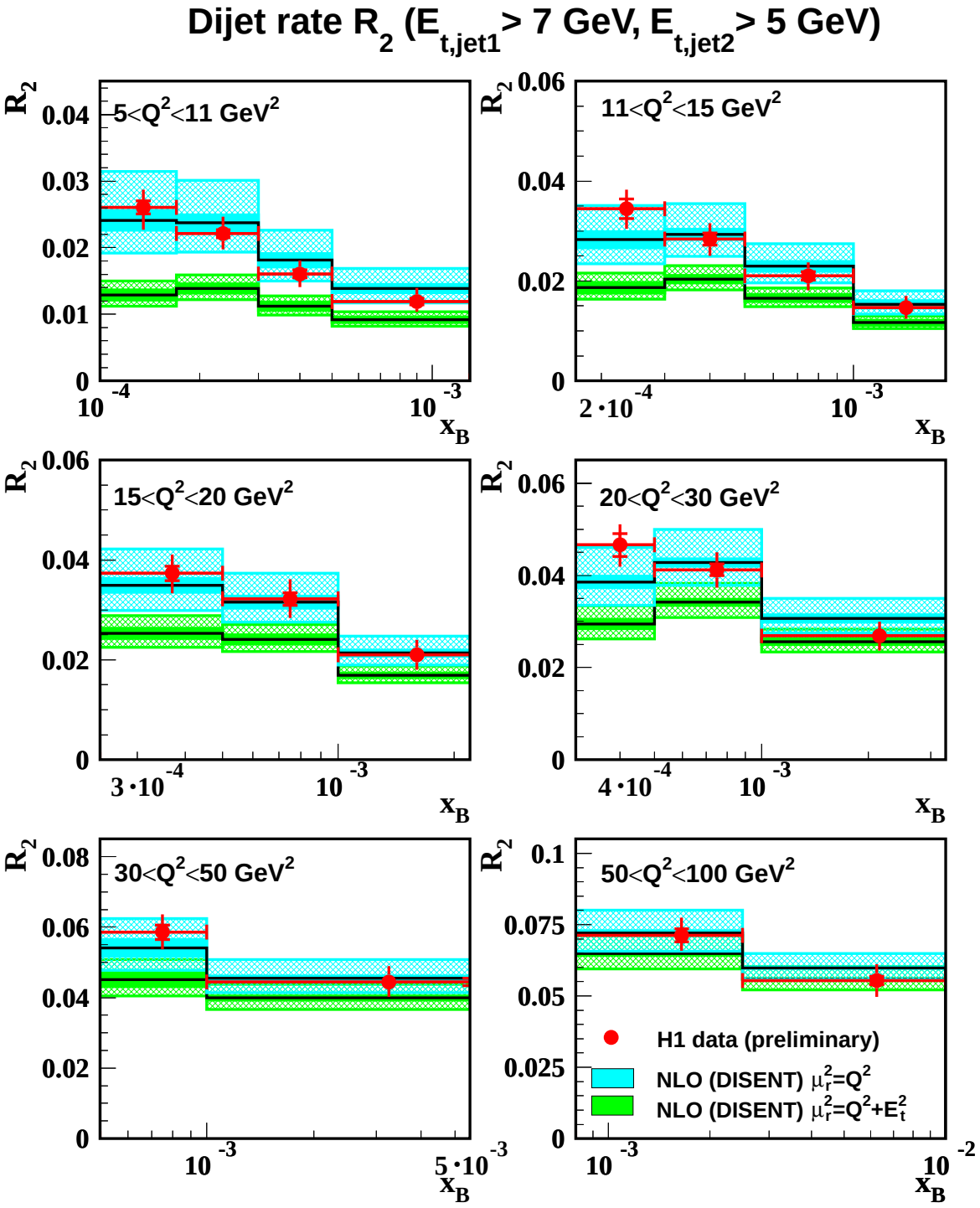

Figure 5.3: Corrected dijet rate R_2 as a function of x_B in bins of Q^2. Shown are the NLO QCD predictions, corrected for hadronization effects, for $\mu_r^2 = Q^2$ and for $\mu_r^2 = Q^2 + E_t^2$.

In Figure 5.4 R_2, is compared to predictions from the JETVIP program using $\mu_r^2 = \mu_f^2 = Q^2 + E_t^2$ in order to have a smooth behavior of the predictions even in the case $E_t^2 < Q^2$ [KRA98]. Here, only the massive scheme is used since it provides physical predictions over the

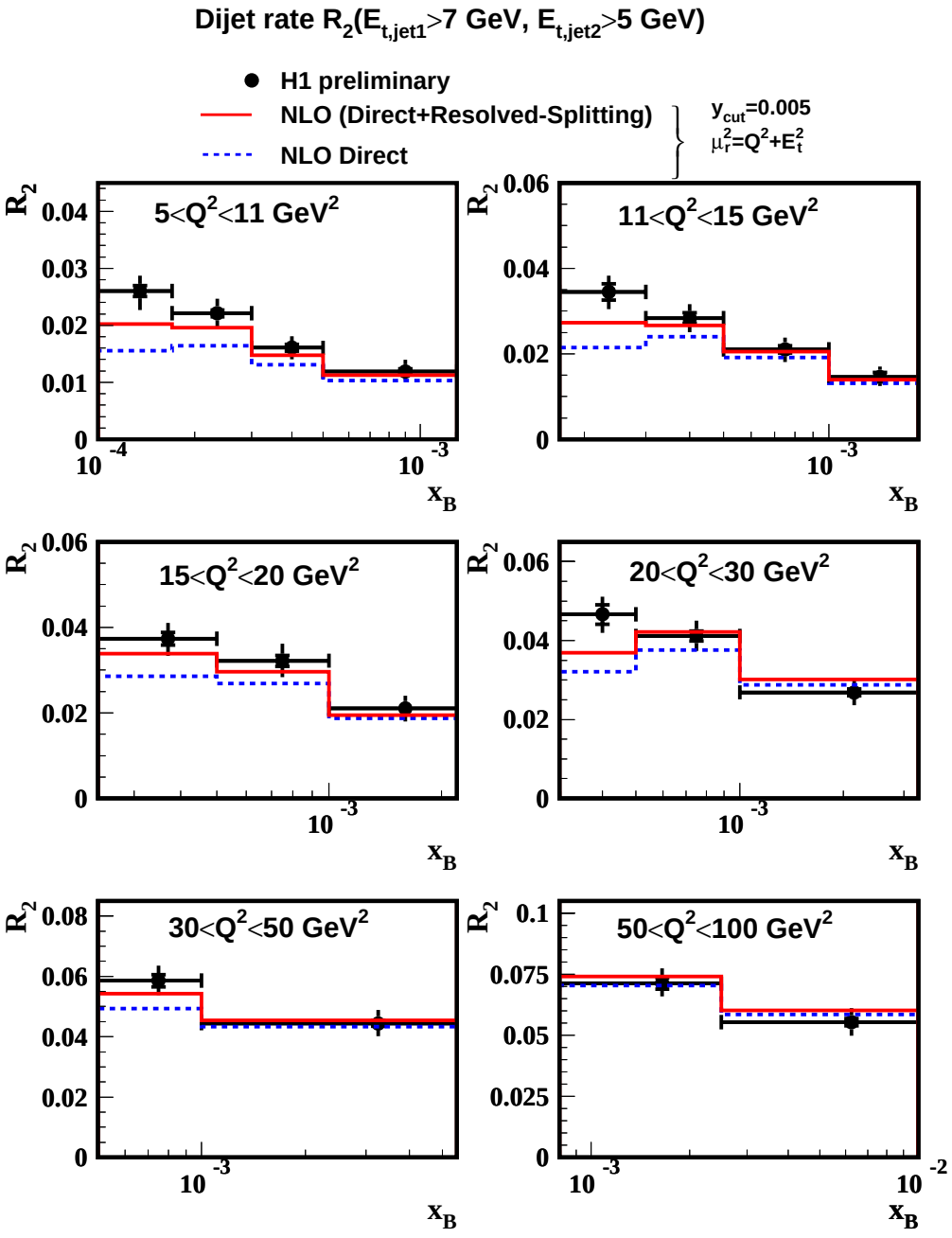

Figure 5.4: Corrected dijet rate R_2 compared to NLO predictions (JETVIP) including only a direct coupling of the virtual γ and including contributions from the resolved virtual photon. For the resolved contributions the massive approach was used. The phase space slicing parameter is chosen to be $y_{cut} = 0.005$. The NLO predictions are corrected for hadronization effects.

entire analyzed Q^2 range. However, it was checked that the massless scenario gives quite similar results in the region $Q^2 < 20\,\mathrm{GeV}^2$ where JETVIP is expected to behave well. The y_{cut} parameter

has been set to 0.005 following the recommendation in [POE99]. It can clearly be seen that adding contributions from resolved virtual photon brings the prediction into better agreement with the data than it is the case when only direct contributions are taken into account. This can be taken as a hint that a pure DGLAP approach in the parton ladder is not sufficient to describe the data. Rather other contributions have to be taken into account to describe the production of dijet events using NLO calculations.

As a cross check Figure 5.5 compares the data to JETVIP predictions using $y_{cut} = 0.0005$ to testing the stability of the result. The same conclusion as before may be drawn for this choice of y_{cut} as well although the summed predictions are slightly larger at large Q^2.

To study the dependence of the dijet rate on the transverse energy of the jets, R_2 is measured as a function of the parameter Δ where the highest $E_{t,jet}$ satisfies $E_{t,jet1} > (5 + \Delta)$ GeV. Note that as $\Delta \to 0$ the cuts on the jets become symmetric and the NLO calculations become infrared sensitive. The measured R_2 as a function of Δ is presented in Figure 5.6 for two bins in $Q^2$and x_B. At large x_B, large Q^2 and $\Delta \geq 1$ GeV, thus staying away from the infrared sensitive region of the calculation, the NLO QCD calculations using DISENT describe the data well for both choices of μ_r^2. In the low x_B, Q^2 regime the predictions only describe the data when choosing $\mu_r^2 = Q^2$. For $\mu_r^2 = Q^2 + E_t^2$ a reasonable agreement between the prediction and the measurement is only observed for $\Delta = 7$ GeV which is equivalent to the requirement of large transverse energies of the jets. Finally, it must be noted that the NLO calculations show a turnover between $\Delta = 0$ and $\Delta = 1$ GeV whereas the data continue to increase towards $\Delta = 0$. In this region, resummed calculations are needed but are not yet available.

The two bins shown in Figure 5.6 are part of a detailed scan of the phase space which is presented in Figure 5.7. It is evident that for fixed Q^2 and decreasing x_B the NLO description fails to describe the data when $\mu_r^2 = Q^2 + E_t^2$ and that $\mu_r^2 = Q^2$ is favored by the data.

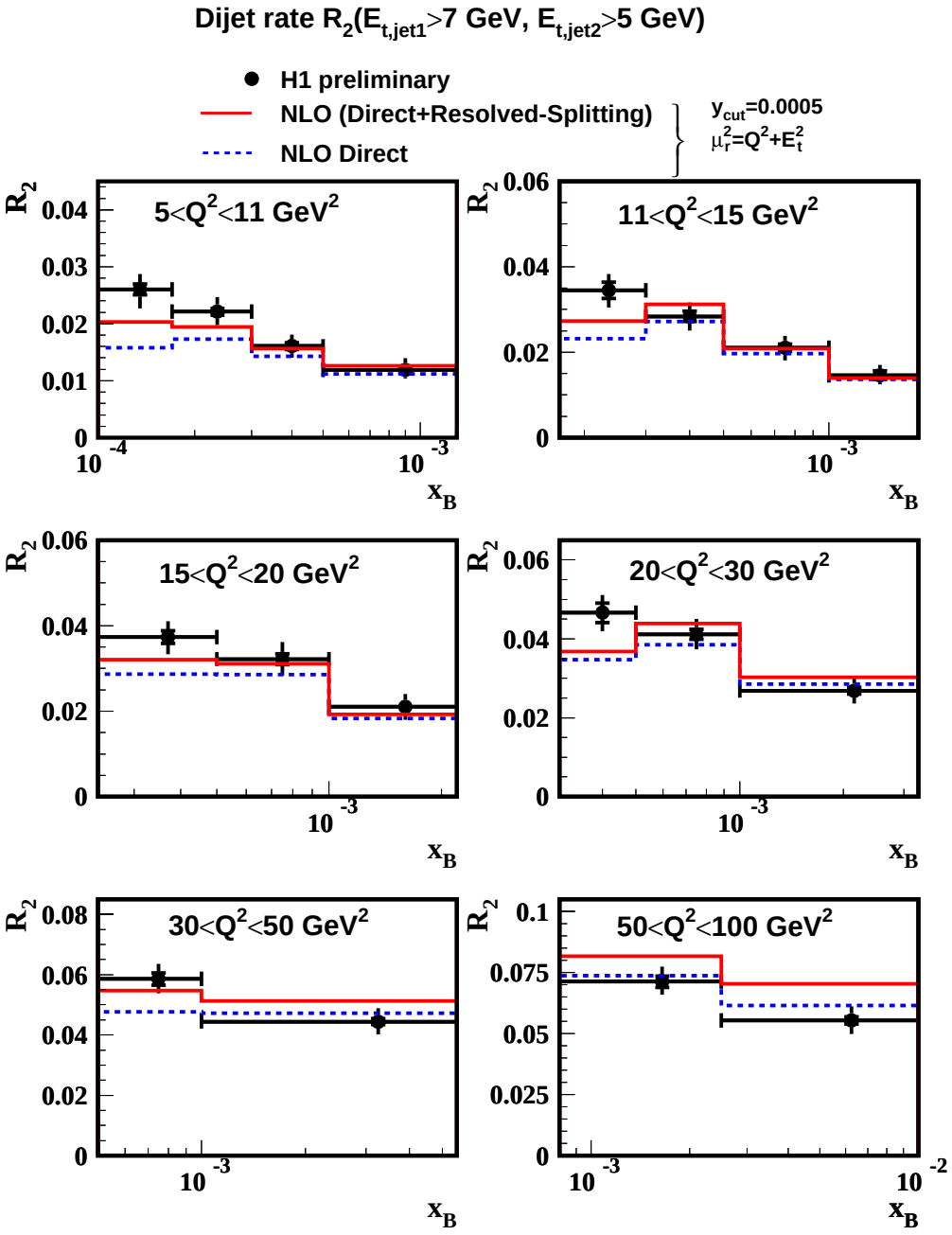

Figure 5.5: Corrected dijet rate R_2 compared to NLO predictions (JETVIP) including only a direct coupling of the virtual γ and including contributions from the resolved virtual photon. For the resolved contributions the massive approach was used. The phase space slicing parameter is chosen to be $y_{cut} = 0.0005$. The NLO QCD predictions are corrected for hadronization effects.

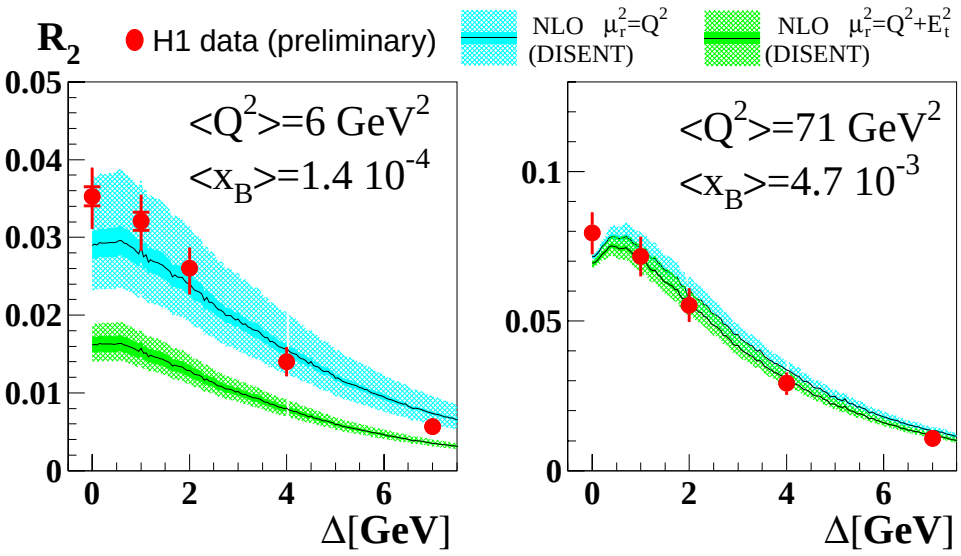

Figure 5.6: Dijet rate R_2 as a function of Δ in two extreme regions of Q^2 and x_B for this analysis. The variable Δ is defined by requiring $E_{t,jet} > (5+\Delta)$ GeV for the jet with the largest transverse energy. The data are compared to NLO predictions for two choices of the renormalization scale μ_r^2. The NLO predictions have been corrected for hadronization effects.

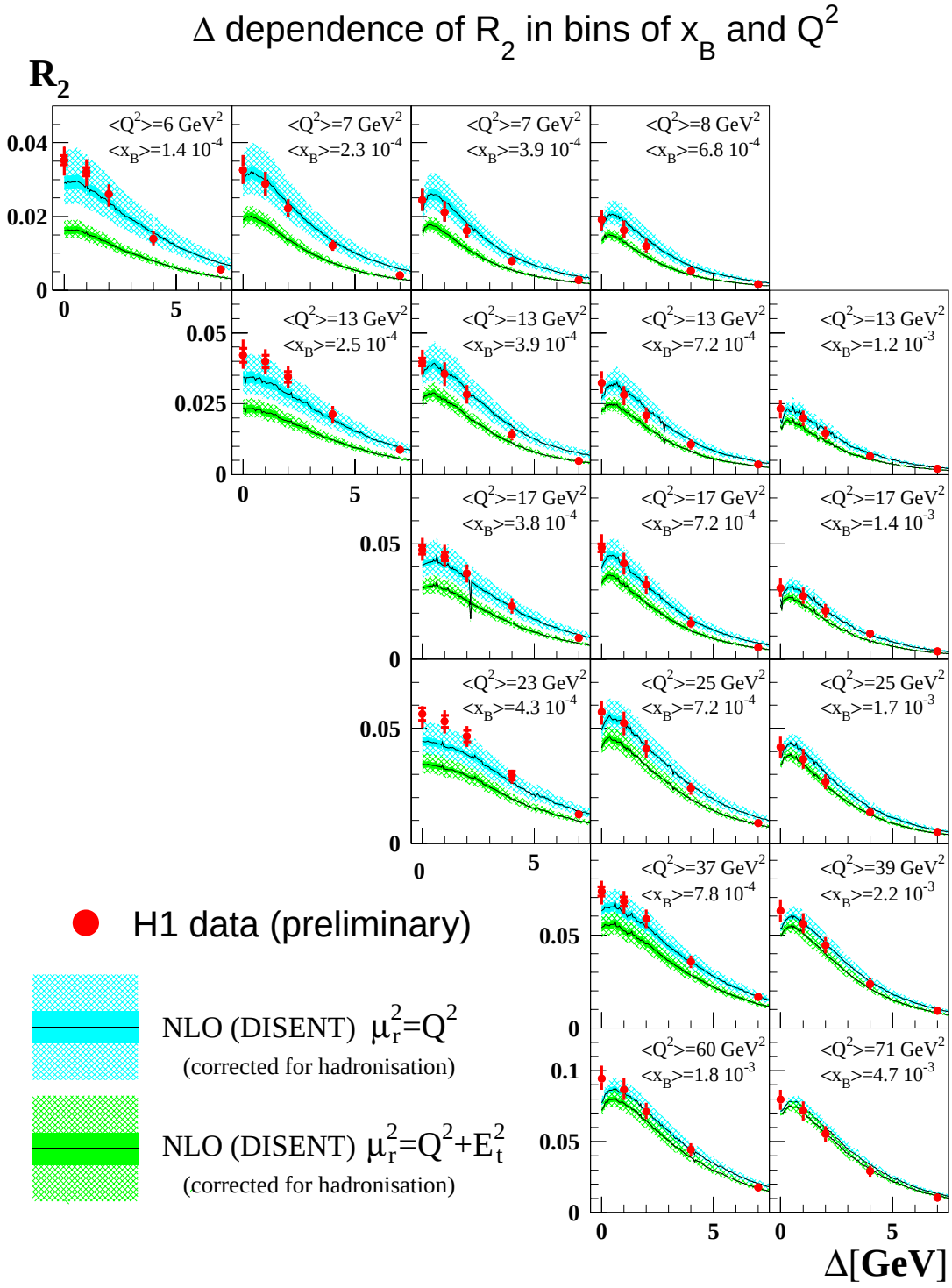

Figure 5.7: Dijet rate R_2 as a function of Δ in various regions of Q^2 and x_B. The two bins shown in Figure 5.6 are included in this figure. The innermost band indicates the the error from the hadronization corrections and the full error band includes the scale uncertainty added in quadrature.

Chapter 6

Summary

The analysis presented the measurement of the dijet rate R_2, the fraction of dijet events in all DIS events, as a function of the kinematic variables x_B and Q^2 in the range $5 < Q^2 < 100\,\mathrm{GeV}^2$ and $10^{-4} < x_B < 10^{-2}$. The analysis is based on data collected with the H1 detector in the years 1996/97. The large amount of integrated luminosity ($21.9\,\mathrm{pb}^{-1}$) available for this analysis allowed for the first time a double differential measurement of R_2 as a function of both x_B and Q^2.

The single differential dijet rate, $R_2(x_B)$ and $R_2(Q^2)$, increases for increasing Q^2 as well as for increasing x_B. The double differential dijet rate $R_2(x_B, Q^2)$ is more sensitive to the x_B dependence of dijet production since it shows a strong increase towards small values of x_B if Q^2 is kept fixed.

The double differential dijet rate has been compared to predictions of NLO QCD calculations. For the comparison it is required that at least one of the jets has a transverse energy $5 + \Delta\,\mathrm{GeV}$ where $\Delta = 2\,\mathrm{GeV}$ was chosen to be the central cut scenario. The dijet rate is well described by NLO calculations when $\mu_r^2 = Q^2$ is chosen as the renormalization scale albeit at the cost of large scale uncertainties. If, however, $\mu_r^2 = Q^2 + E_t^2$ is chosen, which considerable reduces the scale uncertainties, substantial contributions from other sources of dijet production are needed.

The inclusion of contributions from a resolved virtual photon to dijet production can partially account for this discrepancy. However, a judgment of this result is difficult since, presently, the concept of a virtual photon structure in NLO QCD is not completely worked out and the program used to calculate the resolved contributions is not designed for $Q^2 > 20\,\mathrm{GeV}^2$.

It will be interesting to see whether calculations embedding BFKL types of parton evolutions will be able to describe the data at small x_B.

The dijet rate has also been studied as a function of the transverse energy of the jets. As before when choosing $\mu_r^2 = Q^2 + E_t^2$ as renormalization scale, the data at low Q^2 and x_B are only described for large transverse energies of the jets. For large values of Q^2 and x_B, however, the theory successfully matches the data and the choice of the scale variable is less important. The measurement has been extended to a region of phase space where resummation is required in the calculations and therefore provides an important reference for improved theoretical predictions.

Bibliography

[ALB69] W. Albrecht et al., Contributed paper to the 4th int. symposium on electron and photon interactions, Liverpool (1969); DESY-69-046 (1969)

[ALT77] G.Altarelli, G. Parisi, Nucl. Phys. B126 (1977) 298

[AND83] B. Anderson, G. Gustafson, G. Ingelman, T Sjöstrand, Phys. Rep. 97 (1983) 31

[AND77] H.L. Anderson et. al., Phys. Rev. Lett. 38 (1977) 1450

[AND89] B. Andersson et al., Z. Phys. C43 (1989) 621

[ARK99] V. Arkadov, Talk given in the H1 Escale Meeting, 11.6.1999

[AWE92] T.C. Awes et al., Nucl. Instr. Meth. A311 (1992) 130

[BAB94] A. Babaev, Internal H1 Note h1-1294-413 (1994)

[BAS95] U. Bassler, G. Benardi, NIM A350 (1995) 197

[BAR78] W.A. Bardeen, A.J. Buras, D.W. Duke and T.A. Muta, Phys. Rev. D 18 (1878) 3998

[BEC96] H. Beck, Internal H1 Note h1-0596-479, 1996

[BET34] H. Bethe, W. Heitler, Proc. Roy. Soc. A146 (1934) 83

[BET00] S. Bethke, hep-ex/0004021

[BJO69] J.D. Bjorken, E.A. Paschos, Phys. Rev. 185 (1969) 1975

[BLO69] E.D. Bloom et al., Phys. Rev. Lett. 23 (1969) 930

[BOR98] M. Borowski, Diploma thesis, Universität Dortmund, 1998

[CAL69] C.G. Callan, D.J. Gross, Phys. Rev. Lett. 22 (1969) 156

[CAR99] T. Carli, private communication

[CAT92] S. Catani, Yu.L. Dokshitzer, B.R. Webber, Phys. Letters B285 (1992) 291

[CAT93] S. Catani, Dokshitzer, B.R. Webber, Nucl.Phys B406 (1993) 187

[CAT97-1] S. Catani, B.R. Webber, JHEP 10 (1997) 005

[CAT97-2] S. Catani and M.H. Seymour, Nucl. Phys B 485 (1997) 291

[CDF92] CDF Collaboration, Phys. Rev. D 45 (1992) 72

[COL89] J.C. Collins, D.E. Soper, G. Sterman, World Scientific, Singapore 1989

[CTE97] CTEQ collaboration, Phys. Rev. D 55 (1997) 1280

[CTE00] CTEQ collaboration, Eur. Phys. J. C12(2000) 375

[DIR95] M. Dirkmann, Diploma thesis, Universität Dortmund, 1995

[DIR96] M. Dirkmann, Internal H1 Note h1-0596-477, 1996

[DOK77] Yu.L. Dokshitzer, Sov. Physics JETP 46 (1977) 641

[DRE83] J. Drees, H.E. Montgomery, Annual Review of Nuclear Science 33 (1983) 383

[DRE94] M. Drees, R.M. Godbole, Phys. Rev. D 50 (1994) 3125

[ELL93] Ellis, Soper, Phys. Rev. D 48 (1993) 3160

[ENG95] R. Engel et al., Z. Phys. C 66 (1995) 203

[ERD97] M. Erdmann, "The Partonic Structure of the Photon", Springer Tracts in Modern Physics 138, Springer-Verlag Berlin Heidelberg 1997

[FEY69] R.P. Feynman, Phys. Rev. Lett. 23 (1969) 1415

[FLE98] M. Fleischer, Proceedings of VII calorimeter conference CALOR 97, World Scientific (1998) 327

[FOX74] D.J. Fox, Phys. Rev. Lett. 33 (1974) 1504

[FRI91] J.I. Friedmann, Rev. Mod. Phys. 63(1991) 615
H.W. Kendall, Rev. Mod. Phys 63(1991) 597
D.E. Taylor Rev. Mod. Phys. 63(1991) 573

[FRI97] S. Frixione, G. Ridolfi, Nucl. Phys. B507 (1997) 315

[GAR00] F. Garczarek, Diploma thesis, Unversität Dortmund 2000

[GAY96] J. Gayler, Minutes of the H1 energy scale working group, 5.2.1996

[GEI90] W.M. Geist et al., Phys. Rept. 197(1990) 263

[GEL64] M. Gell-Mann, Phys. Lett. 8 (1964) 214

[GLA98] A. Glazov, Dissertation, Humboldt-Universität Berlin 1998

[GLU95] M. Glück, E. Reya, A. Vogt, Phys. Rev. D 51 (1995), 433

[GLU98] M. Glück, E. Reya, A. Vogt, Eur. Phys. J. C5 (1998) 461

[GLU99] M. Glück, E. Reya, I. Schienbein, Phys. Rev. D60 (1999) 054019

[GOR96] L. Görlich et al., Internal H1 Note h1-1291-204

[GRI72] V.N. Gribov, L.N. Lipatov, Soviet Journal of Nuclear Physics 15 (1972) 438

[GRO73] D.J. Gross, F. Wilczek, Phys. Rev. D9 (1973) 3633

[GRO79] J.G.H de Groot et al., Zeitschrift f. Physik C1 (1979) 143

[H1B96] H1 BEMC Group, Nucl. Inst. and Meth. A 372 (1996) 399

[H1C93] H1 Calorimeter Group, Nucl. Inst. and Meth. A 336 (1993) 499

[H1C94] H1 Calorimeter Group, Nucl. Inst. and Meth. A 350 (1994) 57

[H1C96] H1 Collaboration, Nucl. Inst. and Meth. A386 (1996) 310

[H1C98] H1 Collaboration, Eur. Phys. J. C13 (2000) 415

[H1C00] H1 Collaboration, Eur. Phys. J. C13 (2000) 397

[H1C99] H1 Collaboration, Eur. Phys. J. C13 (2000) 609

[H1S96-1] H1 SpaCal Group, Nucl. Inst. and Meth. A 374 (1996) 149

[H1S96-2] H1 SpaCal Group, Nucl. Inst. and Meth A 382 (1996) 395

[H1S99] H1 SpaCal Group, Nucl. Inst. and Meth. A 426 (1999) 518

[HEI99] B. Heinemann, Dissertation, Universität Hamburg, 1999

[HUT90] J. Huth et al., FERMILAB-CONF-90 249-E (1990)

[ING92] G. Ingelman, Proc. of the Workshop on Physics at HERA, eds. W. Buchmüller and G.Ingelman, Hamburg (1992) 1366.
A. Edin, G. Ingelman and J. Rathsman, LEPTO 6.5, DESY-96-05

[IOF69] B.L. Ioffe, Phys. Lett. 30 (1969) 1

[ISS96] Cigdem Issever, Diploma thesis, Universität Dortmund, 1996

[JAN94] J. Janoth et al., NIM A350 (1994) 221

[JAN96] J. Janoth, Dissertation, Universität Heidelberg, 1996

[JET99] Minutes of the regular H1 jet working group meeting, 15.10.1999

[JUN95] H. Jung Comp. Phys. Comm. 86 (1995) 147, in this thesis RAPGAP version 2.06/32 is used

[KEL98] N. Keller et al., Internal H1 Note h1-0898-550, 1998

[KLA96] M. Klasen, G. Kramer, Phys. Lett. B366 (1996) 385

[KLE99] M. Klein, Invited Talk given at the XIX International Symposium on Lepton Photon interactions at High Energies, Stanford 1999, hep-ex/000159 (2000)

[KUR72] E.A. Kuraev, L.N. Lipatov, Sov. J. Nucl. Phys. 15 (1972) 199;
YY. Balitsky and L.N. Lipatov, Sov. J. Nucl Phys. 28 (1978) 822

[KUR93] T. Kurca, Dissertation, Universität Hamburg, 1993

[KRA98] G. Kramer, B. Pötter, Eur. Phys. J. C5 (1998) 665

[KRA84] G. Kramer, Springer Tracts in Mod. Phys. Vol. 102, Springer-Verlag Berlin Heidelberg, 1984

[KWI92] A. Kwiatkowski, H. Spiesberger, H.J. Möring, Proc. of the Workshop on Physics at HERA, eds. W. Buchmüller and G. Ingelmann, Hamburg (1992) 1294

[KWI99] J. Kwiecinski et al., hep-ph/9904402

[LEM97] V.Lemaitre, http://www-h1.desy.de/h1/iww/itrigger/L4Farm/l4new.html

[LEN99] V. Lendermann, Internal H1 Note h1-0899-575, 1999

[LON92] L Lönnblad, Comp. Phys. Comm. 71 (1992) 15, In this thesis ARIADNE version 4.08 is used

[LON95] L. Lönnblad, Z. Phys. C65 (1995) 285

[MAR98] J. Marks, http://www-h1.desy.de/~marks/hfs/hfs.html

[MEY97] A. Meyer, Dissertation, Universität Hamburg, 1997

[MEN78] A. Mendez, Nucl. Phys. B145 (1978) 199
R. Peccei and R. Rückl, Nucl. Phys B162 (1980)
C. Rumpf, G. Kramer, and J. Willrodt, Z. Phys. C7(1981) 337

[MOR98] S. Moretti, L. Lönnblad and T. Sjöstrand, JHEP 08 (1998) 001

[NAU98] J. Naumann, Diploma thesis, Universität Dortmund, 1998

[NAU99] J. Naumann, to appear in Proceedings of the VIII calorimeter conference CALOR 99, World Scientific

[OLS97] J. Olsson
Minutes H1 Data quality meeting 26.8.1997, Report by K. Sedlak
Minutes H1 Data quality meeting 19.8.1997, Report by P. Thompson
Minutes H1 Data quality meeting 25.11.1997, Report by R. Wallny
Minutes H1 Data quality meeting 17.3.1998, Report by R. Pöschl

[PEC80] R.D. Pecci, R. Rückl, Nucl. Phys. B162 (1980) 125

[PFE97] K. Pfeiffer, Diploma thesis, Universität Dortmund, 1997

[POE96] R. Pöschl, Diploma thesis, Universität Dortmund, 1996

[POE97] B. Pötter, Comp. Phys. Comm. 119 (1999) 45

[POE99] B. Pötter, hep-ph/9911221

[POE00] B. Pötter, private communication (2000)

[RUM81] Ch. Rumpf, G. Kramer, J. Willrodt Z. Phys. C7 (1981) 337

[RUT11] E. Rutherford, Phil. Mag. 21 (1911) 669
H. Geiger, E. Marsden, Phil. Mag. 25 (1913) 604
E. Rutherford, Phil. Mag. 37 (1919) 537

[SAS95] G.A. Schuler and T Sjöstrand, Z. Phys. C68 (1995) 607

[SCH92] G.A. Schuler, H. Spiesberger, Proc. of the Workshop on Physics at HERA, eds. W. Buchmüller and G. Ingelman, Hamburg (1992) 1419

[SCH96] G.A. Schuler and T Sjöstrand, Phys. Lett. B376 (1996) 193

[SCH98] S. Schleif, Dissertation, Universität Heidelberg, 1998

[SJO86] T. Sjöstrand, Comp. Phys. Comm. 39 (1986) 74
T. Sjöstrand, Comp. Phys. Comm. 82 (1994) 74

[SPI97] J. Spiekermann, Dissertation, Universität Dortmund, 1997

[WEB84] B.R. Webber, Nucl. Phys. B 238 (1984) 492

[WEL90] H.P Wellisch, Diploma thesis, Max-Planck Institut München, 1990

[WEL94] H.P. Wellisch et al., Internal H1 Note h1-0294-346, 1994

[TZA97] E. Tzamariudaki, Proceedings of VII calorimeter conference CALOR 97, World Scientific (1998) 252

[WEG91] A. Wegner, Internal H1 Note h1-0291-160, 1991

[WOB99] M. Wobisch, T. Wengler, Proceedings of the Workshop 'Monte Carlo Generators for HERA Physics', DESY-PROC-1999-02 270

[WIS98] C. Wissing, Diploma thesis, Universität Dortmund 1998

[ZHO99] A. Zhokin, private communication (1999)

Acknowledgements

During my time as a Ph.D student I have enjoyed the helpfulness, friendship and knowledge from a lot of people. This is now the place to say 'Thank You' to all of them.

First of all I would like to thank Prof. Dr. D. Wegener for his guidance and continous encouragement I had the pleasure to experience during the last 4 years.

I am grateful to Prof. Dr. P. Buchholz who kindly accepted to be the correferent of this work.

Many thanks to Dr. Manfred Fleischer and Dr. Hans-Christian Schultz-Coulon not only for the critical reading of the manuscript but also for their guidance and outstanding support they gave to me even during the hard times of the final stages of this work.

I would like to thank all members of the H1 collaboration and especially of the H1 jet working group. I have benefitted a lot from the good working spirit which was provided by its conveners Dr. Tancredi Carli, Dr. Stephen Maxfield and Dr. Günter Grindhammer.

Furthermore many thanks to Dr. Tancredi Carli for the critical rading of the manuscript and the same to Dr. Guillermo Contreras who did not hesitate to send me comments even from Mexico. My english style was much improved by the help and suggestions of Dr. David Reyna.

Thank you to all my colleagues from Dortmund University and from the office 1b 604 at DESY for a great time inside and outside DESY. Thanks to all my friends who kept me believing that there is life beside High Energy Physics.

A deep thank you to Marion who with love shared patiently all the ups and downs of the last year with me.

Last but not least I would like to thank my family and especially my parents, Rosemarie and Herbert Pöschl, who gave me their love and continous support during my whole life. Thank you very, very much.

Dortmund, October 2000
Roman Pöschl

This work was supported by the Bundesministerium für Bildung, Wissenschaft, Forschung und Technologie, FRG (contract-number: 057DO55P).